Final Report

Impact of Reactive Halogen Species on the Air Quality in California Coastal Areas

Contract No. A-62-1 **Contract No. A-62-2** **Mr. Brent K. Bailey** **Executive Director** **Coordinating Research Council, Inc.** **3650 Mansell Road Suite 140** **Alpharetta, Georgia 30022**	**Agreement #05-307** **Dr. William Vance** **Air Pollution Specialist** **California Air Resources Board** **Research Division** **P.O. Box 2815** **Sacramento, CA 95812**

Prepared by

Dr. Jochen Stutz
University of California, Los Angeles
7127 Math Sciences
Los Angeles, CA 90095

Dr. Bertram T. Jobson
Washington State University
101 Sloan
Pullman, WA 99164

Dr. Ann Louise Sumner
Battelle
505 King Avenue
Columbus, OH 43201

This report was prepared by Battelle Memorial Institute, Columbus Operations (Battelle), University of California, Los Angeles (UCLA), and Washington State University (WSU) as an account of work sponsored by the Coordinating Research Council (CRC) and the California Air Resources Board (CARB). Neither CRC, members of the CRC, CARB, Battelle, UCLA, WSU, nor any person acting on their behalf: (1) makes any warranty, express or implied, with respect to the use of any information, apparatus, method, or process disclosed in this report, or (2) assumes any liabilities with respect to use of, inability to use, or damages resulting from the use or inability to use, any information, apparatus, method, or process disclosed in this report.

Abstract

Air pollution in coastal urban areas remains one of the most serious environmental challenges in the State of California. Urban airshed models, which have been the basis of the development of air pollution mitigation strategies for many years, depend on the accurate description of the relevant chemical mechanisms. Therefore, it is crucial to determine whether the current chemistry in these models is complete, or whether new species and their reactions should be included. The primary goal of this project was to provide experimental evidence for the presence of reactive halogens, reactive halogen precursors, and halogen chemistry in coastal air masses and in the Los Angeles Basin to determine whether halogen chemistry should be included in current urban airshed models of Southern California.

The results of our field experiment at Zuma Beach, Malibu, in October 2006 clearly showed that halogens are present in coastal air upwind of Los Angeles, and that halogen chemistry is occurring. Evidence for chlorine chemistry was found through the observation of up to 12 ppt of Cl_2 and the presence of the chlorine reaction product chloroacetone. Bromine chemistry was found to be less important most of the time. However, sporadic observations of up to 10 ppt of Br_2 deserve further attention. I_2 levels remained below 1 ppt due to its rapid photolysis and the nocturnal off-shore winds. However, observations of several ppt of IO and OIO are proof that iodine chemistry is also occurring.

Macrocystis pyrifera, commonly known as Giant or Iodine Kelp, which is the predominant macroalgae species at the Southern California coast, appears to be the dominant biological source of iodine, and most likely also of bromine. Single particle composition analysis revealed the presence of processed sea salt aerosol at Malibu, indicating that sea salt aerosol is the most likely chemical source of reactive chlorine.

Modeling studies by the UCLA group and comparison with published studies showed that chlorine and iodine chemistry can lead to an increase of ozone levels of 8% (4.5 ppb increase at a 55 ppb base value) in the morning in coastal urban areas in California. The afternoon ozone peak of 76 ppb, on a moderately polluted day, increased by 4% or 3.5 ppb. The presence of halogens also increases OH concentrations by up to 10% and changes the NO/NO_2 ratio. The observation of N_2O_5 shows that the formation of $ClNO_2$ should be considered as an important source of reactive chlorine. Because chlorine and iodine chemistry are linked, the inclusion of iodine chemistry increases chlorine levels in our model and leads to enhanced formation of ozone away from the coastal zone. Models of halogen chemistry should thus always include all three halogen species: chlorine, bromine, and iodine. It should be noted that the model calculations in this project were intended to give more insights into the chemistry of halogens and ozone, rather than to provide an accurate quantification on the ozone levels in the LA-Basin.

The results of our study also revealed a lack in our understanding of the chemistry forming Cl_2 at night, and suggested the importance of as-yet-unidentified iodine reactions. While we have identified kelp as an important source of iodine and probably also of bromine, we cannot estimate the total amount of halogens that are emitted from this source along the California coast.

Our results clearly show that halogen chemistry will impact atmospheric chemistry in Southern California. However, the uncertainties in the chemistry and the sources of halogens make it challenging to give an accurate quantitative assessment of the impact of halogens on the formation of ozone and particles in the Los Angeles Basin. Further research is needed to close the gaps in our understanding of halogen chemistry in polluted coastal areas.

Table of Contents

Abstract 2
List of Tables 5
List of Figures 6
List of Abbreviations 8
1 Introduction 9
2 Review of Atmospheric Halogen Chemistry 11
2.1 Role of halogens in atmospheric chemistry 11
2.1.1 Halogens as oxidants: 11
2.1.2 Catalytic ozone destruction: 14
2.1.3 Influence on HO_x and NO_x 14
2.2 Tropospheric Sources of Reactive Halogen Species 15
2.2.1 Biological sources in the ocean 15
2.2.2 Liberation from sea salt 16
2.2.3 Anthropogenic sources 19
2.3 Previous Studies on Reactive Halogen Species 19
2.3.1 Observations 19
2.3.2 Modeling studies 20
3 2006 Field Experiment 21
3.1 DOAS Measurements (UCLA) 21
3.2 Molecular Halogens by Atmospheric Pressure Ionization Mass Spectrometer (Battelle) 26
3.3 Measurements of VOC (WSU) 27
3.3.1 PTR-MS. 27
3.3.2 GC-MS. 30
3.3.3 Canister sampling 32
3.4 Optical Particle Counter (WSU) 33
3.5 In-Situ measurements of CO, O_3, NO, and NO_y 35
3.6 Meteorological Data and Actinic Fluxes 35
3.7 Molecular Halogens by Mass Spectrometry (UCI / NSF) 36
3.8 Particle Sample and Ionic Composition by Neutron Activation Analysis (UNH /NSF) 36
4 Observations 37
4.1 Meteorological conditions during CalHal 37
4.2 Ozone, NO_x, NO_y, CO and HCHO 37
4.3 VOCs 38
4.3.1 Canister samples 38
4.3.2 Zuma Beach VOCs 41
4.4 NO_3 and N_2O_5 43
4.5 Halogen Oxides 43
4.5.1 BrO 44
4.5.2 IO and OIO concentrations and DSCDs 44
4.5.3 Vertical profiles of IO and OIO 44
4.6 Molecular halogens 48
4.7 Aerosol 49

Table of Contents, Continued

5 Discussion 50
5.1 Dependence of halogen levels on environmental parameters 50
5.2 Coastal Sources of Halogens 51
5.3 Evidence for Chlorine Chemistry at the Southern California Coast 52
5.4 Impact of Halogens on Atmospheric Chemistry on the Southern California Coast and in Los Angeles Basin 53
6 Conclusions 59
6.1 Reactive Halogen Chemistry at the California Coast 59
6.2 Impact on Ozone Formation in the Los Angeles Air Basin 60
6.3 Sources of Halogen Species 61
7 References 63
Figures 74

This report was prepared by:
O. Pikelnaya, J. Stutz, University of California Los Angeles
A.L. Sumner,Battelle
B.T. Jobson, Washington State University

List of Tables

2.1 Comparison of Cl Atom and OH Radical Rate Coefficients at 298 K with Hydrocarbons 11
2.2 Cl atom / OH Ratio for Equivalent Rates of RO2 Production from Hydrocarbon Oxidation 12
2.3 Organohalogen Compound Concentrations in the Boundary Layer and their Respective Photolytic Lifetimes. 16
3.1 Measurements Performed During the Zuma Beach Experiment. 22
3.2 References Used for DOAS Analysis 23
3.3 The Wavelength Window for LP DOAS Data Analysis. 24
3.4 Typical Observed Concentrations and Detection Limits at Zuma Beach 25
3.5 MAX-DOAS Trace Gases Spectral Evaluation Information 26
3.6 Ions Used for Quantification of Molecular Halogens 27
3.7 PTR-MS Measurements. 30
3.8 Species Measured by GC-MS. 32
3.9 Canister Sampling Schedule. 34
4.1 Median Mixing Ratios from Canister Sampling at UCLA and CELA in ppb 39
4.2 Chloroacetone in Canister Samples. 40
4.3 Indicator Hydrocarbon Pairs: Reaction Rate Constants at 298 K. 41
5.1 Halogen reaction included in UCLA's 1D chemical transport model (rate constants and uptake coefficients from [*Atkinson*, 2007; *Sander et al*., 2006]. 55
5.2 List of model runs performed to study the impact of halogen chemistry. 57

List of Figures

3.0.1. Map of field site locations for the Zuma Beach halogen experiment 70
3.0.2. Photograph of mobile containers at the main site at Zuma Beach 71
3.1.1. Schematics of the DOAS experimental set-up at Zuma Beach. 72
3.1.2. Example of the spectral analysis of daytime IO from LP DOAS.....73
3.1.3. Example of the spectral analysis of daytime OIO from LP DOAS.....74
3.1.4. Example of the spectral analysis of daytime IO from MAX-DOAS.....75
3.1.5. Example of the spectral analysis of daytime OIO from MAX-DOAS.....76
3.2.1. Impact of denuder placement and composition on I_2 and Br_2 response 77
3.2.2. Iodine and bromine blanks obtained by flooding the ambient inlet with zero air.....77
3.3.3. Automated zero air blanks for iodine as a function of time of day 78
4.1.1. Meteorological data at Zuma Beach.....80
4.1.2. Daytime measurements of wind speed and wind direction 81
4.1.3. Nighttime measurements of wind speed and wind direction 82
4.2.1. UCLA LP DOAS and UCI in-situ observations of pollutants at Zuma Beach 83
4.2.2 Observations of various nitrogen oxide species, NO_y, and the photolysis frequencies of NO_2. 84
4.3.1. Chloroacetone mixing ratios initially measured in canister samples collected at the UCLA (circles) and CELA (diamonds) sites 85
4.3.2. Replicate sample analysis results for chloroacetone 86
4.3.3. Correlations between hydrocarbon groups from Table 4.3 87
4.3.4. Hydrocarbon mixing ratios measured at Zuma Beach. 88
4.3.5. Zuma Beach time series isoprene, MACR, MVK, and monoterpene isomers. 89
4.3.6. Zuma Beach time series of benzene, toluene, and the sum of C_2-alkylbenzene isomers.....90
4.3.7. Zuma Beach time series of acetaldehyde, m/z=61 assumed to be acetic acid, and m/z=47 attributed to ethanol and formic acid 91
4.3.8. Zuma Beach time series of acetonitrile, methanol, and acetone 92
4.3.9. Zuma Beach time series of chloroacetone and CH_2Cl_2 mixing ratios.....93
4.3.10. Time series of chloroacetone, toluene, and acetaldehyde during the October 19 to October 24 LA basin outflow period.....94
4.3.11. Correlations between chloroacetone and a long lived urban air tracer CH_2Cl_2 and a short lived tracer toluene 95
4.3.12. Correlations between Zuma Beach hydrocarbons with similar OH rate coefficients but significantly different Cl-atom rate coefficients 96
4.3.13. Measure of variability vs. estimated OH lifetime for hydrocarbons measured by GC-MS at Zuma Beach during the LA basin air outflow period.....97
4.5.1. Overview of DOAS observations at Zuma Beach.....98
4.5.2. OIO vertical profile retrieval algorithm 99
4.5.3. OIO DOAS measurement overview.....100
4.5.4. Example of an aerosol profile and the O_4 vertical profile used for RT calculations.....101
4.5.5. Example of the aerosol profile retrieval. 101
4.5.6. Overview of OIO MAX- and LP DOAS measurements 102
4.5.7. Schematic representation of MAX-DOAS light paths 103
4.5.8. Aerosol retrievals for October 13, 2006 between 18:10 and 18:30 UT 103

List of Figures, Continued

4.5.9. OIO vertical profile retrieved for October 13, 2006 at 18:30 UT 104
4.5.10. OIO vertical profile retrieval for October 13, 2006 at 22:03 UT 104
4.5.11. Schematics of the OIO spatial distribution model.....105
4.5.12. MAX-DOAS IO DSCDs and wind speed and direction at Zuma Beach on October 11 and 12, 2006 106
4.5.13. Schematics of IO spatial distribution at Zuma Beach. 107
4.6.1. Battelle ambient I_2 dataset. 108
4.6.2. Overview over all halogen species detected at Zuma Beach 109
4.7.1. Aerosol size distribution, TRAC sample particle morphology observations, and Na and Cl aerosol concentrations 110
4.7.2. Particulate composition of major and minor elements associated with sea-salt particles (A. Pszenny, UNH) 111
4.7.3. Particulate trace metal concentrations. (A. Pszenny, UNH) 112
4.7.4. SEM image of particles collected by TRAC from October 9 22:21. 113
4.7.5. SEM image of particles collected by TRAC from October 10 11:42. 113
4.7.6. SEM image of particles collected by TRAC from October 19 13:03. 114
5.1.1. Dependence of molecular halogensCl_2, Br_2, and I_2 on wind direction 115
5.1.2. Daytime IO and OIO mixing ratios (ppt) and IO/O_4 and OIO/O_4 ratios as a function of wind direction in Malibu 116
5.1.3. Map of the Southern California coastline and neighboring islands 117
5.1.4. Wind data reported by weather stations around Southern California coast at 18:00 UT on October 11, 2006 118
5.1.5. Observed relationship between IO and tidal height in Malibu.....119
5.2.1. Photograph of macroalgae *Macrocystis pyrifera*, Coralline algae, and *Phyllospedix sp.* found at Zuma Beach in October of 2006 119
5.2.2. Photograph of the kelp emission experiment 120
5.2.3. I_2 and Br_2 emission from kelp while enclosed in a Teflon bag 120
5.3.1. Time series of selected tracers during a period of elevated Cl_2 121
5.4.1. Modeled ozone mixing ratios for three scenarios 122
5.4.2. Modeled concentrations of the most important chlorine species 123
5.4.3. Modeled concentrations of the most important iodine.....124
5.4.4. Modeled OH concentration and NO/NO_2 ratios.....125

List of Abbreviations

AMF	air mass factor
APCI-MS/MS	atmospheric pressure chemical ionization tandem mass spectrometry
APS	Aerodynamic Particle Sizer
BAMF	box air mass factor
CalHal	California Halogen Field Experiment
CARB	California Air Resources Board
CCSEM/EDX	Computer Controlled Scanning Electron Microscopy/Energy Dispersed X-ray
CELA	Central Los Angeles air quality monitoring station
CMBA	chloromethylbutenal
CMBL	Coastal Marine Boundary Layer
CMBO	1-chloro-3-methyl-3-butene-2-one
DOAS	differential optical absorption spectroscopy
DMS	dimethylsulfide
DSCD	differential slant column density
EDAX	energy dispersive x-ray analysis
EMSL	Environmental Molecular Sciences Laboratory
EPA	Environmental Protection Agency
FID	flame ionization detector
GC	gas chromatograph
LOD	limit of detection
LP DOAS	long path DOAS
MACR	methacrolein
MAX-DOAS	multi-axis DOAS
MBL	Marine Boundary Layer
MID	multiple ion detection
MS	mass spectrometer
MVK	methylvinylketone
MW	molecular weight
NAA	neutron activation analysis
PNNL	Pacific Northwest National Laboratory
ppb/ppt	parts per billion/trillion by volume
PTR-MS	proton transfer reaction mass spectrometer
RHS	Reactive Halogen Species
SCAQMD	South Coast Air Quality Management District
SCAQS	Southern California Air Quality Study
SAZ	solar azimuth
SEM	imaging - scanning electron microscopy
SEM	secondary electron multiplier
SZA	solar zenith angle
TRAC	Time-Resolved Aerosol Collector
UCI	University of California Irvine
UCLA	University of California Los Angeles
UNH	University of New Hampshire
VOC	volatile organic compounds
WSU	Washington State University

1 Introduction

The chemistry of air pollution is driven by reactions of various radical species [*Finlayson-Pitts and Pitts*, 2000]. It is well known that the hydroxyl radical (OH) and other peroxy radicals (HO_2 and RO_2) play a central role in the formation of ozone and aerosol particles in polluted environments during the day. The nitrate radical (NO_3) plays a similar role during the night. The chemistry of RO_x ($OH + HO_2 + RO_2$) and to a lesser extent of NO_3 forms the basis of current air quality models.

This project addressed a different kind of atmospheric radical species– halogen atoms and halogen oxides. These species have received much less attention than RO_x or NO_3. Over the past few decades the sources and chemistry of reactive halogen species in the troposphere have become much better understood. Reactive halogen species (RHS), such as Cl, Br, and I atoms, and their oxides, are known to influence ozone levels in the stratosphere, where they lead to the well known ozone hole [*Finlayson-Pitts and Pitts*, 2000]. A similar effect has been observed in polar regions at the surface, where a complete depletion of ozone in the lowest 1,000 m over vast areas during spring has been observed [*Barrie et al.*, 1988]. These low ozone events are associated with elevated levels of bromine oxide (BrO) [*Tuckermann et al.*, 1997] and clear chemical signatures of Cl atom and Br atom oxidation of hydrocarbons [*Jobson et al.*, 1998]. During the Arctic spring, *Spicer et al*. have measured significant concentrations of Br_2 and BrCl, species that readily photolyze in sunlight to yield Br and Cl atoms [*Foster et al.*, 2001; *Spicer et al.*, 2002].

Reactive halogen species have also been observed at mid-latitudes. Significant levels of chlorine have been observed at coastal sites [*Pszenny et al.*, 1993; *Spicer et al.*, 1998; *Keene et al.*, 2007], near the Great Salt Lake [*Stutz et al.*, 2002], and in Houston [*Tanaka et al.*, 2003b]. In marine and salt lake environments the source of the halogens is most likely the release from sea salt aerosol or salt deposits, while in Houston industrial emissions are the most likely source. Bromine oxide has been identified both at coastal sites and salt lakes [*Hebestreit et al.*; 1999; *Stutz et al.*, 2002; *Leser et al.* 2003a; *Saiz-Lopez et al.*, 2004b]. The observations of 6 parts per trillion by volume (ppt) BrO upwind of Salt Lake City [*Stutz et al.*, 2002] show that bromine can also be a component of urban pollution. Finally, evidence of reactive iodine compounds in coastal areas is mounting, with observations at various coasts of Europe and the U.S. [*Alicke et al.*, 1999; *Allan et al.*, 2000; *Saiz-Lopez and Plane*, 2004 a,b; *Peters et al.*, 2005; *Stutz et al*., 2007; *Saiz-Lopez et al.*, 2006, 2007 a,b; *Read et al.*, 2008].

Our current understanding of halogen chemistry and the mounting evidence of the presence of these species at mid-latitude motivated our study, which addressed the question of whether halogen chemistry needs to be considered in the atmospheric chemistry of ozone in California coastal cities. The general purpose of this study therefore was to provide information on the concentrations and impacts of reactive halogens on the California coast upwind of the greater Los Angeles area. The original proposal had the following main goals:

1. Determine the atmospheric levels of reactive halogen compounds and their precursors upwind of a coastal California city.

2. Determine the impact of the observed halogen levels on coastal urban air quality, in particular on ozone levels.

3. Evaluate the sources of reactive halogen species through an analysis of the observations.

This report summarizes our findings, which were predominantly derived from a field study performed in Fall 2006 at Zuma Beach in Malibu, CA, a site that under most meteorological conditions is upwind of the Los Angeles Air Basin. The report is divided into several chapters. Chapter 2 gives an introduction into our current knowledge on halogen chemistry, and summarizes previous observations at mid-latitudes and modeling studies of the impact of halogens on air pollution. Chapter 3 gives an overview of the field study and the experimental methods deployed in Malibu and Los Angeles. The results of the field study are presented in Chapters 4 and 5. Chapter 6 presents the conclusions drawn from our study with respect to the goals of our original proposal.

2 Review of Atmospheric Halogen Chemistry

2.1 Role of halogens in atmospheric chemistry

Reactive halogens can impact the chemistry in the troposphere through their influence as hydrocarbon oxidants, on the reaction cycles leading to ozone formation, and through their role as catalysts in the destruction of ozone. These influences are described below. It should be noted that fluorine is not known to play an important role in the chemistry of the atmosphere; we will thus focus on chlorine, bromine, and iodine for the remainder of this report.

2.1.1 Halogens as oxidants

One of the better known properties of halogen atoms, and in particular chlorine, is their potential to oxidize hydrocarbons. The oxidation capacity of the halogen decreases from chlorine to bromine to iodine. The three species will therefore be treated separately.

<u>Chlorine</u>

The chlorine atom is one of the strongest oxidants in the atmosphere [*Finlayson-Pitts*, 1993]. Cl atom initiated oxidation of alkanes and aromatics proceeds by H atom abstraction, forming HCl and an alkyl radial ($R^{\bullet}$):

$$RH + Cl \rightarrow R^{\bullet} + HCl \tag{2.1}$$

Cl initiated oxidation ultimately leads to RO_x production. Unlike OH radicals, which can cycle through many hydrocarbon oxidation cycles before being lost to a chain termination reaction, Cl atoms are not regenerated in a chain reaction. Cl atoms can be formed again through the reaction of OH and HCl (Reaction 2.2) or heterogeneous recycling from aerosols:

$$OH + HCl \rightarrow Cl + H_2O \tag{2.2}$$

Table 2.1 compares Cl atom and OH radical bimolecular rate coefficients for several hydrocarbons to illustrate the difference in their reactivities. In general the reactions of Cl atoms with alkanes are one to two orders of magnitude faster than those of the OH radical, and approach the collisional rate limit ($k_c \sim 1 \times 10^{-10}$ cm^3 $molecule^{-1}$ s^{-1}). For most alkenes/alkynes and aromatic compounds, the differences between Cl atom and OH reaction rates are not as great (factors of 4 to 13, except for acetylene, with the ratio of k_{Cl} to k_{OH} of 82). Another exception is

benzene, which is relatively unreactive with Cl atoms ($k = 1.3 \times 10^{-16}$ cm^3 $molecule^{-1}$ s^{-1}). The significantly greater reactivity of Cl atoms across a broad range of hydrocarbons implies that even small concentrations of Cl atoms can have an impact on ozone formation rates through increasing the rate of RO_2 production.

Table 2.1. Comparison of Cl Atom and OH Radical Rate Coefficients at 298 K with Hydrocarbons.

Reacting Hydrocarbon	**$k_{Cl} \times 10^{-12}$** (cm^3 $molecule^{-1}$ s^{-1})	**$k_{OH} \times 10^{-12}$** (cm^3 $molecule^{-1}$ s^{-1})	**Ratio** k_{Cl}/k_{OH}
Alkanes [a]			
Methane	0.1	0.0064	16
Ethane	5.93	0.257	231
Propane	140	1.11	126
i-butane	140	2.16	64
n-butane	210	2.45	86
i-pentane	210	3.74	56
n-pentane	270	3.97	68
Hexane	330	5.28	63
Heptane	380	6.52	58
2,2,4-trimethylpentane	250	3.34	75
Alkenes / Alkynes [b]			
Acetylene	67 [c]	0.78 [d]	82
Ethene	107 [c]	8.52	13
Propene	281 [c]	26.3	11
1,3-butadiene	420 [e]	66.6	6
Isoprene	460 [e]	101	5
Aromatics [f]			
Benzene	1.3×10^{-4} [g]	1.22	1.1×10^{-4}
Toluene	58 [h]	5.63	10
o-xylene	143 [h]	13.6	10
m-xyelene	130 [h]	23.1	6
p-xylene	142 [h]	14.3	10
1,3,5-trimethylbenzene	242 [i]	56.7	4

References to rate coefficient values:

a. "Mechanisms of Atmospheric Oxidation of the Alkanes", Ed. J.G Calvert., Oxford University Press, New York, 2008.
b. Except for otherwise noted values are from "Mechanism of the Atmospheric oxidation of the Alkenes", Ed. J.G. Calvert, Oxford University press, New York, 2000.
c. Average of two studies*: Atkinson and Aschmann*, 1985; *Wallington, Skewers, and Siegel*, 1988.
d. *Atkinson et al.,* 2007.
e. *Ragains and Finlayson-Pitts*, 1997.
f. OH rate coefficients from "Mechanisms of Atmospheric Oxidation of Aromatic Hydrocarbons", Ed. J.G. Calvert, Oxford University Press, New York, 2002.
g. *Sokolov et al.,* 1998.
h. Average of two studies: *Shi and Bernhard*, 1997; *Wallington, Skewers, and Siegel*, 1988.
i. *Wang, Arey and Atkinson*, 2005.

A rough estimate of the Cl atom concentration required to influence urban ozone formation can be calculated by equating the rates of RO_2 production from the Cl and OH initiated oxidation of hydrocarbons found in urban areas. Two major hydrocarbon sources in urban areas are roadway emissions (composed of a mix of alkanes, alkenes, and aromatics) and natural gas emissions (principally composed of methane with small fractions of C_2-C_4 alkanes). The relative abundance of hydrocarbons in auto exhaust is reasonably well known from air sampling in traffic tunnels [*Jobson et al.*, 2004 and references therein]. These hydrocarbon source profiles will be used to illustrate the low concentration of Cl atoms required to significantly impact RO_2 production rates. The RO_2 production rate P (molecules s^{-1}) from OH initiated oxidation of hydrocarbons is given by

$$P_{RO2}^{HO} = [OH]\sum_i k_{OH,i}[R_i] \qquad \text{(E2.3)}$$

where $k_{OH,i}$ is the bimolecular rate coefficient for reaction of OH with hydrocarbon species *i* and R_i is the concentration of that hydrocarbon. A similar expression follows for Cl initiated oxidation. Table 2.2 shows the ratio of concentration of Cl atoms to OH needed for the RO_2 production rates to be equal for the two different hydrocarbon source profiles. Cl atom concentrations at levels of only a few percent of those of OH will have a profound influence on ozone production rates in urban areas through increased RO_2 radical production rates. The difference between the ratios for the two hydrocarbon sources is a consequence of the much larger ratio of k_{Cl}/ k_{OH} for alkanes than for alkenes and aromatics (see Table 2.1). Increasing the proportion of alkanes in an urban atmosphere (for example through increased natural gas usage) will increase an urban airshed's sensitivity to Cl atom chemistry.

Table 2.2. Cl atom / OH Ratio for Equivalent Rates of RO_2 Production from Hydrocarbon Oxidation.

Hydrocarbon Source Profile	**Cl / OH ratio**
Roadway Traffic Tunnel	0.069
Natural Gas	0.012

The influence of chlorine on urban air ozone formation rates has been experimentally investigated by *Tanaka et al.* [2003a], who found that the addition of small amounts of Cl_2, which rapidly photolyzes into Cl atoms, to urban air captured in a Teflon bag increased the ozone formation rate from 36 ppb/h to 78 ppb/h in the Houston area.

Bromine

Bromine atoms are generally less reactive towards hydrocarbons than Cl atoms and the OH radical. While Br atoms will react relatively rapidly with alkenes forming addition products, Br atoms are essentially unreactive with alkanes and aromatics and thus would play a minor role in the creation of alkyl radicals in an urban atmosphere. However, there are two very important reactions involving bromine that impact particulate matter formation and its toxicity. The first is the reaction of BrO with dimethylsulfide (DMS), which can be responsible for the formation of sulfuric acid and sulfate particles in the marine boundary layer [*von Glasow et al.*, 2004]. This reaction is thought to be an important source of particulate sulfate in the marine environment and may have a significant influence on background sulfate levels along the California coast.

The second reaction is that of Br atoms (and Cl atoms) with atmospheric mercury (Hg^0) [*Ariya et al.*, 2002]. Mercury is one of the most toxic elements in nature and its derivatives bioaccumulate. The halogen atom + Hg^0 reactions are fast and yield low volatility products that condense onto particles. The reaction of Br atoms with Hg^0 in the Arctic is a significant source of Hg deposition into the high Arctic ecosystem [*Ariya et al.*, 2004; *Steffen et al.*, 2008]. Similarly, reactions of Br and Cl with Hg^0 in polluted coastal environments may be a significant source of airborne particulate Hg and a clear health concern for Californians living in coastal environments.

Iodine

Iodine atoms are fairly unreactive towards hydrocarbons. Consequently they are not converted to HI through this pathway and thus remain longer in the gas-phase than either Cl or Br.

2.1.2 Catalytic ozone destruction

The best known influence of halogens on ozone is through catalytic destruction cycles, which are responsible for the stratospheric ozone hole and the sudden ozone depletion events in the Arctic [*Finlayson-Pitts et al.*, 1990; *LeBras and Platt*, 1995; *Wayne et al.*, 1995]. The key species in both mechanisms are the halogen oxides XO and YO (X, Y = Cl, Br, I), which are formed in the reaction of halogen atoms with ozone (reactions 2.4 and 2.5).

Three kinds of catalytic cycles can be distinguished, each beginning with the reaction of the halogen atom with an ozone molecule (Reaction 2.4). In the first mechanism (Cycle A), the self- or cross - reaction of the halogen oxides XO and YO (reaction 2.6) are responsible for recycling the halogen atoms such that they can reenter the mechanism. In total, this Cycle A converts two ozone molecules into three oxygen molecules without loss of RHS.

Cycle A:

$$X + O_3 \rightarrow XO + O_2 \tag{2.4}$$

$$Y + O_3 \rightarrow YO + O_2 \tag{2.5}$$

$$XO + YO \rightarrow X + Y + O_2 \tag{2.6}$$

Net reaction: $2O_3 \rightarrow 3O_2$

The rate of reaction (2.6) determines the efficiency of Cycle A. Consequently, the rate of this mechanism depends on either the square of the XO concentration for the self reaction, or the product of [XO][YO], and is only effective at relatively high (>10 ppt) XO levels [*Stutz et al.*, 1999]. These levels have been observed in the Arctic and near salt lakes, but thus far not in the marine boundary layer.

The second ozone loss process (Cycle B) proceeds through the reaction of XO with HO_2 (reaction 2.7). The HOX formed is then photolyzed (reaction 2.8), recycling a halogen atom. Together with the formation of HO_2 by different OH reactions, this cycle also converts O_3 into O_2.

Cycle B:

$$X + O3 \rightarrow XO + O2 \tag{2.4}$$

$$XO + HO_2 \rightarrow HOX + O_2 \tag{2.7}$$

$$HOX + h\nu \rightarrow X + OH \tag{2.8}$$

$$OH + CO,\ O_3 \text{ or VOC} \rightarrow\rightarrow HO_2 + \text{products} \tag{2.9}$$

Net reaction (2.9): $O_3 \rightarrow O_2$

This reaction cycle only depends on the concentration of XO, and thus dominates at low XO levels [*Stutz et al.*, 1999].

Evidence for the occurrence of both Cycles A and B has been observed in the Arctic and near salt lakes [*Hebestreit et al.*, 1999; *Stutz et al.*, 2002; *Tuckermann et al.*, 1997].

A third cycle (Cycle C) proceeds through the formation of the halogen nitrate $XONO_2$, here written for the iodine pathway.

Cycle C:

$$I + O3 \rightarrow IO + O2 \tag{2.10}$$

$$IO + NO_2 \xrightarrow{M} IONO_2 \tag{2.11}$$

$$IONO_2 + h\nu \rightarrow I + NO_3 \text{ (main pathway)} \tag{2.12a}$$

$$\rightarrow IO + NO_2 \tag{2.12b}$$

$$IONO_2 \xrightarrow{M} IO + NO_2 \tag{2.13a}$$

$$\xrightarrow{M} I + NO_3 \tag{2.13b}$$

$$NO_3 + h\nu \rightarrow NO + O_2 \tag{2.14}$$

$$NO + O_3 \rightarrow NO_2 + O_2 \tag{2.15}$$

Net: $2O_3 \rightarrow 3O_2$

2.1.3 Influence on HO_x and NO_x

In addition to affecting the catalytic ozone destruction mechanisms discussed above, halogens also influence the photochemical equilibria of NO/NO_2 and OH/HO_2 in the atmosphere. The ratio of nitric oxide (NO) and nitrogen dioxide (NO_2) concentrations is normally described by the Leighton ratio (Equation 2.17). If halogen atoms are present, the reaction

$$XO + NO \rightarrow X + NO_2 \tag{2.16}$$

introduces another pathway to convert NO into NO_2.

The ratio of [NO] and [NO_2], or the Leighton ratio (L), can therefore be expanded as shown in equation 2.17 (please note that we have also added the $RO_2\bullet + NO \rightarrow RO\bullet + NO_2$ reactions in equation 2.17):

$$L = \frac{[NO_2]}{[NO]} = \frac{[O_3]\cdot k_{NO+O3} + [HO_2]\cdot k_{NO+HO2} + \sum[RO_2]\cdot k_{NO+RO2} + \sum[XO]\cdot k_{NO+XO}}{J_{NO2}} \qquad \text{(E2.17)}$$

The presence of iodine oxide, which has been observed at levels of 5 ppt in polluted air masses by one of our groups, will increase L by ~10%. This increase is fairly independent of the NO_x levels in the case of iodine.

In addition, the ratio and the absolute concentrations of hydroxyl radical (OH) and peroxy radical (HO_2) are affected by the halogens. When halogen oxides are present, HO_2 can be converted to OH by the production of HOX (reaction 2.7), followed by its photolysis (reaction 2.8). Model calculations show that with halogens present, the HO_2 concentration decreases, while [OH] increases [*Stutz et al.*, 1999]. Simple steady state arguments are difficult to use in this analysis, but a comparison between the rates of the HO_2/RO_2 + NO reactions and that of HO_2 + IO shows that, at high NO_x (> 1 ppb), the HO_2/OH ratio is not significantly influenced by the HOI pathway, and reacts primarily to the change of NO due to the change in L. At low NO_x, however, the HOI shortcut can increase the HO_2 sink and OH formation rate by 40% and 15% respectively [*Bloss et al.*, 2005].

The three mechanisms above can have considerable influence on ozone chemistry in marine air. Whether the catalytic destruction of ozone or an enhanced formation will occur depends on the levels of the reactive halogen species and the levels of NO_x. While there have been very few studies on the impact of chlorine chemistry on ozone chemistry in polluted air (see below), iodine chemistry in polluted air has not been considered thus far.

2.2 Tropospheric Sources of Reactive Halogen Species

2.2.1 Biological sources in the ocean

Photolytically unstable organohalogen compounds and molecular iodine (and possibly bromine) act as precursors of halogen atoms in the troposphere. Most of these compounds are of marine origin being emitted by plankton and algae in the ocean [*Rasmussen et al.*, 1982; *Khalil et al.*, 1981; *Carpenter et al.*, 1999; 2000; 2001; 2003]. While many of the organohalogen compounds are present in the atmosphere (e.g., CH_3Cl, CH_3Br, and CH_3I, etc.), as summarized in Table 2.3, the production rate of halogen atoms is small due to the slow photolysis of these compounds. These precursors are most likely not a significant source for chlorine atoms. On the other hand, much shorter lived alkyl-iodides and alkyl-bromides may be important. Measured concentrations of alkyl-iodides in the marine boundary layer may explain the elevated IO mixing ratios observed at Mace Head, Ireland [*Carpenter et al.*, 1999; 2000]. In particular, CH_2I_2 and CH_2BrI have been observed at mixing ratios of up to 1 ppt, and are potential iodine and bromine atom precursors. It is possible that other, thus far unidentified, short-lived organo-iodides also contribute to iodine production.

Table 2.3 Organohalogen Compound Concentrations in the Boundary Layer and their Respective Photolytic Lifetimes [a]

Species	Concentration	Lifetime
CH_3Cl	~ 630 ppt	~ 1 year
CH_2Cl_2	~ 32 ppt	83 days
CH_3Br	20-40 ppt	1-2 years
$CHBr_3$	N/A	Days
CH_3I	1- 30 ppt	3-4 days
CH_2I_2	up to 1 ppt [c]	5 min [b]
CH_2ClI	up to 1 ppt [c]	10 hours
CH_2BrI	up to 1 ppt [c]	45 min [b]

a. All data from WMO Report if not noted otherwise
b. *Moessinger et al.,* 1998
c. *Carpenter et al.,* 1999

Recently I_2 has also been observed at Mace Head, Ireland at levels sufficient to explain the presence of reactive iodine species [*Saiz-Lopez and Plane*, 2004a]. I_2 photolyzes rapidly and originates most likely from macro-algae, for example of the type *Laminaria*, which are exposed to air. I_2 was also observed in the Gulf of Maine by one of our groups, though its source is not well understood.

In summary, direct oceanic emissions, most likely from algae, are the main source of reactive iodine precursors. These emissions may also include precursors for reactive bromine. However, direct experimental evidence for this has not yet been found.

2.2.2 Liberation from sea salt

The largest reservoirs of halogens in the atmosphere are sea salt aerosols and salt covered surfaces [*Keene et al.*, 1990]. The typical halogen composition of sea salt is (by weight): 55.7 % Cl^-, 0.19 % Br^- and 2×10^{-5} % I^- (in standard mean ocean water). The low amount of iodine makes liberation of this element from sea salt an unlikely source of observed reactive iodine concentrations in marine environments. However, for chlorine and bromine the release from this reservoir is thought to be the principal source of reactive chlorine and bromine species.

A number of processes that volatilize chlorine and bromine from aerosol or salt surfaces have been studied (see review by *Finlayson-Pitts* [2003]). These processes can be subdivided into those occurring on solid salt surfaces, which are important at low relative humidity values, and those occurring in deliquescent particles and/or salt solutions at high relative humidities.

The best known mechanism for releasing chlorine (and bromine) from salt is the displacement of chlorine by acids such as H_2SO_4 or HNO_3. This reaction occurs both on solid and aqueous particles

$$NaCl + HNO_3 \rightarrow HCl + NaNO_3 \qquad (2.18)$$

This mechanism is responsible for the depletion of chlorine in aged sea salt particles in polluted environments, as has been observed in many locations, including the Los Angeles Basin [*Hughes*

et al., 2000]. Only in cases where large amounts of HCl are present, such as the 7.5 ppb observed in the South Coast Air Basin [*Appel et al.*, 1988], does this reaction become important for the formation of chlorine atoms (via reaction 2.2).

More important for the formation of reactive chlorine and bromine are processes that release photolabile precursors, such as X_2 and XNO_2, which photolyze, releasing the halogen atom (X=Cl, Br):

$$X_2 + h\nu \rightarrow 2\ X \tag{2.19}$$

$$XNO_2 + h\nu \rightarrow X + NO_2 \tag{2.20}$$

Several of these processes have been observed in the laboratory. It should, however, be noted that many of these mechanisms are not well understood, severely restricting our ability to accurately model their impact.

On solid salt surfaces such as sea salt particles below their crystallization point, oxidants such as OH, O_3, and NO_3 react, releasing either Cl or Br directly or in the form of Cl_2 and Br_2. [*Gershenzon et al.*, 1999; *Finlayson-Pitts*, 2003] (X=Cl, Br):

$$NaX + OH \rightarrow ½\ X_2 + NaOH \tag{2.21}$$

$$NaX + O_3 \rightarrow \rightarrow HOX \tag{2.22}$$

$$NaX + NO_3 \rightarrow X + NaNO_3 \tag{2.23}$$

The reactions of nitrogen oxides on NaCl, KBr, and other salt surfaces are also known to release XNO_2 and XNO [*Finlayson-Pitts et al.*, 1983; *Zetzsch et al.*, 1988; *Behnke et al.*, 1991; 1992; 1997; *Zetsch and Behnke*, 1992;]. Such reactions include:

$$N_2O_5 + NaX \rightarrow XNO_2 + NaNO_3 \tag{2.24}$$

$$2\ NO_2 + NaX \rightarrow XNO + NaNO_3 \tag{2.25}$$

XNO and XNO_2 photolyze rapidly in early morning hours [*Wayne et al.*, 1995] and release halogen atoms. This mechanism would be most effective in relatively polluted air with high NO_x concentrations, such as in populated coastal areas of California.

A number of aqueous phase chemical cycles releasing halogens have been studied (see [*Finlayson-Pitts*, 2003]). The reaction of ozone on salt particles (reaction 2.22), which is slow for chlorine and faster for bromine, forms HOCl or HOBr in the aqueous phase, which can then be released into the gas phase (X=Cl, Br):

$$O_3 + X^- \rightarrow XO^- + O_2 \tag{2.26}$$

$$H^+ + XO^- \leftrightarrow HOX \tag{2.27}$$

In contrast to the relatively slow reaction of O_3, the reaction of OH on deliquescent particles is much faster. The following mechanism has been attributed to this Cl release process:

$$OH + Cl^- \rightarrow HOCl^- \tag{2.28}$$

$$HOCl^- + H^+ \leftrightarrow Cl + H_2O \tag{2.29}$$

$$Cl + Cl^- \leftrightarrow Cl_2^- \tag{2.30}$$

$$2Cl_2^- \rightarrow Cl_2 + 2Cl^- \tag{2.31}$$

$$Cl + Cl_2^- \rightarrow Cl^- + Cl_2 \quad (2.32)$$

Ultimately this mechanism releases Cl_2 from the aerosol during the day. Halide ions can also be oxidized by NO_3 and N_2O_5 at night:

$$NO_3 + X^- \rightarrow NO_3^- + X \quad (2.33)$$

$$N_2O_5 + X^- \rightarrow NO_3^- + XNO_2 \quad (2.34)$$

All these mechanisms have been observed in the laboratory. The formation of $ClNO_2$ has recently been observed along the coast of Texas near Houston and in the Houston ship channel, where *Osthoff et al.* [2008] found up to 600 ppt of $ClNO_2$. In addition, recent studies show that halide ions are concentrated on the surface of particles, making these reaction faster than previously assumed [*Finlayson-Pitts*, 2003; *Ghosal et al.*, 2005a; 2005b].

There are a number of processes that recycle reactive halogens on aerosol particles, or even lead to an autocatalytic release of halides from salt particles. The best known example is the so-called "bromine explosion", which is believed to be responsible for the release of bromine in the polar regions [*Fan and Jacob*, 1992; *Mozurkewich*, 1995; *Vogt et al.*, 1996]. As outlined by *Vogt et al.* [1996], HOBr can react on the surface with Cl^- to form BrCl, which can hydrolyze back to HOBr or react with Br^- to form Br_2:

$$HOBr\ (aq) + Cl^- + H^+ \rightarrow BrCl\ (aq) + H_2O \quad (2.35)$$

$$BrCl\ (aq) + H_2O \rightarrow HOBr\ (aq) + H^+ + Cl^- \quad (2.36)$$

$$BrCl\ (aq) + Br^- \rightarrow Br_2\ (aq) + Cl^- \quad (2.37)$$

Br_2 and BrCl can then return to the gas phase, where they are photolyzed to yield Br atoms that can react with ozone again to form BrO (reaction 2.4). The subsequent reaction of BrO with HO_2 (reaction 2.7) yields HOBr, which can again react heterogeneously on the surface. In this reaction scheme one HOBr can release up to 2 Br atoms per cycle. If less than 50% of the bromine is lost from the cycle, the number of gas phase bromine molecules increases exponentially (at the expense of Br^-). Our current understanding shows that bromine is released from this autocatalytic process and that chlorine is a byproduct. This reaction cycle is important on acidified surfaces such as those found in polluted environments.

Many of the chemical processes described above have been observed in the laboratory. However, these studies are often made at much higher reactant concentrations and with "model-aerosol" particles, i.e. fresh NaCl instead of true aged sea salt particles. It is therefore unclear to what extent these reactions contribute to the atmospheric release of reactive halogen species. In addition, reports from laboratory and modeling studies indicate that halide ions are concentrated on the surfaces of particles [*Finlayson-Pitts*, 2003; *Ghosal et al.*, 2005a; 2005b]. The fact that the halide reactants are on the particle surface suggests that the liberation of photolabile halogen species from sea salt may even be faster than previously assumed.

Finally it should be noted that, with the exception of the "bromine explosion," there are currently no atmospheric studies that allow us to determine which of the various release mechanisms is important, and to what extent each mechanism contributes to the levels of reactive halogens. The uncertainty in the kinetics of these reactions precludes accurate modeling studies of their significance in the atmosphere and their influence on urban air quality. Direct

observation of RHS concentrations in the atmosphere is required for reliable assessment of their impact on urban air chemistry.

2.2.3 Anthropogenic sources

While our work focused mainly on oceanic sources of reactive halogens in coastal California, it should be mentioned that there are also a number of anthropogenic sources of RHS precursors. The EPA toxic release inventory (www.epa.gov/tri) lists a total emission of 93 pounds/yr of Cl_2 from fugitive air emissions and 355 pounds/yr from point source air emissions, such as metal processing facilities, for Los Angeles County. Compared to other locations outside of California, these emissions are fairly low [*Tanaka et al.*, 2000]. Other sources of chlorine are cooling towers, water treatment, and swimming pools. A 1988 CARB report [*Rogozen et al.*, 1988] lists the use of chlorine compounds as a biocide in electric utility cooling towers as ~ 100 tons of chlorine equivalent per year, while their use in water treatment is even higher. However, it is not clear how much of this chlorine is actually released into the atmosphere as a reactive halogen precursor (the CARB report focused on chloroform), and how the emission rates have changed since 1988.

2.3 Previous Studies on Reactive Halogen Species

2.3.1 Observations

Observational evidence for the presence of reactive halogens in the marine boundary layer (MBL) outside of polar regions is sparse. *Pszenny et al.* [1993] report 48 to 268 ppt of non-HCl reactive chlorine (most likely Cl_2 and HOCl) on the coast of Florida. *Spicer et al.* [1998] provide the most direct proof of the presence of chlorine atom precursors, finding 150 ppt of Cl_2 near the coast of Long Island. Chlorine was monitored with high specificity by atmospheric pressure chemical ionization tandem mass spectrometry (APCI-MS/MS). Multiple parent/daughter ion isotope pairs for Cl_2 were monitored to ensure specificity.

Keene et al. [2007] found non-HCl reactive chlorine between 50 and 400 ppt in polluted air over the Gulf of Maine. These observations were accompanied by a near complete depletion of chlorine from sea salt particles and HCl mixing ratios of up to 6 ppb. While no direct measurements of reactive chlorine have been made on the California coast, or on the U.S. Pacific coast in general, there is evidence that chlorine chemistry is occurring in the South Coast Air Basin. For example *Appel et al.* [1988] report HCl mixing ratios of up to 7.5 ppb during the 1987 Southern California Air Quality Study (SCAQS). That the HCl originated from sea salt was confirmed by the observation of chlorine depletion in larger aerosols (for example *Hughes et al.* [2000]). Indirect evidence of chlorine chemistry was also provided by *Tanaka et al.* [2003b] in Houston, TX, where anthropogenic sources are suspected as the origin of the chlorine. However, aerosol chlorine depletion was also observed. Recently *Osthoff et al.* [2008] reported the observation of up to 600 ppt of $ClNO_2$ in the Houston ship channel. They argue that at these $ClNO_2$ levels, chlorine chemistry can considerably influence ozone chemistry in Houston.

Reactive bromine in the marine boundary layer outside of polar regions has also been quite elusive. *Leser et al.* [2003] report 2.3 ppt of BrO in the marine boundary layer, while *Saiz-Lopez et al.* [2004b] report up to 4 ppt on the Irish coast. However, numerous other reports fail to find BrO in the marine boundary layer.

There are now a number of measurements of reactive iodine species in coastal areas in Europe, Tasmania, Tenerife, and the Gulf of Maine (for example *Alicke, et al.*, 1999; *Allan, et al.*, 2000; *Saiz-Lopez and Plane*, 2004a; *Peters et al.*, 2005, *Stutz et al.*, 2007; *Read et al.*, 2008), where mixing ratios of up to 7 ppt have been observed in the clean marine boundary layer. In a recent study in the fairly polluted Gulf of Maine, the UCLA group observed up to 7 ppt of IO and up to 30 ppt of OIO [*Stutz et al.*, 2007].

2.3.2 Modeling studies

Modeling efforts of halogen chemistry have thus far mainly concentrated on the unpolluted marine boundary layer. A number of studies have also considered the chemistry of chlorine and bromine under polluted conditions. However, the results are not conclusive, because they strongly depend on the assumption of pollution levels, sea salt aerosol levels, and the chemical halogen release mechanisms. In particular, the chemical mechanisms are quite uncertain, as described above. Most of the studies assume classical aqueous phase chemistry, without considering the aerosol surface enrichment of the halides. For example, *Sander and Crutzen* [1996] find Cl_2 levels of up to 40 ppt, 6 ppb of HCl, and Cl atom levels of 2×10^4 cm^{-3}. The only studies of halogen chemistry on the California coast, by *Knipping and Dabdub* [2003] and *Cohan et al*. [2008], found up to 12 ppt Cl_2 in the base case. The inclusion of the recently proposed heterogeneous and aqueous halogen release mechanisms [*Knipping and Dabdub*, 2002], and in particular those occurring at night, indicated higher Cl_2 levels of 200 – 300 ppt. While the impact on ozone levels in this case was significant, it should be pointed out that the inclusion of novel heterogeneous chemistry was highly speculative and that there is no observational evidence that the Cl_2 levels predicted by the model are realistic. In a follow-up study [*Cohan et al*., 2008], the same group investigated the impact of chlorine chemistry on the weekend effect. In general the results were similar to those of *Knipping and Dabdub* [2003], predicting that the presence of chlorine led to an increase of ozone in the basin. The impact on the weekend effect was small in the base chlorine case. Large changes in ozone and the weekend effect were found for cases with amplified chlorine formation. However, the study again predicted Cl_2 levels of up to 1 ppb along the coast.

The fact that current models are unable to reproduce the few observations of high chlorine without the inclusion of additional speculative heterogeneous chemistry shows that our understanding of halogen chemistry is currently insufficient to quantitatively assess its impact on atmospheric chemistry in polluted areas solely based on model calculations. In addition, iodine chemistry has thus far not been considered. There is also a lack of reliable observational data in the atmosphere that would help in the determination of the chemical mechanisms responsible for the release of reactive halogens to the atmosphere.

3 2006 Field Experiment

The main activity of this project was the performance of the California Halogen Field Experiment (CalHal) from October 4 to 24, 2006 on the coast upwind of Los Angeles. Samples were also taken at two sites in the basin. The focus of the experiment was on providing basic data on the presence of reactive halogens. In addition, various pollutants, meteorological parameters, and actinic fluxes were measured. The experiment consisted of three measurement locations. The primary site, where the majority of scientific equipment was located, was at Zuma Beach, Malibu. Canister samples for chloroacetone analysis were also sampled at UCLA and the South Coast Air Quality Management District (SCAQMD) central Los Angeles (CELA) air quality monitoring station.

Zuma Beach is a one mile-long stretch of beach located in Malibu, north-west of the Los Angeles area (Figure 3.0.1). All scientific equipment at Zuma Beach was housed in two mobile office containers placed at the edge of a Zuma Beach parking lot (Figure 3.0.2). Instrumentation was separated from the ocean by approximately 100 ft of sandy beach. There are no industrial sources of pollutants in Malibu or its surrounding areas. Pacific Coast Highway, which around Zuma Beach only carries light traffic in October, is the only local source of fresh traffic emissions. The parking lot was used very little during the experiment, with an average of around 5 – 10 cars present during the day.

The UCLA site was located on the roof of Bunche Hall, an 11 story building on the UCLA campus. The CELA site is located approximately 2 miles northeast of downtown Los Angeles, on the roof of a 3-story warehouse (Figure 3.0.1).

A variety of state of the art analytical techniques were deployed during the CalHal experiment. This section provides an overview of the various techniques, their properties, as well as the QA/QC performed on the data. Please note that the PI's were joined by E. Saltzman's group from the University of California Irvine, and the group of A. Pszenny from the University of New Hampshire. Both groups brought valuable additions to the field effort. While their activities were funded by the National Science Foundation we will refer to the data throughout the report. Table 3.1 provides a summary of the collective measurements preformed in October 2006. More detailed descriptions of the techniques follow below.

3.1 DOAS Measurements (UCLA)

The UCLA group performed simultaneous measurements with the Long Path (LP) and Multi-Axis (MAX) Differential Optical Absorption Spectroscopy (DOAS) instruments. Figure 3.1.1 illustrates schematically the DOAS measurements set up at Zuma Beach. Lines of sight of both DOAS instruments were almost parallel to each other (see Figure 3.0.1).

Table 3.1. Measurements Performed During the Zuma Beach Experiment.

Species/Parameter	Experimental Technique	Group
Concentrations of IO, OIO, I_2, BrO, ClO, O_3, NO_2, SO_2, HCHO, HONO, NO_3	Long path DOAS (LP DOAS)	UCLA
Concentrations averaged over the boundary layer and vertical profile information of IO, OIO, I_2, BrO, NO_2, HCHO, glyoxal, O_4	Multi Axis DOAS (MAX-DOAS)/UCLA	UCLA
Concentrations of Cl_2, Br_2, I_2	Atmospheric Pressure Chemical Ionization Mass Spectrometry	Battelle
Concentrations of Cl_2, Br_2, I_2, BrCl, ICl	Mass Spectrometer	UCI [a]
Concentrations of NO, NO_2, NO_y	Chemiluminescence	Battelle UCI [a]
Concentrations of CO	Gas filter correlation/Battelle	Battelle
Concentrations of C4-C10 alkane and aromatic; Chloroacetone, bromoacetone, CMBO, CMBA, CH3I	in situ GC-MS and PTR-MS	WSU
Particle size distribution 0.5 – 20 µm	Lasair optical particle counter	WSU
Elemental composition of individual aerosol particles	CCSEM/EDX	PNNL / WSU
Particle Cl, Br, I	Particle sampler and NAA	UNH*
Canister Samples of VOC (UCLA and downtown LA)	Automated samplers	WSU UCLA
Actinic flux and photolysis rates	Spectroradiometer	UCLA
Temperature, relative humidity, wind speed, wind direction, solar radiation	Meteorological station	UCLA

a. Measurements funded by NSF

The UCLA LP DOAS telescope was set up in one of the office containers (Figure 3.2) at ocean level. The retro reflector array was attached to the service structure at El Matador State Beach 5.3 km away, 36 m above the ocean surface. The LP DOAS light path ran approximately parallel to the coast line between Zuma and El Matador beaches (Figure 3.1).

The LP DOAS measured sequentially in four different wavelength intervals. Except for the NO_3 measurement interval, measurements in the remaining three intervals were performed using the multichannel scanning technique (MCST) [*Brauers et al.*, 1995] every 20 to 30 minutes with integration times of 5 to 10 minutes depending on visibility.

The UCLA MAX-DOAS telescope was located on the roof of one of the office containers. The MAX-DOAS instrument collected scattered sunlight from six different elevation viewing angles: 1°, 2°, 3°, 5°, 10°, and 90°; with an azimuth viewing angle slightly to the west of the same direction as the LP-DOAS line of sight, in order to avoid observing backscattering from the coast (see red dashed line on Figure 3.0.1). The MAX-DOAS instrument measured in subsequent sets of elevation viewing angles in a 130 nm wavelength interval with center wavelengths of 385 nm

and 530 nm. Depending on visibility, a typical sequence of measurements for one wavelength interval required approximately 6 minutes.

The spectral analysis of the LP and MAX-DOAS spectra was performed using a combination of linear and non-linear least squares fit [*Stutz and Platt*, 1996].

LP-DOAS Data Analysis:

The use of the multichannel scanning technique [*Brauers et al.*, 1995] for most LP DOAS measurements requires careful assembly of a single MCST spectrum from the individual spectra in a series. For each atmospheric absorption spectrum, the background and electronic offset were removed. Then these spectra were assembled using the MCST, where the mercury lines or water absorptions in the spectra were used to guarantee the correct spectral alignment in the last step of the MCST assembly procedure. To reduce high-frequency noise, a 20-fold triangular smoothing was applied to all MCST spectra. The combined least squares fit was used to optimize a linear combination of reference spectra (see Table 3.2 for the list of references used in each trace gas analysis) and a polynomial to the logarithm of the atmospheric absorption spectra. The fitting procedure also allowed the spectral shift to compensate for uncertainties of grating position that results from the movement of the grating during an MCST series. All absorption reference spectra were shifted by the same amount, i.e. the spectral shifts of the trace gas references were linked together. The spectral shifts were closely monitored during the analysis to avoid systematic errors, and were typically below the uncertainty of the reproducibility of the grating position of ~ 1 pixel. The numerical details of the analysis procedures used on the MCST absorption spectra have been described in *Stutz and Platt* [1996].

Reference spectra were calculated from literature absorption cross sections using a Mercury emission line to describe the instrument function. These spectra underwent an MCST simulation before including them into the fit. In addition to the trace gas references, a reference spectrum of the lamp emissivity, i.e. the broad Xe emission lines originating from the high pressure Xe arc lamp, and a polynomial were also included in the fit.

Table 3.2. References Used for DOAS Analysis.

Spectral Reference	**Source**
I_2	*Saiz-Lopez et al.*, 2004c
IO	*Hönninger,* 1999
OIO	*P. Spietz, Univ. Bremen, personal communication,* 2005
BrO	*Fleischmann et al., 2004*
NO_2	Reference cell recorded by the instrument at the measurements wavelength interval calibrated with NO_2 absorption cross section reference by *Voigt et al.*, 2002
HCHO	*Meller and Moorgat,* 2000
H_2O	HITRAN, 2004
$C_2H_2O_2$	*Volkamer et al.,* 2005
O_4	*Greenblatt et al.,* 1990
O_3	*Voigt et al.*, 2001

Wavelength intervals used for each trace gas spectral analysis are presented in Table 3.3. These intervals were chosen to minimize structures from Xe emission lines and water absorptions which introduce spectral interferences that are difficult to remove. For example, the wavelength ranges from 546 nm to 547.5 nm and from 553 nm to 559 nm, and from 437 nm to 441 nm, which showed structures that interfered slightly with the fit, were excluded from the OIO/I_2 and IO fits respectively (see figures 3.1.2 3.1.3). Tests that included these windows in the fitting procedure showed increased errors. However, the derived mixing ratios agreed within the errors of the respective fits.

Table 3.3 The Wavelength Window for LP DOAS Data Analysis.

Species	Fitting Window (nm)	Trace gas reference fitted
NO_2	336-371	NO_2, IO, O_4, H_2O, $C_2H_2O_2$
HCHO	303-326	HCHO, BrO, NO_2, H_2O, O_4,O_3
O_3	303-326	HCHO, BrO, NO_2, H_2O, O_4,O_3
NO_3	617-625, 653-668	NO_3, NO_2, O_4, H_2O
IO	423-447.5 (437-441 excluded)	IO, NO_2, O_4, H_2O, $C_2H_2O_2$
OIO	542-565 (546-547.5 and 553-559 excluded)	OIO, I_2, NO_2, O_4, H_2O
I_2	542-565 (546-547.5 and 553-559 excluded)	I_2, OIO, NO_2, O_4, H_2O

The fitting procedure also calculates the errors of the trace gas fit parameters, and therefore the errors in their concentrations, for each absorption spectrum. To take into account problems introduced by random residual structures, the errors calculated by the fit were multiplied by a factor of 3 (details are presented in *Stutz and Platt* [1996]). Since DOAS is an absolute method, i.e. no calibrations are necessary, these errors represent the true error of each measurement. Please note that all statistical errors of the DOAS instruments are reported here as 1σ errors. Systematic errors caused by the instrument are on the order of 3%. The uncertainty of the absorption cross sections varies from 3 to 10%, depending on the trace gas, with the exception of OIO for which the correct value is still under discussion.

Figure 3.1.2 shows the results of the analysis of IO for the LP-DOAS instrument recorded on 10/12/2006 at 16:14 UT. The IO mixing ratio in this absorption spectrum was determined to be 2.0 +/- 0.3 ppt. Figure 3.1.3 shows the result of the OIO analysis of the daytime atmospheric absorption spectrum taken on 10/13/2006 at 13:06 UT. The second panel in Figure 3.1.3 clearly shows the positive identification of the OIO absorption structure in this spectrum, with a mixing ratio of 23.5 +/- 2.2 ppt.

A number of sensitivity studies were performed to ensure the stability of the fitting procedure. Parameters such as the wavelength window, the degree of the polynomial, the degree of smoothing, and the atmospheric reference spectrum were varied. Within the error of the fit, mixing ratios of trace gases typically agreed for these tests. The best spectral window and fitting parameters were chosen as a compromise between a stable fit, i.e. without systematic deviations, and a small statistical error.

In order to further improve the sensitivity of the OIO fit, an atmospheric absorption reference spectrum was also included in the fit. The analysis of the data was therefore relative to the OIO content of this spectrum. The daily references were chosen during times of low or negligible OIO, based on the 1° elevation MAX-DOAS observations. Since the 1° elevation is heavily weighted to the lowest 100 m of the atmosphere, we assumed the instances of low 1° MAX-DOAS OIO Differential Slant Column Densities (DSCDs) to be a good indication of low OIO levels. Additional tests showed that no negative data were found within the statistical uncertainty for the relative analysis of the LP-DOAS data. A comparison between LP-DOAS spectra of low OIO taken at different times and the MAX-DOAS data was used to estimate the upper limit of the OIO mixing ratio of the atmospheric reference used in the fits, which was found to be ~ 8 ppt. A comparison between low OIO LP-DOAS spectra did not reveal any visible OIO absorption structure in these spectra. The OIO upper limit for the atmospheric reference spectra was determined to be similar to or only slightly larger than the uncertainty introduced by the spectral fit. It is important to point out that the disadvantage of additional uncertainty introduced by the relative analysis is greatly diminished by the improved spectral identification of OIO. The clear identification of daytime OIO is not influenced by the relative analysis.

Table 3.4 lists the range of observed mixing ratios for all trace gases detected by the LP-DOAS instrument, together with the respective detection limits.

Table 3.4. Typical Observed LP-DOAS Concentrations and Detection Limits at Zuma Beach.

Trace Gas	Observed levels	Average detection limits
NO_2	0.3 - 43 ppb	0.15 ppb
HCHO	below DL[a] – 7 ppb	0.3 ppb
HONO	0.03 – 0.9 ppb	0.02 ppb
O_3	18 – 64 ppb	3.4 ppb
NO_3	below DL - 70 ppt	1.8 ppt
IO	below DL – 6.7 ppt	0.52 ppt
OIO	below DL – 80 ppt	5.4 ppt

a. DL = detection limit

MAX-DOAS Data Analysis:

The spectral analysis of the MAX-DOAS spectra was performed using the same combination of linear and non-linear least squares fit as for the LP-DOAS analysis [*Stutz and Platt*, 1996]. Table 3.5 presents the wavelength intervals used for detection of different trace gases from the MAX-DOAS spectra. For IO, OIO, and NO_2 evaluations, small intervals were excluded from the fit to minimize interference from the Fraunhofer bands and other spectral interferences in these regions. In addition to the trace gas references, a temporally close zenith spectrum of the same elevation angle sequence as a Fraunhofer reference, and a simulated Ring spectrum [*Vountas et al.*, 1998] were fitted together with a polynomial after a ten fold triangular smoothing low pass filter. The spectral shift of the absorbing trace gases allowed within the fit was performed with one set of parameters, i.e. these reference spectra were linked to each other, to allow for uncertainties in the grating position. These shifts were typically below 1 pixel. Similarly, the

spectral shifts of the Ring and zenith spectra were linked to each other. The spectral shift between these spectra and the low elevation spectrum was statistically indistinguishable from zero since the grating was not moved between these measurements.

All reference absorption cross sections were convoluted using the WinDOAS software with the instrument function determined using a measured Hg line. The convolution process also corrected for the I_0 effect caused by the highly structured solar spectrum [*Aliwell et al.*, 2002]. The references for the absorption cross sections used in the analysis are listed in Table 3.5. The statistical error of the fit was multiplied by a factor of three according to [*Stutz and Platt*, 1997]. Systematic uncertainties by the instrument are below 3%. The absorption cross sections, with the exception of OIO, have an uncertainty of 3 to 10%.

Table 3.5. MAX-DOAS Trace Gases Spectral Evaluation Information.

Trace Gas	Wavelength (nm)	Trace gas references fitted
IO (from 385 nm spectra)	415-438.8 (431-434 excluded)	IO, NO_2, O_4, H_2O, $C_2H_2O_2$
NO_2 (from 385 nm spectra)	413-446	NO_2, O_4, IO, H_2O, $C_2H_2O_2$
O_4 (from 385 nm spectra)	350-389	O_4, NO_2, HCHO, BrO, O_3
O_4 (from 530 nm spectra)	520-589	O_4, NO_2, H_2O, I_2, OIO
I_2 and OIO (from 530 nm spectra)	540.9-566.7(552-558 excluded)	I_2, OIO, O_4, NO_2, H_2O, O_3
HCHO and BrO (from 385 nm spectra)	328-346	HCHO, BrO, NO_2, H_2O, O_4,O_3

Figure 3.1.4 shows the spectral analysis of daytime IO from the 1° elevation viewing angle recorded on 10/11/2006 at 19:26 UT. The IO differential slant column density (DSCD) was found to be 4.09 +/- 0.22 × 10^{13} molec/cm^2. Figure 3.1.5 shows the spectral analysis of daytime OIO from the 1° elevation viewing angle MAX-DOAS spectrum recorded on 10/18/2006 at 19:34 UT. The OIO DSCD was found to be 1.2 +/- 0.11 × 10^{14} molec/cm^2. The detection limits for IO and OIO were 4 × 10^{13} molec/cm^2, and 2 × 10^{13} molec/cm^2 respectively. The conversion of the path integrated slant column densities to vertical profiles of IO and OIO will be discussed in Section 4.5.

3.2 Molecular Halogens by Atmospheric Pressure Ionization Mass Spectrometer (Battelle)

The molecular halogens Br_2, Cl_2, and I_2 were monitored using atmospheric pressure chemical ionization tandem mass spectrometry (APCI-MS/MS, Perkin Elmer-Sciex API-365) in the negative ionization mode. The measurement approach for the halogens has been described elsewhere [*Spicer et al.*, 2002]. The API-365 was optimized for each analyte individually with unit resolution for both quadrupoles. The ion masses in atomic mass units (amu) used for quantification are summarized in Table 3.6. The API-365 was calibrated daily using the output of permeation devices for each molecular halogen (VICI Metronics), which were each housed in separate permeation ovens (Metronics Model 340) held at 30°C for Br_2 and Cl_2 and 100°C for I_2.

Table 3.6. Ions Used for Quantification of Molecular Halogens.

Analyte	Parent/daughter ion pairs used for quantification (amu)	Parent/daughter ion pairs monitored for identification purposes (amu)
Br_2	160/81	158/79
Cl_2	70/35	72/37
I_2	254/127	Not applicable

Sample air was drawn at approximately 8 liters per minute (L/min) through a 2.8 m inlet, which was originally mounted above the roof of the measurement trailer. A shorter 0.8 m inlet was later mounted directly outside the window of the trailer (1.5 m above the ground), and reduced the line losses from ~50% to less than 10%. The inlet was positioned inside an inverted plastic bin to protect it from rain.

Two methods were used to determine the blank values for the molecular halogens during the study. The first method utilized a sodium carbonate-coated annular denuder and the second method flooded the inlet with zero air. Two coating solutions (in methanol) were employed for the carbonate-coated denuder: 1% weight/volume (w/v) sodium carbonate and 1% sodium carbonate with 1% glycerol. Although denuders coated with both solutions effectively removed Br_2 and Cl_2, they were unreliable or acted as a source for I_2, as shown for the API-365 response data in Figure 3.2.1. In an effort to reliably obtain accurate blank measurements, the shorter ambient inlet was reconfigured so that it could be flooded with zero air approximately every 2 hours during ambient measurements. The efficiency for eliminating the iodine signal improved, as shown in Figure 3.2.2, but some elevated iodine blank values were still observed and varied as a function of time. The blank value for I_2 appeared to correlate with ambient temperature, as shown in Figure 3.2.3; the complete removal of bromine indicated that the zero air flow was in excess of the API-365 sampling rate. Temperature-dependent desorption of I_2 from the inlet walls may have been the cause of the variable I_2 blank signal. Simple background subtraction using the average blank value for a given day was used to determine ambient I_2 concentrations.

Detection limits for each molecular halogen were determined daily as the average blank response plus three times the standard deviation of the blank. For I_2, the limit of detection (LOD) ranged from 0.6 to 1.1 ppt. The Br_2 LOD was ~25 ppt. No blank signal for Cl_2 was observed during the study, so this method could not be used to determine the Cl_2 LOD. For reasons that are not clear, the API-365 sensitivity to Cl_2 was very low during this study compared to previous measurement campaigns. The Cl_2 LOD, determined as three times the signal to noise ratio during calibrations, was greater than 230 ppt. For that reason, Cl_2 measurements from the API-365 instrument will not be discussed in the remainder of this report.

3.3 Measurements of VOC (WSU)

3.3.1 PTR-MS.

Continuous measurements of selected volatile organic compounds (VOC) were made with a proton transfer reaction mass spectrometer (PTR-MS). The PTR-MS instrument ran continuously from October 7 to October 24. The PTR-MS is a commercial instrument sold by Ionicon Analytik (Austria). VOCs are measured by chemical ionization, whereby the reagent ion H_3O^+ ionizes organics via a fast proton transfer reaction:

$$R + H_3O^+ \rightarrow RH^+ + H_2O \tag{3.1}$$

The reaction takes place in a drift tube where the sample air stream reacts with H_3O^+ ions produced by a hollow cathode ion source. Compounds that have proton affinities greater than that of water (693 kJ/mol) can in principle be detected by this technique. This includes many polar organic compounds. The instrument is insensitive to the major constituents of air (N_2, O_2, noble gases) and to several pollutant gases (CO_2, CH_4, N_2O, CO, O_3, SO_2, NO_x). It is also insensitive to alkanes < C_9, ethene, and acetylene. For many species the proton transfer reaction is non-dissociative and compounds can be identified by the ion signal at the mass to charge ratio (m/z) that is 1 amu greater than the compound's molecular weight (MW). Other species dissociate upon protonation (e.g., monoterpenes) leading to fragment ions that complicate the interpretation of the PTR-MS mass spectrum. The PTR-MS identifies compounds based on their molecular weight and cannot discriminate between geometric isomers.

The drift tube is pressure and temperature controlled. For these measurements the drift pressure was set at 2.4 mbar, the drift temperature 60 °C, and the drift voltage at 555 volts. The protonated organics are mass analyzed by a quadrupole mass spectrometer and the ions counted by a secondary electron multiplier (SEM). In this experiment a Mascom brand SEM was used.

In theory, the number concentration (molecules cm^{-3}) of the neutral organic (R) in the drift tube can be determined by the following equation:

$$[R] = \frac{1}{kt}\left(\frac{I_{RH^+}}{I_{H_3O^+}}\right)\frac{\varepsilon_{RH+}}{\varepsilon_{H_3O+}} \qquad \text{(E3.1)}$$

where k is the ion-molecule rate constant (molecules cm^{-3} s^{-1}), t is the reaction time (typically of order 100 µs), I_{RH+} and I_{H_3O+} are the respective ion count rates, and ε_{RH+} and ε_{H_3O+} are the ion transmission efficiencies through the quadrupole. The mixing ratio of the R in the sample air is then determined by:

$$\chi_R(ppb) = \frac{[R]}{[AIR]_{drift}} \times 10^9 \qquad \text{(E3.2)}$$

where [AIR] is the number concentration of air (molecules/cm^3) in the drift tube given the drift tube pressure and temperature.

In practice, the sensitivity of the PTR-MS to various VOC is determined by using multicomponent compressed gas standards to establish the ion count rate (I_{RH+}) per ppb of analyte per million Hertz reagent count rates. This is called the normalized sensitivity (SI_{FH+}). A theoretical normalized sensitivity value can be calculated from equation 3.3:

$$SI_{RH+} = [R] I_{H_3O+} kt \left(\frac{\varepsilon_{H_3O+}}{\varepsilon_{RH+}} \right) \qquad \text{(E3.3)}$$

$$SI_{RH+} = \left(4.57 \times 10^{7} \text{ molecules cm}^{-3}\right)\left(1 \times 10^{6} \text{ Hz}\right)\left(2.0 \times 10^{-9} \text{ molecule}^{-1}\text{cm}^{3}\text{s}^{-1}\right)\left(100 \times 10^{-6} \text{ s}\right)\left(\frac{\varepsilon_{H_3O+}}{\varepsilon_{RH+}} \right)$$

$$SI_{RH+} = 9 \text{ Hz}$$

The calculation shows a theoretical normalized sensitivity of 9 Hz / ppb for a H_3O^+ count rate of 1 million Hz, given a rate coefficient of 2×10^{-9} molecule^{-1} cm^3 s^{-1}, a reaction time of 100 μs, and a relative transmission efficiency of unity. In practice, due to differences in ion-molecule rate coefficients and relative transmission efficiencies, different species have different normalized sensitivities. Normalized sensitivities are typically larger for polar oxygenated compounds. Aromatic compounds such as benzene display sensitivities close to that calculated above.

Analyte ions are measured sequentially in a measurement cycle. In a multiple ion detection cycle (MID) the measurement cycle consists of measuring the reagent ion (H_3O^+), other diagnostic ions (O_2^+, NO^+, $H^+(H_2O)_2$), and analyte ions. The instrument repeats this cycle indefinitely storing the data to file. The dwell time (τ) is the length of time the mass spectrometer spends measuring an ion and can be varied to improve the signal to noise ratio. A dwell time of 2 seconds was used for analyte ions in this study. The measurement cycle took 45 seconds to complete. The PTR-MS data files thus consist of a 2 second average of a VOC every 45 seconds. Table 3.7 gives the ions and corresponding organic compounds monitored at Zuma Beach with the PTR-MS. Some of the monitored masses were exploratory measurements to assess PTR-MS measurement capability. Measurements of DMS appear to be subject to a significant mass interference from acetaldehyde water clusters [*deGouw and Warneke*, 2007] and hence were not useful.

Sample air for the PTR-MS instrument was pulled from an inlet approximately 6 feet above the shelter roof through a ½" PFA Teflon sampling line by a diaphragm pump at about 30 L/min. The PTR-MS sampled from this flow at 400 sccm. Zero air was generated by passing ambient air through a heated Pt catalyst trap to remove VOCs. This zero air was used periodically to check instrument backgrounds and to dilute calibration gas to perform spans (every 8 hours). Calibration was done by dynamically diluting a multicomponent compressed gas standard (Scott Marin, stated accuracy ±5%) to approximately 20 ppb levels using humid zero air produced by the catalyst trap. The components of this standard are identified in Table 3.7. All flows were controlled by mass flow controllers and flow rates were verified in the field by measuring them with a precision dry piston flow measuring device (Dri-Cal). The compounds p-xylene, 1,2,4-trimethylbenzene, and 1,2,3,5-tetramethylbenzene are used to represent the average group sensitivities for the sum of C_2-alkylbenzene compounds (xylenes + ethylbenzene), C_3-alkylybenzene compounds, and C_4-alkylbenzene compounds respectively. For compound *j* for which we have no standards we use the normalized sensitivity of calibration compounds with a similar mass (± 5 amu, to account for ion transmission efficiency) multiplied by the ratio of the ion – molecule thermal rate coefficients [*Su*, 1988] to obtain the compound's normalized sensitivity SI_j:

$$SI_j = SI_{RH+}\left(\frac{k_j}{k_{RH+}}\right) \quad \text{(E3.4)}$$

Table 3.7. PTR-MS Measurements.

Ion (m/z)	Species	Calibration Notes & QA Comments
33	Methanol [a]	
42	Acetonitrile [a]	
43	Alkene / alkane fragment ion	$SI = SI_{methanol}$
45	Acetaldehyde [a]	
47	Formic acid + ethanol	$SI = 0.61 \times SI_{acetaldehyde}$
57	Alkane / alkene fragment ion	$S = SI_{isoprene}$
59	Acetone [a] / propanal	
61	Acetic acid	$SI = 0.75 \times SI_{acetone}$
63	Dimethylsulfide	interference due to acetaldehyde water cluster
69	Isoprene [a]	
71	Methacrolein [a] and methyl vinyl ketone	
73	2-butanone [a] / butanal	
79	Benzene [a]	
93	Toluene [a]	
95	Phenol	$SI = 1.3 \times SI_{toluene}$
105	Styrene [a]	
107	C_2-alkylbenzene isomers [a]	
121	C_3-alkylbenzene isomers [a]	
135	C_4-alkylbenzene isomers [a]	
137	Monoterpenes [a]	

a. Indicates analyte present in the Scott-Marin compressed gas standard. For the C_2, C_3 and C_4-alkylbenzene isomers only one isomer was in the standard. Response of other isomers is assumed to be equivalent. Alpha-pinene was used to calibrate monoterpene response. Methacrolein and methyl vinyl ketone are assumed to have the same response.

3.3.2 GC-MS.

An Agilent 6890 gas chromatograph (GC) and Agilent 5973 mass spectrometer (MS) system were employed for in-situ VOC analysis. The GC-MS was used to make measurements of chloroacetone, a marker compound for Cl atom chemistry; a suite of alkanes and aromatic compounds typically found in urban air; and a suite of other compounds that are tracers of coastal water kelp and plankton emissions. The species monitored are listed in Table 3.8. The GC-MS system began collecting data on October 8 and was shut down with the other instruments on October 24. A total of 397 ambient samples were analyzed.

The GC-MS preconcentration system was automated to cryo-collect an ambient sample and inject it into the GC every 45 minutes. A 770 ml ambient air sample was collected onto a pre-concentration loop using an evacuated reference volume. The pressure and temperature of the reference volume were recorded to determine the sampled air volume. The sample was cryogenically trapped in a 1/16” OD by 0.020” ID glass lined stainless steel (Restek Inc) open loop trap. The trap was attached to a heated gas sampling valve (Valco Inc). The cryo-trap was cooled by immersion in liquid nitrogen, which causes immobilization of VOC components and allows passage of oxygen (O_2), nitrogen (N_2), carbon monoxide (CO), and methane (CH_4). The

air sample was dried prior to cryo-trapping by passing the sample stream through a ¼" OD glass lined tube (Restek Inc) cooled to < -45 °C. Air was continuously pulled through this trap at 150 ml /min and flow from the dried air stream was subsampled at ~ 70 ml/min through the cryo-trap. CO_2 was removed by passing the air through a heated Ascarite packed tube prior to cryo-trapping. The sample was injected onto the GC column by switching the gas sampling valve and resistively heating the loop to 100°C in 10 seconds. During the field experiment it was found that the Ascarite trap was removing low levels of chloroacetone (presumably due to absorption onto the wet Ascarite surface) and the trap was removed on October 14. The downside of doing this was CO_2 caused early eluting compounds (i.e., C_5-C_6 alkanes, isoprene, and CH_3Cl) to have poor peak shapes and these species could not be reliably quantified.

A J&W Scientific DB-624 capillary column, 60-m × 0.32 mm ID, 1.80 µm phase thickness was used to separate hydrocarbons in the C_5-C_{12} range. Helium was used as the carrier gas in constant flow mode. The GC was temperature programmed: initial temperature was 35 °C held for 5 minutes, temperature ramp at 6 °C min^{-1} to 180 °C, and temperature held at 180 °C for 5 minutes. The MS was operated in selected ion monitoring mode (SIM). The species were identified by retention time and presence of the identifying quantitation ion shown in Table 3.8. Mixing ratios were calculated from the measured peak area of the quantitation ion, a compound dependent sensitivity factor determined from the daily calibrations, sample blank peak areas, and the volume of air cryogenically trapped. Detection limits listed in Table 3.8 were determined from the variability of the sample blank peak areas, defined as twice the standard deviation of the sample blanks.

Sample blanks were done by sampling the headspace from a liquid N_2 dewar. Typically this gas has very low concentrations of VOCs and allows for a good assessment of trace level contamination of the preconcentration sampling system. Calibrations were done using a 33 component compressed gas standard that was diluted with humidified zero air and cryo-collected in the same way an ambient sample was collected. The zero air source was the same as used for the PTR-MS. The compressed gas standard was purchased from Apel-Reimer Environmental (Denver, CO). Apel-Reimer has extensive experience in the preparation of oxygenated VOC standards and has investigated the stability of some of the Cl atom photoproducts that were to be identified in this study. Based on their experience, the Cl atom photoproducts from isoprene, 1-chloro-3-methyl-3-butene-2-one (CMBO) and the chloromethylbutenal isomers (CMBA), are not stable in canisters or compressed gas cylinders and so were not considered as tracers for Cl atom chemistry in this study. Chloroacetone was considered to be stable and this compound was purchased as a component of the mixture. This compound however proved to be problematic (Apel-Reimer personal communication) and significant loss to the cylinder occurred soon after standard preparation. The chloroacetone concentration in the standard was re-determined at WSU by analyzing the mixture by GC-FID and applying effective carbon number response factors to determine the chloroacetone concentration in the cylinder. No further decrease in chloroacetone concentration was observed. Calibration factors for the species DMS, carbon disulfide (CS_2) and bromoform ($CHBr_3$) were determined from a TO-15 standard (Scott Specialty Gases, stated accuracy ± 10%). This standard also contained toluene. Relative response factors for these species relative to toluene were determined after the field experiment. It was assumed that iodoform had the same relative response as bromoform.

Table 3.8 Species Measured by GC-MS.

#	Species	Retention Time (min)	Quantitation Ion	Detection Limit
1	2,2-dimethylbutane	8.67	71	15
2	Dimethylsulfide	9.03	62	2
3	Carbon disulfide	9.04	76	2
4	dichloromethane	9.83	84	6
5	1,1,1-trichloroethane	14.04	97	10
6	2-methylhexane	14.06	85	3
7	3-methylhexane	14.47	71	2
8	benzene	14.87	78	11
9	2,2,4-trimethylpentane	15.05	57	2
10	heptane	15.44	71	4
11	chloroacetone	17.18	92	4
12	2,3,4-trimethylpentane	17.69	71	2
13	toluene	19.21	91	17
14	octane	19.43	85	6
15	iodoform	21.0	127	2
16	ethylbenzene	22.76	91	5
17	nonane	23.04	57	4
18	m,p-xylene	23.04	91	21
19	o-xylene	24.02	91	9
20	bromoform	24.45	173	2
21	isopropylbenzene	24.9	105	4
22	a-pinene	25.61	93	2
23	3-ethyltoluene	26.13	105	10
24	4-ethyltoluene	26.2	105	15
25	decane	26.32	57	12
26	1,3,5-trimethylbenzene	26.34	105	10
27	2-ethyltoluene	26.88	105	8
28	1,2,4- trimethylbenzene	27.3	105	10
29	1,2,3- trimethylbenzene	28.38	105	10
30	n-butylbenzene	29.12	91	10

3.3.3 Canister Sampling

Canisters were collected from the UCLA campus and the CELA monitoring station using a Xontech, Inc. autosampler that could be programmed to fill canisters at selected times. Thirty-six canisters were filled at each site for a total of 72 canisters. Canisters were filled 4 times per day per site using half hour fill times. The sampling times provide data on VOC distributions during the morning, afternoon, and evening. The fill times were: 02:45 to 03:15 representing a nighttime sample, 06:45 to 07:15 representing conditions at sunrise, 07:15 to 07:45 representing rush hour, and 14:45 to 15:15, representing afternoon conditions. Table 3.9 gives the canister sample collection periods. Canisters were not collected on rainy days.

The cans were returned to WSU and analyzed by GC-MS for the same list of compounds shown in Table 3.9 and for light hydrocarbons (C_2-C_6 alkanes, alkenes, alkynes) by gas

chromatography and flame ionization detection (GC-FID). Compounds were separated on a 50-m Al_2O_3/KCl PLOT column. A 500 cc sample was cryo collected on a glass bead packed trap. Water and CO_2 were removed prior to sample collection by cooling the air stream to -50 ˚C and then passing it through a heated Ascarite filled tube to remove CO_2. The Ascarite trap was replaced daily. FID carbon response was calibrated using a NIST certified standard of 2,2-dimethylbutane (neohexane) with stated accuracy of ± 10%.

For this study, 12 Silonite coated canisters were purchased from Entech Instruments. It was believed that these canisters would prove better at storing oxygenated species such as chloroacetone than the older SUMMA polished canisters in the WSU inventory. As discussed in Section 4.3, this proved to be correct but in an unexpected way. Based on replicate sample runs over time, chloroacetone increased significantly in the older SUMMA polished canisters but not in the Silonite coated canisters. These Silonite canisters are identified by bold face type in Table 3.9.

3.4 Optical Particle Counter (WSU)

Particle size distribution measurements were made with a TSI Aerodynamic Particle Sizer (APS) model 3320. The APS measures particles in the size range 0.5 to 20 μm. Particle number concentration is determined for 52 size bins spanning this range, and data are reported as particle concentration per cm^3 for each of the 52 bin sizes. Bin sizes are identified by their median aerodynamic particle size. Aerodynamic particle size is determined by a time of flight experiment, in which particles are accelerated through an optics chamber containing two laser beams. The particles are detected from the scattered light and their velocity is determined by differences in the timing of measured scattered light pulses from the two beams. From the measured velocity, the APS determines the aerodynamic particle diameter from an internal calibration based on polystyrene latex spheres. For the lowest size range, 0.3 to 0.523 μm, total particle concentration is determined from the measured scattered light.

The APS instrument was housed in a waterproof case with the instrument's short inlet protruding through a weatherproof seal in the case. A "rain hat" shielded the inlet from weather without affecting sampling airflow. The instrument was placed on the roof of the sampling shelter. Size distribution data were collected as 1-minute averages from October 6 to October 14, 2006 and changed to 5-minute averages from October 14 to the end of sampling on October 24. The instrument ran continuously from late afternoon of October 6 to the morning of October 24. No data were collected for October 10 and for the period between October 19 15:00 to October 20 02:00 due to data logging computer malfunctions.

Table 3.9. Canister Sampling Schedule.

Date	Start	Stop	UCLA Can #	CELA Can#
10/12/2006	02:45	03:15	53	P20
	06:45	07:15	36	70
	07:15	07:45	189	97
	14:45	15:15	P43	65
10/13/2006	02:45	03:15	P41	130
	06:45	07:15	615	P5
	07:15	07:45	82	P18
	14:45	15:15	316	T14
10/15/2006	02:45	03:15	**6900** [a]	T21
	06:45	07:15	**6908**	63
	07:15	07:45	**6901**	T13
	14:45	15:15	**6904**	T5
10/16/2006	02:45	03:15	**6905**	T26
	06:45	07:15	**6902**	T18
	07:15	07:45	**6907**	T27
	14:45	15:15	118	T16
10/17/2006	02:45	03:15	74	112
	06:45	07:15	**6906**	106
	07:15	07:45	**6896**	P48
	14:45	15:15	61	86
10/18/2006	02:45	03:15	BAI 224	125
	06:45	07:15	BAI 265	T28
	07:15	07:45	BAI 267	T20
	14:45	15:15	BAI 224	309
10/19/2006	02:45	03:15	BAI 223	281
	06:45	07:15	BAI 102	**6894**
	07:15	07:45	BAI 237	**6899**
	14:45	15:15	BAI 226	123
10/20/2006	02:45	03:15	BAI 299	49
	06:45	07:15	BAI 200	**6998**
	07:15	07:45	BAI 230	P13
	14:45	15:15	BAI 269	69
10/21/2006	02:45	03:15	BAI 240	P9
	06:45	07:15	BAI 222	34
	07:15	07:45	BAI 107	P38
	14:45	15:15	BAI 212	86

a. bold type face indicates Entech Silonite coated canisters

3.5 In-Situ measurements of CO, O_3, NO, and NO_y

CO was measured using a Thermo Environmental Model 48C continuous analyzer. The measurement principle of the 48C is cross filter correlation infrared spectroscopy. The instrument was used with a 2 ppm operating range and its calibration was set using a 1.6 ppm dynamic dilution from a certified compressed gas standard (Scott Specialty Gases, 442.6 ppm ± 1% CO). Zero air (less than 0.1 ppm total hydrocarbons, Lehrner Martin) was used to set the zero; the calibration and zero values were checked at least weekly. The ambient air encountered at the field site frequently contained less CO than the zero air cylinders used to set and check the zero value. All measurement data were offset by 0.4765 ppm, which was the lowest measurement value observed during the study. However, this minimum was influenced by the lower range of the analog output of the analyzer and therefore biases the resulting data, which should be considered the minimum concentrations. The general trends and variability still have value, except at low concentrations, although the absolute concentrations cannot be determined. The CO LOD was not determined since the data cannot be used quantitatively.

Concentrations of NO and NO_y were quantified in real-time using a Thermo Environmental Model 42S chemiluminescence monitor. The instrument, which is manufactured to detect NO and NO_2, was modified in-house with an external converter to quantify all oxides of nitrogen, including NO and nitric acid. The converter was positioned approximately 1 m above the roof of the instrument trailer. An inverted plastic bin was used to protect the inlet and converter box from rain. The instrument sampled at a flow rate of 1.2 L/min and the instrument's range was set at 200 ppb for the study. Before ambient monitoring began, the instrument was calibrated with a 160 ppb dynamic dilution from a certified gas standard (Scott Specialty Gas, 44.53 ppm ± 1% NO) and the zero was set using zero air (less than 0.1 ppm total hydrocarbons, Lehrner Martin). The calibration was checked at least once per week during the study. It was discovered that the zero air cylinders contained more NO than was occasionally present in the ambient air; an offset ranging between 1.1 and 2.4 ppb was applied to the data, depending on the specific cylinder used to set the analyzer zero value. The estimated LOD values for NO and NO_y were approximately 2 and 3 ppb, respectively.

The UCI group also deployed a Thermo Environmental ozone and NO monitor. Details on these measurements can be found in *Finley* [2007].

3.6 Meteorological Data and Actinic Fluxes

Meteorological data were collected at the field site, approximately 2 meters above the roof of one of the office containers using an Onset weather station. Parameters measured include wind direction and speed, temperature, pressure, relative humidity, and solar radiation. Measurements were taken at one-minute intervals throughout the experiment.

Actinic fluxes were also measured, in particular the photolysis rates of NO_2 and O_3, using a MetCon spectroradiometer borrowed from the Pacific Northwest National Laboratory (PNNL). Actinic fluxes were measured on the roof of one of the containers with a 5 minute time resolution from October 15 to October 23 with some interruptions due to problems with the instrument computer.

3.7 Molecular Halogens by Mass Spectrometry (UCI / NSF)

The group of Eric Saltzman from the University of California Irvine (UCI) joined us in our Malibu field effort, bringing their APCI-MS system to measure molecular halogen compounds. Details of the instrument can be found in *Finley* [2007].

3.8 Particle Sample and Ionic Composition by Neutron Activation Analysis (PNNL, UNH / NSF)

Aerosol sampling for compositional analysis was carried out using the Time-Resolved Aerosol Collector (TRAC) [*Laskin et al.*, 2003]. The TRAC sampling device impacts particles directly onto electron microscopy grids for analysis of individual particle morphology and elemental composition. Air was sampled onto an individual electron microscopy grid for 20 minutes. A sampling disk housed 550 grids and particles were deposited onto each grid sequentially in time. In this way, continuous sampling with the TRAC was done from 12:40 on October 9 to 15:54 on October 17 on "disk 1" and from 19:44 on October 17 to 14:34 on October 24 on "disk 2".

The TRAC samples were returned to the Environmental Molecular Sciences Laboratory (EMSL) located at PNNL for analysis. The analysis consisted of surveys whereby certain grids were selected to examine particle morphology and composition using scanning electron microscopy (SEM) for particle imaging and energy dispersive x-ray analysis (EDAX) for determining elemental composition of individual particles. Seventeen grids from disk 1 and 15 grids from disk 2 were examined based on measurements of gas phase species that indicated interesting events or clean or polluted conditions.

In addition to the TRAC sampling, Alex Pszenny from University of New Hampshire (UNH) performed 24 hour Hi-Vol sampling of $PM_{2.5}$ to determine elemental composition of particles by neutron activation analysis and ion chromatography. The data provide quantitative measurements of major elements expected to be found in sea-salt particles (i.e. Na, Cl, Br) and several trace metals that are tracers of pollution sources (e.g., V).

4 Observations

4.1 Meteorological conditions during CalHal

Figure 4.1.1 provides an overview of meteorological measurements performed at Zuma Beach at the time of the experiment. A land-sea breeze pattern dominated during the first week of the experiment (October 8 to 17, 2006). The wind direction reversals normally take place at 9 to 10 a.m. as land warms after sunrise and between 8 and 9 p.m., after the sunset. Figures 4.1.2 and 4.1.3 show wind speed/wind direction dependency observed at Zuma Beach during the first ten days of the experiment during day and night respectively. Temperatures during this first part of the experiment varied between 15 and 20 °C while the relative humidity was around 80%. As indicated by solar radiation, many of the days from October 8 to October 17 were cloudy, with the exception of October 11, 12, and 17.

On October 18 to 21 the weather pattern changed to predominantly off-shore flow ("Santa Ana" event). During this time wind speeds were higher than during the previous days and there was no clear on-shore off-shore pattern. This Santa Ana event can also be distinguished by the low relative humidity and higher temperature and atmospheric pressure values. These days were clear. The Santa Ana event was followed by foggy and cloudy days during the end of the experiment.

4.2 Ozone, NO_x, NO_y, CO, and HCHO

Figure 4.2.1 shows concentrations of various pollutants measured by the LP-DOAS and various in-situ instruments at Zuma Beach during the experiment. Low pollutant levels occurred during the first half of the experiment. Ozone as measured by the LP-DOAS and the in-situ monitor agreed well and showed mixing ratios around 40 ppb at night. Daytime mixing ratios were slightly higher, reaching 50 to 60 ppb. The higher daytime values indicated that the Zuma Beach site was influenced by pollution even during the first, relatively clean part of the experiment.

NO and NO_2 mixing ratios varied according to the wind direction with daytime mixing ratios below 1 ppb during the first part of the experiment (Figure 4.2.2). The minimum daytime NO_2 value below 100 ppt was observed on October 11, 2006. Nighttime values were generally higher, in the range of 5 to 10 ppb. Higher NO_2 levels at night can most likely be attributed to the flow reversal bringing polluted air from the LA Basin to the site. This behavior is also reflected in the NO_y data. During the Santa Ana event, from October 18 to October 21, 2006 NO, NO_2, and NO_y mixing ratios were considerably higher with maximum values in the range of 40 to 150 ppb (Figure 4.2.2). NO values, in particular during the night, sometimes show local emissions, i.e. sharp peaks, due to cars passing near the site. The NO_2 values of the two in-situ instruments agreed fairly well, as did the DOAS NO_2 and in-situ NO_2. While we did not perform a formal intercomparison the comparison shown in Figure 4.2.2 gives us confidence in the measurements.

The LP-DOAS also measured HONO (Figure 4.2.1), which was below the detection limit during the day and reached ~200 ppt at night during the first part of the experiment. The second half of the experiment was characterized by higher pollution levels. In particular during the Santa Ana event air from the South Coast Air Basin was observed, and concentrations of all pollutants were quite high. NO_2 mixing ratios reached 45 ppb on October 20. Ozone showed a much more pronounced diurnal variation, with low mixing ratios at night and daytime maxima at ~70 ppb.

HONO mixing ratios during this period reached above 0.5 ppb. The last few days of the experiment were characterized by foggy days, which made LP-DOAS measurements impossible.

HCHO levels, as observed by the LP-DOAS, were between 0.3 and 2 ppb during the first half of the experiment, showing a diurnal cycle with higher mixing ratios during the night than during the day, due to the land/sea breeze system. HCHO mixing ratios were more consistently at and above 2 ppb during the second half of the experiment and reached 7.5 ppb during the Santa Ana event on October 20, when air processed in the LA Basin was observed at Zuma beach.

Figure 4.2.2 also shows the NO_2 photolysis rates measured in the second half of the experiment. The observed values are in the range expected for the location and the time of the year (i.e., up to 0.007 sec^{-1}).

4.3 VOCs

4.3.1 Canister samples

Canister samples were collected on the roof top of an 11 story building on the UCLA campus and at the Los Angeles North Main Street monitoring site (ARB site # 70087), which we identify in this report as CELA. Table 4.1 lists the median mixing ratios determined from the two sites for each sampling period. The CELA site had much higher hydrocarbon concentrations as expected given the proximity of the site to busy roads. The data from CELA was used to define source ratios of selected hydrocarbons to compare with the Zuma Beach data set to determine impacts of Cl atom chemistry on the LA plume.

The primary purpose of the canister sampling was to determine the presence of Cl atom chemistry through the measurement of Cl atom chemistry photoproducts such as chloroacetone. Figure 4.3.1 shows the time series of chloroacetone mixing ratios from both sites. Mixing ratios ranged from below detection limits to surprisingly high levels over 600 ppt. Replicate sampling of 13 canisters 4 to 6 months after the first analysis was performed to determine chloroacetone stability; the results are shown in Figure 4.3.2. This time frame is similar to the time between canister sampling and the first analysis. Interestingly, chloroacetone mixing ratios typically increased as a function of storage time in many of the canisters, indicating production within the canister. Canisters are known to produce oxygenated species and it appears that chloroacetone can be produced in canisters as well. In several canisters containing low levels of chloroacetone (< 25 ppt), chloroacetone decreased with the storage time. Our assessment of the chloroacetone data is to use the data from the Silonite treated canisters purchased from Entech for this project and to disregard the chloroacetone data from the other canisters due to uncertainty resulting from positive artifact formation. The replicate samples from the Silonite treated canisters displayed no dramatic increase in chloroacetone with storage time and in general yielded the lowest overall levels of chloroacetone, as shown in Figure 4.3.1.

Table 4.1 Median Mixing Ratios from Canister Sampling at UCLA and CELA in ppb

	CELA				UCLA			
Species	**02:45**	**06:45**	**07:15**	**14:45**	**02:45**	**06:45**	**07:15**	**14:45**
ethane	11.40	13.76	14.63	8.16	4.09	4.76	5.73	2.57
propane	7.01	8.88	8.20	3.42	1.94	1.35	2.34	3.51
iso-butane	1.84	1.62	1.63	0.66	0.41	0.30	0.39	0.71
n-butane	2.04	2.06	1.91	1.10	0.81	0.22	0.51	0.42
iso-pentane	2.66	3.94	4.22	1.30	0.56	0.30	0.36	0.31
n-pentane	1.09	1.40	1.55	0.53	0.50	0.11	0.18	0.16
2,2-dimethylbutane	0.09	0.18	0.20	0.05	0.05	0.04	0.05	0.04
2-methylhexane	0.13	0.23	0.26	0.07	0.17	0.05	0.07	0.07
3-methylhexane	0.13	0.25	0.28	0.07	0.11	0.14	0.07	0.06
methylcylopentane	0.53	0.78	0.90	0.22	0.04	0.10	0.03	0.03
cylcohexane	0.26	0.45	0.45	0.13	0.19	0.23	0.13	0.13
2,2-dimethylbutane	0.23	0.42	0.44	0.09	0.08	0.19	0.06	0.06
2-methylpentane	1.12	1.79	1.99	0.46	0.16	0.05	0.07	0.06
3-methylpentane	0.49	0.78	0.90	0.21	0.03	0.02	0.02	0.03
hexane	0.44	0.63	0.72	0.21	0.03	0.01	0.02	0.02
heptane	0.14	0.23	0.25	0.10	0.05	0.03	0.03	0.05
2,3-dimethylpentane	0.30	0.38	0.53	0.10	0.04	0.00	0.03	0.04
2,2,4-trimethylpentane	0.29	0.54	0.60	0.13	0.04	0.02	0.02	0.04
2,3,4-trimethylpentane	0.09	0.18	0.19	0.03	0.01	0.01	0.01	0.01
octane	0.06	0.10	0.09	0.04	0.02	0.01	0.02	0.02
nonane	0.07	0.09	0.10	0.05	0.04	0.01	0.03	0.04
decane	0.10	0.13	0.14	0.07	0.06	0.01	0.06	0.04
ethylene	3.72	8.04	8.61	1.90	1.53	2.05	1.03	1.48
acetylene	2.52	6.38	6.77	1.33	0.60	0.48	0.53	0.52
propene	1.27	3.06	2.58	0.68	0.54	0.64	0.45	0.63
t-2-butene	0.07	0.17	0.15	0.03	0.00	0.00	0.00	0.00
i-butene	0.17	0.34	0.33	0.20	0.07	0.00	0.04	0.14
isobutylene	0.44	0.80	0.97	0.37	0.22	0.18	0.18	0.25
c-2-butene	0.07	0.15	0.13	0.04	0.00	0.00	0.00	0.00
isoprene	0.05	0.05	0.06	0.04	0.01	0.00	0.00	0.08
i-pentene	0.11	0.14	0.16	0.11	0.04	0.03	0.03	0.03
Alpha-pinene	0.24	0.21	0.26	0.02	0.02	0.01	0.04	0.02
benzene	0.36	0.65	0.65	0.16	0.09	0.07	0.07	0.08
toluene	1.23	1.77	1.88	0.63	0.23	0.12	0.18	0.24
ethylbenzene	0.165	0.272	0.341	0.062	0.020	0.013	0.035	0.027
p-xylene	0.698	0.960	1.254	0.204	0.078	0.041	0.111	0.089
o-xylene	0.244	0.359	0.475	0.078	0.032	0.014	0.044	0.033
isopropylbenzene	0.011	0.017	0.023	0.004	0.002	0.001	0.002	0.003
3-ethyltoluene	0.106	0.202	0.171	0.038	0.016	0.001	0.009	0.014
4-ethyltoluene	0.081	0.130	0.129	0.033	0.025	0.006	0.012	0.017
1,3,5-trimethylbenzene	0.097	0.162	0.209	0.045	0.027	0.011	0.028	0.019
2-ethyltoluene	0.038	0.075	0.064	0.017	0.008	0.001	0.003	0.008
1,2,4-trimethylbenzene	0.357	0.564	0.669	0.130	0.198	0.037	0.090	0.101
1,2,3-trimethylbenzene	0.034	0.061	0.056	0.012	0.009	< DL	0.006	0.003
dichloromethane	0.245	0.261	0.246	0.168	0.083	0.064	0.050	0.051
1,1,1-trichloroethane	0.014	0.014	0.016	0.012	0.011	0.010	0.011	0.011
chloroacetone	0.061	0.060	0.034	0.067	0.118	0.012	0.012	0.048

Table 4.2 compares average chloroacetone mixing ratios in the Entech canister samples to the other canister samples. For both LA locations the Entech canister samples yielded chloroacetone mixing ratios about a factor of 10 lower than the other canisters. We believe that the samples collected in the Entech cansisters are the best guide to establishing chloroacetone mixing ratios in Los Angeles. Six of the twelve Silonite treated canisters yielded chloroacetone above the detection limit (4 ppt) with the two sites yielding similar ranges. For the samples above the detection limit, the average chloroacetone mixing ratio in the Entech canisters was found to be 11 ppt. The observation of significant chloroacetone levels in these cans suggests that Cl atom chemistry is occurring in urban air.

Table 4.2 Chloroacetone in Canister Samples

	CELA	**UCLA**
Total # can samples	35	36
# Entech type canisters	3	9
# non-Entech type canisters	32	27
# Entech canister samples > DL (4 ppt)	3	3
% Entech canister > DL (4 ppt)	100%	33%
Average chloroacetone in Entech canisters	8 ppt	13 ppt
Non-Entech canister samples > DL (4 ppt)	30	27
% non-Entech canister samples > DL (4 ppt)	94	100%
Average chloroacetone in non-Entech canisters	87 ppt	123 ppt

For the conditions of the field experiment the chloroacetone lifetime is estimated to be ~ 1.2 days. The lifetime is principally determined by photolysis. The lifetime against photolysis is estimated to be 35 hours, as determined from published absorption cross sections [*Burkholder et al.*, 2002] and calculated UV photon fluxes for mid October at this latitude from the NCAR TUV calculator. The OH rate coefficient at 298 K has been measured to be 4.2×10^{-13} $cm^3 molecule^{-1}$ s^{-1} ± 20% (*Carr et al.*, 2003). Given an OH concentration of 5×10^6 molecules cm^{-3} for the urban environment, this yields a lifetime against OH attack of about 5.5 days.

Hydrocarbon trends from the canister samples were examined to determine if a Cl atom chemistry signature was evident. The analysis approach was to examine the correlations of species with similar OH rate coefficients but with significantly different Cl atom rate coefficients. Several pairs of hydrocarbons were identified as meeting this criterion including iso- and n-alkanes with the same carbon number. Isoalkanes react more slowly with Cl atoms than do the corresponding n-alkanes. These species are shown in Table 4.3.

Figure 4.3.3 shows correlations from the canister sample data set (UCLA & CELA sites) between species with similar OH rate coefficients but different Cl atom rate coefficients. The trends are compared to the auto exhaust source ratio determined from published tunnel studies [c.f. *Jobson et al.*, 2004]. The dynamic range of the data is determined by atmospheric processing, which includes dilution and mixing of roadway sources into the PBL and their subsequent photochemical processing. For species with similar atmospheric lifetimes, atmospheric processing will not change the relative amounts of the plotted species, and the data should trend along the source ratio line. With the exception of the i-butane vs. n-butane plot, the data do indeed agree reasonably well with the auto exhaust source ratio over the 2 orders of magnitude range in mixing ratios observed. The higher i-butane to n-butane ratio is typical for

urban areas that also have contributions from other sources, such as natural gas. There is no consistent evidence in Figure 4.3.3 of the trend lines deviating systematically from the source ratio, which would suggest a significant difference in their lifetimes due to Cl atom processing. This is perhaps to be expected since the dynamic range of the data in an urban environment is likely largely determined by atmospheric dynamics (dilution and mixing) and emissions rate variability rather than chemical processing.

Table 4.3 Indicator Hydrocarbon Pairs: Reaction Rate Constants at 298 K

Species	**$k_{OH} \times 10^{-12}$** (molecule^{-1} cm^3 s^{-1})	**$k_{Cl} \times 10^{-10}$** (molecule^{-1} cm^3 s^{-1})	**Ratio OH rate coefficients**	**Ratio Cl rate coefficients**
i-butane	2.16 [a]	1.40 [a]	0.88	0.67
n-butane	2.45 [a]	2.10 [a]		
i-pentane	3.74 [a]	2.10 [a]	0.94	0.78
n-pentane	3.97 [a]	2.70 [a]		
3-methylpentane	5.54 [a]	2.69 [a]	1.05	0.82
hexane	5.28 [a]	3.30 [a]		
2-methylhexane	6.78 [b]	3.38 [a]	1.04	0.89
3-methylhexane	7.15 [b]	3.16 [b]	1.10	0.83
heptane	6.52 [a]	3.80 [a]		
2,3,4-trimethylpentane	6.60 [a]	2.63 [b]	0.85	0.60
octane	7.81 [a]	4.40 [a]		
benzene	1.22 [c]	1.3×10^{-6} [d]	0.22	2.3×10^{-7}
ethylbenzene	7.00 [c]	1.15 [e]	1.24	0.20
toluene	5.63 [c]	5.75 [f]		

References to rate coefficient values:

a. "Mechanisms of Atmospheric Oxidation of the Alkanes", Ed. J. Calvert., Oxford University Press, New York, 2008.
b. Calculated from structure activity relationships, OH: Atkinson et al., 1987 ; Cl: Tyndall et al., 1997.
c. "Mechanisms of Atmospheric Oxidation of Aromatic Hydrocarbons", Ed. J. Calvert, Oxford University Press, New York, 2002.
d. *Sokolov et al.,* 1998.
e. *Anderson et al.,* 2007
f. Average of two studies: *Shi and Bernhard*, 1997; *Wallington, Skewers and Siegel*, 1988.

4.3.2 Zuma Beach VOCs

The first 10 days of sampling at Zuma Beach were characterized by clean marine air. In the later period, wind flow brought air from the LA Basin to the site as evidenced by large increases in VOC mixing ratios and increases in CO and NO_x. Figure 4.3.4 shows a time series of sum of the C_3-alkylbenzene isomers measured by the PTR-MS, representative of a short lived urban air tracer, and mixing ratios of dichloromethane by GC-MS, representative of a longer-lived urban air tracer. For the period from October 19 to October 24, mixing ratios of both species were

elevated indicating the impact of the Los Angeles Basin air. This is consistent with observed increases in NO_x and CO during this period.

During the clean air period, it was evident that many VOCs displayed a diel cycle driven by the sea breeze circulation. This was most pronounced for monoterpenes, measured by the PTR-MS as the ion signal at m/z =137. Monoterpenes are emitted from vegetation and elevated mixing ratios were often seen at night when mixed layer heights were at a minimum. Figure 4.3.5 shows a time series of monoterpene mixing ratios along with those of isoprene, a compound emitted by vegetation during the day, and the sum of methacrolein (MACR) and methylvinylketone (MVK), which are oxidation products of isoprene. Monoterpene mixing ratios were much higher at night (typically > 1 ppb) compared to the daytime (typically < 0.1 ppb). Time series plots for other VOCs measured by the PTR-MS are given in Figures 4.3.6 through 4.3.8.

The time series of chloroacetone measurements is given in Figures 4.3.9 and 4.3.10. Chloroacetone was significantly above detection limits for three periods: the clean air period between October 9 and October 10, the clean air period between October 16 and October 18, and the polluted period between October 19 and October 24 when LA Basin air was being sampled. Mixing ratios of chloroacetone during the polluted period were up to 16 ppt, similar to the average levels observed in the Silonite canister samples collected in Los Angeles. During the pollution event, chloroacetone was reasonably well correlated with other hydrocarbons. Correlations with toluene (short lived urban tracer) and dichloromethane (long lived urban tracer) are shown in Figure 4.3.11. The positive correlation suggests that either chloroacetone is being transported out of the urban area or that it is being produced during transport to the site. It was not clear what the source of chloroacetone was during the clean air periods, which were obviously unconnected with urban air chemistry and so chloroacetone must be produced from local marine/coastal photochemistry. It has been reported that chloroacetone is a major oxidation product of Cl atom initiated oxidation of MACR [*Tyndall et al.*, 2003], which was measured at sub-ppb levels at the site. Thus, there may be a source of chloroacetone from the photoprocessing of biogenic emissions in coastal environments.

To better understand if the LA Basin outflow period was being photochemically processed by Cl atoms, tracer relationships were examined for tell-tale Cl atom kinetic signatures. Correlations between hydrocarbons with similar OH rate coefficients but significantly different Cl atom rate coefficients are plotted in Figure 4.3.12. (The exception was the benzene vs. toluene plot; these compounds have significant differences in their OH rate coefficients.) Also shown in these plots is the source ratio, determined as the average ratio of these species from the CELA canister samples. In all the plots, there was a strong correlation between the plotted pairs. The data follow the source ratio line over at least an order of magnitude in mixing ratio. Under Cl atom processing, the data would be expected to deviate from the source ratio line since the species would be removed from the atmosphere at significantly different rates. For the plots in Figure 4.3.12, the species plotted on the y-axis has the smaller Cl atom rate coefficient so the data would follow a trend with a slope less than that of the source ratio line for Cl atom oxidation. There is no evidence from these plots of such a deviation. For the benzene vs. toluene plot, the data deviate from the source ratio line but this would be expected for OH reaction chemistry alone. Benzene is essentially unreactive with Cl atoms.

The sensitivity of tracer relationships for identifying oxidant signatures depends on the photochemical age of the air, defined as the product of processing time and oxidant

concentration. If this value is small, the relative changes in abundance that would indicate chemical processing will be difficult to observe. The data in Figure 4.3.12 span more than an order of magnitude change in mixing ratio, but a lot of this variability may be due to differences in dilution, mixing, and emissions, rather than photochemical removal. Thus, the data and interpretation of the trends may not be sensitive to Cl atom kinetics because the dynamic range is being driven by dilution rather than chemical processing. One way to assess the relative roles of mixing and chemistry in shaping trace gas distributions is to examine the relationship between temporal variability and lifetime [*Jobson et al.*, 1994; 1999]. Variability/lifetime relationships are power law relationships. For well mixed air removed from immediate sources of hydrocarbons, mixing ratio variability scales as the inverse of the square root of the lifetime: $\tau^{-0.5}$. For sites closer to urban areas, variability displays a weaker dependence on lifetime, indicating a lesser role for chemistry in shaping concentration change. The metric for comparing variability amongst tracers that display a wide range in mixing ratios is the standard deviation of the natural log transformed mixing ratio data (Slnx). The ln-transform is done to transform the mixing ratio distributions from log-normal to Gaussian. The standard deviation of these Gaussian distributions is a meaningful metric to compare tracer variability. Such a plot is shown in Figure 4.3.13. The tracer lifetimes were estimated from an assumed OH concentration and their known OH reaction rate coefficients. The power law exponent is not sensitive to the absolute value of the lifetime. The data in Figure 4.3.13 are reasonably well correlated with the OH lifetime, again suggesting the absence of a significant Cl atom processing signature. A fit to the data yields a $\tau^{0.09}$ dependence, implying a very weak OH chemical signature in the data. The variability of the data in the LA basin outflow period is being driven principally by atmospheric dynamics and emissions and not by OH chemistry. Given the weak OH dependence, we conclude there may not have been enough processing time of the LA basin outflow through the marine environment to observe a Cl atom signature in the tracer relationships.

4.4 NO_3 and N_2O_5

NO_3 was also observed in Malibu during many nights. During the first half of the experiment nocturnal NO_3 mixing ratios were between 5 and 15 ppt, with a short period of 30 ppt on the night of October 13 (Figure 4.2.2). During the second, more polluted half of CalHal, NO_3 mixing ratios were much higher, varying between 10 to 50 ppt, and reaching up to 70 ppt during the Santa Ana event. The NO_3 mixing ratios generally followed other pollutants, particularly NO_2. The very dry conditions during the Santa Ana events also contributed to the high NO_3 since the loss of NO_3 due to N_2O_5 uptake is small. We also calculated the steady state mixing ratio of N_2O_5, based on the LP-DOAS measurements of NO_2 and NO_3 (Figure 4.2.2), and the temperature. N_2O_5 mixing ratios during the first half of the experiment varied between 10 and 50 ppt. During the second half they often reached 100 to 600 ppt at night.

At the observed levels of NO_3 and N_2O_5, nocturnal chemistry becomes important, as will be discussed below. In addition, one has to consider the formation of $ClNO_2$, a photolytic precursor of chlorine atoms.

4.5 Halogen Oxides

Halogen oxides were measured by both DOAS instruments at Zuma Beach. The LP-DOAS measured BrO, IO, and OIO during day and night while the MAX-DOAS measured BrO, IO, and OIO only during the day. The following sections summarize our observations during CalHal. Because the high pollutant concentrations in the second half of the experiment, i.e. the relatively

high concentrations of NO_2, interfered with the sensitive analysis of the iodine oxides, our discussion will be focused on the first half of the experiment. It should be noted that the reaction of NO_2 with all halogen oxides makes it very unlikely that these compounds were present during the very polluted second half of the experiment.

4.5.1 BrO

BrO was not observed above the detection limit of the LP-DOAS of ~1 ppt. The MAX-DOAS also did not observe BrO. This is not surprising since the presence of 1 ppb or higher NO_x levels at Malibu would have shifted the BrO-$BrONO_2$ equilibrium towards bromine nitrate. Thus we cannot conclude that bromine chemistry was absent, but rather that the DOAS systems were not able to detect BrO.

4.5.2 IO and OIO Concentrations and DSCDs

The LP-DOAS detected IO during the day and night at comparable levels (Figure 4.5.1). On average, up to 3 ppt of IO was present in the marine boundary layer at Zuma Beach. The MAX-DOAS instrument detected IO as well, showing a clear separation between elevation viewing angles (Figure 4.5.1). OIO was also detected by both the LP and MAX-DOAS instruments during the day, and LP DOAS also measured OIO at night (Figure 4.5.1). On most nights, OIO levels were slightly lower than during the day. Daytime OIO levels ranged from 15 to 30 ppt, while nighttime OIO ranged from 5 to 15 ppt. The IO and OIO levels were similar to those our group observed in the Gulf of Maine in 2004. A detailed discussion of the implications of these findings is given in section 5.1.

As shown in Figure 3.1.1 the MAX-DOAS instrument measures the path-integrated absorption of IO and OIO, the DSCDs. The units of these measurements are molec/cm^2. To convert the DSCD measurements into vertical concentration profiles, which allow the study of the spatial distribution of the iodine oxides, radiative transfer calculations are necessary. The retrieval algorithm and the results will be discussed in the following section.

4.5.3 Vertical Profiles of IO and OIO

The MAX-DOAS allows the retrieval of vertical concentration profiles for the iodine oxides. Vertical profiles provide important information on how locally constrained these species are and how they can impact areas further downwind. The following paragraphs outline the algorithm used to derive profiles of OIO and show examples of the results. We also briefly discuss why it was not possible to derive IO vertical profiles. The vertical profiles retrieval follows, in general, the methods used for nitrogen dioxide and formaldehyde profiles retrieval described by *Pikelnaya et al.* [2007].

In short, the retrieval of vertical trace gas profiles from MAX-DOAS observations is based on the fact that the absorption path length in the lower troposphere increases with decreasing elevation viewing angle [*Platt and Stutz*, 2008]. Because the light path is strongly influenced by molecular and aerosol scattering, it is necessary to perform radiative transfer modeling to accurately retrieve concentrations. The most commonly used approach, which is also adopted here, uses the oxygen collisional complex, O_4, which has a constant concentration profile in the atmosphere, to derive aerosol profiles, which are then used in the retrieval of the trace gas concentrations. The retrieval is thus a multi-stage process (Figure 4.5.2). This section gives a brief description of our approach, followed by the presentation of examples of vertical profiles. It

should be noted that the general idea of MAX-DOAS assumes that trace gases are distributed evenly in the horizontal. We will discuss below that this condition is not always met, in particular for IO.

A requirement for successful vertical profile retrieval is a separation of the differential slant column densities of O_4 and/or the respective trace gas, here IO and OIO. Figure 4.5.3 shows LP and MAX-DOAS OIO and O_4 measurements in Malibu for one week in October 2006. The MAX-DOAS O_4 and OIO DSCDs measured at different elevation viewing angles are clearly different in values during many time periods. However, the O_4 DSCD's are not as clearly different from each other, as one would expect for a clean (aerosol poor) air mass. Consequently, smaller differences between the OIO DSCDs from different elevation viewing angles observed in Malibu can be at least partially attributed to the radiative transfer conditions.

Retrieval Algorithm:

We used the following assumptions and observations to constrain the profile retrieval for aerosols, IO, and OIO. It is known that aerosol levels, whether in urban, rural or marine areas, are highest near the ground, due to dust, sea spray, or other particle creation mechanisms taking place there. During the day they are typically well mixed in the boundary layer. Their levels decrease with altitude above the boundary layer, often following an exponential decrease. Assuming this behavior to be valid for the marine environment, we parameterized the aerosol as follows: an extinction coefficient at ground level, kept constant up to the height of the marine boundary layer, and an exponential decay coefficient for the decrease above the marine boundary layer. Aerosol extinction was parameterized by a single scattering albedo of 0.982 and a phase-function based on *Henyey and Greenstein* [1941] with asymmetry coefficient of 0.69 [*Fiebig and Ogren*, 2006].

Radiative transfer calculations were performed using the TRACY II 3D Monte Carlo model [*Hendrick et al.*, 2006] for the aerosol extinction profiles for the measurement viewing geometry and different solar zenith angles (SZA)/solar azimuth angle (SAZ) combinations. The radiative transfer model calculates O_4 air mass factors (AMF) and box air mass factors (BAMF), i.e. the conversion coefficients from the observed DSCD to the vertical column density (VCD) in the entire atmosphere or certain height intervals, respectively.

Aerosol extinction profiles were generated based on four systematically varied parameters listed below; Figure 4.5.4 is a graphical example for one of these generated profiles:

1. Boundary layer height: H_{BL} [km]
2. Aerosol Extinction at the surface: Ext_{BL} [km^{-1}] (kept constant throughout the H_{BL})
3. Scale height of exponential decay of aerosol extinction above the boundary layer:

$$Ext(h) = Ext_{BL} \cdot e^{-\left(\frac{h-H}{ScaleH}\right)} \qquad \text{(E4.5.1)}$$

4. Tropospheric background aerosol extinction above the boundary layer: Ext_{Bckgr} [km^{-1}] (including non-marine aerosol, e.g. dust particles from the continent)

As the result of the radiative transfer calculations, a systematic database of O_4 AMF and DSCD for different aerosol profiles at different SZA/SAZ combinations was created. Using this data base, aerosol profiles at the time of a given measurement were retrieved by comparing the O_4 VCDs calculated for each elevation viewing angle with the measured O_4 DSCD divided by

the modeled O_4 AMF at the time of the measurement. Since, by definition, the VCD of O_4 is constant, and related to the variable SCD (or DSCD) by variable AMF, for the "correct" aerosol profile the resulting O_4 VCDs at all elevation viewing angles should be the same. In our retrieval we accepted all aerosol extinction profiles for which measured and modeled O_4 VCDs at all elevation viewing angles agreed within the errors. Example of such a retrieval is presented in Figure 4.5.5.

Using the derived aerosol profiles as input, AMFs and box AMFs for IO and OIO were calculated. A grid search method was used to retrieve profiles from these and the MAX-DOAS DSCD measurements. A number of vertical profiles were generated, parameterized, in analogy to aerosol test profiles, by the following four factors:

1. Boundary layer height: H_{BL} [km]
2. Trace gas mixing ratios at the surface (kept constant within the H_{BL}): C_X^{BL} [ppt]
3. Exponential decay of OIO above the boundary layer, governed by the scale height:

$$C_X = C_X^{BL} \cdot e^{-(\frac{h-H}{ScaleH})} \qquad \text{(E4.5.2)}$$

4. Inhomogeneous DSCD to account for the portion of the trace gas that is unevenly distributed within the marine boundary layer: IO/OIO Plume DSCD [molec cm^{-2}].

For the "true" profile, DSCDs calculated from the assumed concentration profile and box air mass factors should agree with the measured DSCDs. Just as with the aerosols, we accepted all vertical profiles for which calculated and measured DSCD agreed within their errors. Since the IO and OIO were located close to the ground, in good approximation the DSCD obtained from the measurement are equivalent to the SCD. Figure 4.5.2 provides a schematic of the trace gas vertical profile retrieval algorithm.

In the following section we will concentrate on the period from October 13 – 14 (Figure 4.5.6). Almost all day on October 13, and in the morning hours of October 14, OIO DSCDs clearly show an elevation viewing angle dependence expected for OIO evenly distributed in the lowest layers of the troposphere, despite the absence of a clear separation between the O_4 DSCDs from different elevations. This suggests that OIO in the MAX-DOAS line of sight not only must have been evenly distributed horizontally, but also exhibited a strong vertical gradient with the concentration rapidly decreasing with altitude. In the case of IO, only DSCDs from the 10° elevation are different in value from all other elevation viewing angles, which, as we will discuss later, makes the retrieval of profiles impossible (not shown).

The afternoon of October 13, 2006 will be used as an example of OIO vertical profile retrieval in Malibu, CA. During this time skies were clear allowing us to use the radiative transfer modeling to calculate OIO AMFs for that time period. In addition, MAX-DOAS OIO DSCDs showed a clear dependence on the elevation viewing angle (see Figure 4.5.6). O_4 DSCDs on October 13, 2006 show very little separation between the elevation viewing angles. The O_4 atmospheric vertical profile is known and shown in Figure 4.5.7, and this O_4 profile influences MAX DOAS DSCDs in a way that separation between the elevation viewing angles can be expected. Thus, the absence of separation between the O_4 DSCDs must be caused by aerosol loads, which reduced or eliminated differences in light paths. This means that a trace gas profile leading to separated trace gas DSCDs (like OIO DSCDs) in spite of perturbed or bunched-

together O_4 DSCDs must be located very close to the ground, where the geometric light path enhancement dominates in spite of some aerosol scattering. This point is illustrated in Figure 4.5.7, which shows an atmospheric O_4 vertical profile (solid black line) and proposed OIO vertical profile (solid blue line) that rapidly decreases with altitude. Red dashed lines represent light paths from 1° and 5° elevation viewing angles. Light from 1° elevation will pass through a larger amount of O_4 than the light from 5° elevation viewing angle, resulting in larger signal from the 1° path. Increased aerosol extinction will lead to smaller differences between the O_4 DSCDs from the two elevation viewing angles. However, the OIO vertical gradient is so strong, that, even at high aerosol extinction profile, the signal from the lower elevation viewing angle is still greater.

Figure 4.5.8 shows the results of the aerosol extinction profile retrievals for the time period between 18:00 and 19:00 UT in Malibu on October 13, 2006 (marked by the red rectangle on Figure 4.5.6). For all of the retrieved profiles, the aerosol extinction at the surface is equal to 0.055 km^{-1}, but boundary layer heights of the retrieved aerosol profiles vary between 50 and 1000 m. HYSPLIT backtrajectory calculations can constrain these values, as the HYSPLIT model estimated mixed layer heights of 930 m and 750 m for 18:00 and 19:00 UT respectively in Malibu. The large number of retrieved aerosol profiles and therefore ambiguity in the retrieval (for example boundary layer height) stems from the complicated radiative transfer conditions in Malibu on October 13.

Using all retrieved aerosol profiles, i.e. those that agree with the O_4 measurements (see description of the aerosol algorithm above), we can retrieve the OIO vertical profiles. Figure 4.5.9 depicts the statistical analysis representation for OIO vertical profiles retrieved for Malibu on October 13, 2006 for the time period between 18:10 UT (11:10 PST) and 19:00 UT (12:00 PST). The inset in the figure shows measured and calculated OIO DSCDs of nearly 1000 OIO vertical profiles that satisfied the retrieval criteria. MAX-DOAS-measured OIO DSCDs during this time period stayed approximately at the same values, and OIO profiles retrieved for all data points during this time period are very similar to each other as well; they show that the OIO profile in Malibu at that time consisted of an average of 8 (± 1) ppt of OIO at the ocean surface up to ~300 m, and that the mixing ratio rapidly decreased with altitude above 300 m. In addition to the OIO vertical profile, retrieval showed 1.34 (±0.87) × 10^{13} molec/cm^2 of OIO in inhomogeneous plumes.

Figure 4.5.6 also shows that October 13 is an unique and interesting day to examine because OIO DSCDs vary from higher values with clear separation between the elevation viewing angles in the morning to lower values with little difference between the elevation viewing angles in the afternoon (after 21:00 UT, 14:00 PST, see time period highlighted by the orange rectangle in Figure 4.5.6). Changes in the O_4 DSCDs during the day, on the other hand, are not as striking. The OIO vertical profile retrieval for the period after 21:00 UT indicates that the contribution of evenly distributed OIO in the marine boundary layer became much smaller, while the part of OIO in inhomogeneous plumes remained about the same as earlier in the day. Figure 4.5.10 shows an example of the OIO vertical profile retrieved for 22:03 UT. While OIO extent remained the same as earlier in the day, OIO mixing ratios decreased from the average value of 8 ppt at 18:30 UT to the average of 1.4 ppt at 22:03 UT. The error of the homogeneous OIO profile also increased, almost to the point that statistically it is not clear that a homogeneous OIO profile still existed in Malibu after 21:00 UT. OIO, however, was still present with 1.64 (± 0.37) × 10^{13} molec/cm^2 of OIO in the inhomogeneous plumes.

It is interesting to examine the possible reasons that could lead to the observed variations in MAX-DOAS OIO DSCD during this day, while the LP DOAS measurements did not show a significant change. On October 13, 2006, before and after 21:00 UT (14 PST) the wind speed was approximately the same, but the wind direction varied from ~ 130° before to ~210° after 21:00 UT. Wind from ~ 130° at Zuma Beach is associated with a direction along the coast line, approximately parallel to the MAX-DOAS line of sight. The 210° direction is associated with the open ocean air, traveling at an angle and crossing the MAX-DOAS line of sight. At the same time when the wind direction and the MAX-DOAS OIO DSCDs changes occurred, the LP-DOAS and in-situ NO_x measurements detected changes in the NO_2 levels: at 18:00 UT (11:00 PST) LP-DOAS measured 6.5 ppb of NO_2, at 22:00 UT (15:00 PST) however only 1 ppb of NO_2 was detected at Zuma Beach. This strongly indicates that corresponding changes in the concentrations and spatial distributions of OIO detected by the MAX-DOAS must have been associated with changes in meteorological conditions that resulted in different air masses prevalent in the first and second half of the day.

Our vertical retrievals of OIO profiles lead to the following picture of the spatial OIO distribution (see Figure 4.5.11): OIO was present in localized plumes, most likely associated with the emissions of I_2 (see below) along the DOAS light paths. In addition, a certain amount of OIO is also well mixed in the marine boundary layer. This OIO is most likely from iodine sources further upwind from Malibu. The presence of this “background” OIO is quite surprising since we are currently not able to explain its presence based on known iodine chemistry. However, it allows one to draw the conclusion that OIO is indeed transported over longer distances and can thus reach the LA basin. We therefore believe that iodine chemistry needs to be considered in the LA Basin.

We also applied our retrieval algorithm to observations of IO (Figure 4.5.12). However, we were only able to retrieve an inhomogeneous part, leading to the conclusion that the spatial distribution of IO in the marine boundary layer was too inhomogeneous to allow profile retrieval. This confirms previous reports that IO is predominantly located in localized plumes [*Saiz-Lopez and Plane*, 2004a]. Figure 4.5.13 gives a schematic view of the distribution of IO at Malibu. Localized plumes dominate the observations. The fact that the 10° MAX-DOAS light path shows lower values than the other elevations can be explained by its higher altitude at greater distances. The light path therefore runs above IO plumes that are furthest away from Zuma Beach.

4.6 Molecular halogens

Measurements of I_2 by Battelle’s APCI-MS/MS are reported only on days for which reliable blank measurements were available, which was during the period between October 20 and October 24, 2006. The ambient I_2 observations are shown in Figure 4.6.1. In general, measured I_2 mixing ratios varied between <0.5 ppt and 11 ppt, with an average of approximately 0.5 ppt. Note that no adjustments have been made for values that were measured below the I_2 LOD in the calculations or reported ranges. The highest I_2 levels were observed during periods of westerly and southwesterly winds, consistent with flow from over the ocean. The ambient I_2 measurement data are consistent with measurements reported in the literature, which have ranged from zero to greater than 50 ppt, for example at Mace Head [*Saiz-Lopez et al.*, 2006]. Br_2 was detected on most days, but far below the ~25 ppt LOD.

Figure 4.6.2 shows an overview of all molecular halogen observations and iodine oxides, including the data set acquired by E. Saltzman’s group at UCI (see *Finley* [2007] for more

details). Cl_2 mixing ratios reached up to 15 ppt during the first few days of the experiment and in the latter part of the experiment. Between October 12 and October 21, 2006, Cl_2 was typically below 1 ppt with a few episodes of mixing ratios up to 5 ppt. It is interesting to note that Cl_2 levels increased during the Santa Ana event when off-shore flow occurred. Cl_2 levels were also sometimes elevated during daytime, thus leading to an ongoing Cl atom production through Cl_2 photolysis.

Br_2 mixing ratios were typically below 1 ppt. During a few events Br_2 exceeded 1 ppt. Particularly interesting in this respect is the event on October 19 when a peak Br_2 mixing ratio of 12 ppt was observed by the UCI group. The source of this Br_2 is not clear. However, as we will show later, it is most likely emitted from the algae along the California coast. The absence of elevated Br_2 during most of the experiment is in agreement with the DOAS observation, which did not show any detectable BrO.

I_2 levels as observed by both mass-spectrometer instruments were also below 1 ppt for most of the field campaign. It should be noted here that I_2 is rapidly photolyzed during the day and we did not expect high I_2 during the day. However, the absence of I_2 during the night is somewhat surprising since this compound has been observed at high levels at other coastal locations. We believe that the absence of I_2 at night can be explained by the off-shore flows which would move any I_2 emitted by algae away from the coast. The fact that the LP-DOAS instrument did see IO is likely due to the location of the absorption path over the open ocean.

4.7 Aerosol

Figure 4.7.1 shows the measured aerosol size distribution from the APS instrument, a time series of sodium (Na) and chloride (Cl) concentrations from UNH's Hi-Vol PM sampling, and observational notes on particle morphology determined from SEM analysis of single particles collected by the TRAC. A clear oscillation in Na and Cl concentrations is evident and is in phase with sea breeze circulation. Na and Cl concentrations are highest in the daytime when winds bring ocean air and sea salt particles to the site. Diel concentrations of Na varied from approximately 0.1 to 1 ug/m^3 while Cl concentrations varied from approximately 0.2 to 2 ug/m^3 during the relatively clean marine air period experienced during the first half of the study. Other elements associated with sea-salt (i.e., I, Br, and Mg) also displayed clear diel variations as shown in Figure 4.7.2. Trace metals (Mn, Al, V) measurements are shown in Figure 4.7.3. These data clearly show that V, a tracer of fossil fuel combustion, was elevated during the LA Basin outflow period as expected but was also slightly elevated during the early portion of the study from October 7 – October 12, 2006. We attribute the peaks in V to ship plumes arriving at Malibu. During the Santa Ana event, very large increases in Al and Mn were observed and these metals remained elevated during the latter portion of the field experiment. The cleanest marine air periods, identified by the very low abundances of the crustal elements Al and Mn and by low V was observed during the period of October 14 to October 17, 2006.

SEM imaging of the single particles revealed sea-salt particles in every sample examined, which was expected given the close proximity to the shore. Figure 4.7.4 shows an image of a sample collected on October 9, 2006 when V was slightly elevated showing both fresh sea-salt particles and organic particles. Organic particles are revealed by the SEM as darker grey objects in the image. Processed sea-salt particles were observed both in the early part of the experiment as sodium sulfate, shown in Figure 4.7.5, and in the LA Basin outflow period as both sodium sulfate and sodium nitrate particles. Figure 4.7.6 shows fresh and chemically processed sea-salt

particles and soot particles, identified by their filamentous shape, from a sample collected during the Santa Ana period. What is notable about the Santa Ana period were high levels of Al and Mn as shown in Figure 4.7.3.

5 Discussion

5.1 Dependence of halogen levels on environmental parameters

It is instructive to examine how the observed halogen levels depend on environmental parameters such as tide, wind direction, and solar radiation. We will first concentrate on the molecular halogens observed by the two mass-spectrometry instruments. Elevated Cl_2, Br_2, and I_2 mixing ratios were predominantly observed with winds from the southwest [*Finley*, 2007], i.e. from the ocean and/or the coast near Malibu (Figure 5.1.1). It should be noted that Cl_2 and I_2, and to a lesser extent Br_2, have short photolytic lifetimes in the atmosphere. The detection of I_2 and Br_2 during the day implies sources of these species close to the Zuma Beach site.

The iodine oxide observations, which are less influenced by photolytic decay, provide a different view of the halogen sources. Figure 5.1.2 illustrates LP DOAS measured IO and OIO mixing ratios during the day as a function of the wind direction at the time of the measurement. Since LP DOAS measures trace gas concentrations averaged over the light path, the center of the wind-rose was placed at the center of the LP DOAS light path. High IO values were observed for winds originating from the South-Eastern to North-Western directions (top left of Figure 5.1.2, between 150 and 285 degrees). Figure 5.1.2 also shows IO/O_4 differential slant column density ratios (top right) measured by the 1° elevation viewing angle of MAX-DOAS instrument at Zuma Beach. The division of IO DSCDs by the O_4 DSCDs reduces the effect of radiative transfer, thus giving a much more accurate picture of the wind direction dependence. Similar to the LP DOAS IO distribution, high IO signal was observed with wind coming from the coast west of Zuma Beach. This result is similar to that observed for the molecular halogens. High IO levels for winds from the coast can be explained by sources between the beach and the light path, which passed over the ocean. These observations, together with our arguments in Section 4.5 support the conclusion that iodine sources are of coastal origin, as opposed to oceanic or land-based.

An interesting finding of our Malibu observations was that a part of the observed OIO appears to be well mixed in the marine boundary layer. A well mixed trace gas in the marine boundary layer can be an indication of non-local or area sources as well as sources sufficiently upwind to allow vertical mixing. Since we already concluded that the OIO precursor IO originates from local heterogeneous sources, we expect that OIO originates from iodine sources farther downwind from Zuma Beach. Please note that it is currently unclear how OIO can remain in the atmosphere long enough to be well mixed. Figure 5.1.2 (bottom left) shows LP and MAX DOAS OIO observations as a function of the wind direction. The much weaker dependence of OIO on wind direction (relative to that of IO) supports our conclusion that OIO is much better mixed within the marine boundary layer. A conclusion from this behavior is that OIO can be transported much further than IO and that this species or a possible non-IO OIO precursor may be the reservoir for transporting reactive iodine into the Los Angeles Basin.

During a number of occasions, the DOAS instruments also detected elevated levels of IO in air masses from the direction of the open ocean or the islands along the California coast. We investigated the question whether an open ocean source of halogens can be inferred from our

observations of iodine oxides. On October 11, 2006, starting at approximately 17:00 UT (10:00 PST), the weather station at the Zuma Beach site measured wind coming from the open ocean and the Channel Islands (between 260 and 280 degrees, see also Figure 5.1.3) as well as the direction along the continental coastline to the west of Zuma Beach (between 280 and 290 degrees) (see time period highlighted by the red rectangle on Figure 4.5.12). During this day, IO DSCDs from the 10° elevation viewing angle are much smaller than from the lower angles; and between 19:00 and 21:00 UT even some separation between all lower elevation angles could be observed. On October 12, between 14:00 UT and 18:00 UT (7:00 and 11:00 PST), the meteorological station at Zuma Beach measured wind coming from the direction of Catalina Island, and between 20:00 and 23:00 UT (13:00 and 16:00 PST) from the Channel Islands. During both periods, IO again shows a clear separation of the 10 degree DSCDs from those of the lower elevations. A separation of the DSCDs at different elevation viewing angles is an indication of a trace gas that is relatively evenly distributed, i.e. in our case IO would be well mixed in the marine boundary layer, as one would expect from a more distant source or an area source. Analysis of the Southern California Basin meteorological information for October 11 and 12, 2006 revealed unique conditions. During this time, a large cyclone was active off the coast, disturbing the "normal" diurnal circulation of the LA basin. The east coast of the LA basin, as well as Catalina Island and the Channel Islands experienced easterly winds. However, the west side of the LA basin (based on meteorological data collected at UCLA by James Murakami), Malibu (based on Zuma Beach meteorological station records), and Ventura County (see Figure 5.1.4) were experiencing "normal" westerly winds (James Murakami, personal communication). A simplified diagram of the air patterns over the LA Basin on October 11, 2006 is presented in Figure 5.1.4. The black dashed line in Figure 5.1.4, ending at the Zuma Beach location, depicts an approximate 12-hour trajectory of air measured the afternoon of October 11. A similar pattern is also applicable to the morning of October 12, 2006. It becomes clear that air masses sampled by the UCLA DOAS instruments during these times had not originated from the open ocean or the Channel Islands. The observed separation between the MAX-DOAS IO DSCDs must be due to the coastal IO plumes being "short" in the vertical direction, and not extending high enough for 10 degree elevation viewing line to probe them (see below). For October 11, our profile retrieval algorithm was not able to produce horizontally homogeneous IO profile that would result in the measured IO DSCDs.

It has been shown in literature [*Carpenter et al.*, 1999] that at the coasts of Ireland and Brittany [*Peters et al.*, 2005] reactive iodine levels depend on the tidal cycle, i.e. high levels are only observed during low tide. Figure 5.1.5 therefore shows LP DOAS IO mixing ratios as a function of the tidal height at the time of the measurement. Red and blue points represent day- and night-time measured IO mixing ratios respectively. This figure clearly shows that, in Malibu, in contrast to other locations, no dependency of IO on tidal height was observed, and similar levels of IO were observed during periods of high and low tides during the day and night. It thus appears that sources of reactive iodine precursors are active at all times.

5.2 Coastal Sources of Halogens

In the previous section we argued that sources of halogens are active at the Southern California Coast. While one can argue that the main source of chlorine and bromine is heterogeneous reactions on sea salt aerosol, this is not the case for iodine species. As discussed below, we believe that in the case of bromine other non-chemical sources may also be significant.

The Southern California coastline is home to a large number of brown (*Macrocystis pyrifera*), red (*Coralline algae*), and green sea lettuce (*Ulva sp.*) species of macroalgae [*Abbott and Hollenberg*, 1976; Channel Islands National Marine Sanctuaries http://channelislands.noaa.gov/]. The *Macrocystis pyrifera*, commonly known as Giant or Iodine Kelp is a predominant macroalgae species at the Southern California coast [*Halpern and Cottenie*, 2007]. Giant kelp is the world's largest and fastest growing marine plant. It can grow as much as 50 to 60 cm (20 to 25 inches) per day. Giant Kelp grows in the rocky subtidal areas at depths of between 3 and 30 m (10 to 100 feet). It prefers cool water temperatures between 50° and 65° F; when nutrients are plentiful the giant kelp can reach lengths of up to 30.5 meters (100 feet). Gas filled floats keep the plant suspended, allowing the kelp blades near the ocean surface to capture light [http://channelislands.noaa.gov/]. Figure 5.2.1 shows the picture of Giant Kelp mixed with some red sea lettuce (*Coralline algae)* and Surf Grass (*Phyllospedix sp.*) found at the Zuma Beach at the time of measurements. Unfortunately, there are no data available for the *Macrocystis pyrifera* distribution between Zuma and El Matador beaches and beyond. However, in 2002, California State University's Monterey Bay Seafloor Mapping Lab conducted a survey of *Macrocystis* population in the Santa Monica Bay (from east of Point Dume to Point Fermin of Palos Verdes Peninsula) [*Leisten*, 2002]. According to the survey, Giant Kelp forests in the Santa Monica Bay declined by more than half during the 1990's compared to the beginning of the 20th century. Despite the decline of the number of plants, kelp beds were still present almost continuously along the Malibu coast between Santa Monica and Point Dume. Since the sea floor between the Zuma Beach and El Matador State Beach is similar, it is reasonable to assume that *Macrocystis pyrifera* communities are spread along that part of the Malibu Coast as well.

To confirm the significance of molecular halogen emissions from coastal kelp (see, for example, *McFiggins et al*. [2004]), we performed a semi-quantitative experiment during CalHal using the API-365 APCI-MS/MS. Kelp was harvested from the ocean and placed in a clean Teflon bag (Figure 5.2.2). The bag was filled with zero air at ~12 L/min, while the API-365 sampled from the bag at ~8 L/min. The bag was sealed to inflate it and then vented to the atmosphere. A maximum of >150 ppt I_2 was observed immediately upon adding kelp to the Teflon bag (Figure 5.2.3); the steady-state I_2 concentration was ~20 ppt. An increase in I_2 was observed when the kelp was "perturbed" by rustling it around in the Teflon bag.

Molecular bromine was also detected during the experiment, and levels appeared to increase over the bag background when kelp was added to the bag (Figure 5.2.3). To our knowledge, this is the first report of Br_2 emissions from kelp and/or macroalgae, an observation that warrants further investigation.

A VOC sample was also collected from the bag and analyzed on site by GC-MS. Compounds identified in the bag sample in order of decreasing abundance were: dimethylsulfide (62 ppb), bromoform (60 ppb), dimethyldisulfide (25 ppb), chloroform (20 ppb) and iodoform (19 ppb). Lesser amounts of carbon disulfide (1.5 ppb), iodomethane (0.8 ppb), and iodoethane (0.4 ppb) were also observed.

5.3 Evidence for Chlorine Chemistry at the Southern California Coast

Evidence for Cl atom chemistry occurrence is implied by two observations 1) measurement of Cl_2 at mixing ratios up to 21 ppt and 2) measurement of chloroacetone mixing ratios up to 20 ppt. The highest mixing ratios of both species were measured early in the field study between October 9 and October 11, 2006. During this period average Cl_2 mixing ratios were 6.6 ± 3.7 ppt

compared to only 1 ± 0.9 ppt during the clean marine air period from October 13 to October 17, 2006. Chloroacetone was elevated during the early morning hours of October 9 with an average mixing ratio of 11 ± 3 ppt compared to levels typically below the detection limit of 4 ppt during the clean marine air period. The Cl_2 and chloroacetone data are shown in Figure 5.3.1 for the early portion of the field experiment, together with tracer data that are useful in characterizing the air masses. Monoterpene levels (m/z = 137) are also shown in the figure to identify transitions of sea-breeze circulation from a land breeze (elevated m/z = 137) to sea breeze (low m/z = 137). Sunrise and sunset times are identified by shading.

The air masses sampled during the October 9-11, 2006 period appear to be aged urban pollution. For example average particulate vanadium is elevated during this period compared to the middle portion of the study as shown in Fig 5.3.1. SEM images (not shown here) indicated that the particle population contained organic particles and chemically processed sea-salt, suggesting the impact of anthropogenic emissions. On October 9, there was a clear pollution period starting about midnight with elevated levels of CH_2Cl_2, aromatic compounds such as xylenes (m/z = 107), acetaldehyde (m/z = 45), and particulate vanadium. HYSPLIT back trajectories indicate northerly flow down the coast for October 9 and 10. At about 9:30 AM on October 9 there were high Cl_2 mixing ratios with 3 measurements > 12 ppt. Notable is that significant Cl_2 mixing ratios are measured during the day and night.

Another period of elevated Cl_2 mixing ratios occurred on October 11, 2006 from ~ 4 AM to 9 AM with Cl_2 mixing ratios > 12 ppt. The highest mixing ratio of 21 ppt occurred just before sunrise at 5:20 AM. Unfortunately there are no chloroacetone data for this event. HYSPLIT back trajectories indicate westerly flow, which would bring clean marine air on shore at this time. However, as discussed above in section 5.1, a high pressure system northwest of Malibu that may have caused air to re-circulate out of the LA Basin back into Malibu, a flow situation that may not be captured by HYSPLIT.

In general Cl_2 and chloroacetone were not well correlated. This may be anticipated given the very different lifetimes and source distributions of these species. It is interesting that Cl_2 and chloroacetone did not display a diel variability associated with sea-breeze circulation transitions or day/night photochemical activity transitions. The sea-breeze transitions are clear from the monoterpene signal at m/z = 137 measured by the PTR-MS. It is interesting that the onset of the October 9 pollution plume at about midnight is coincident with a sudden decrease in the monoterpene signal, supporting the argument of polluted marine air that has not been in recent contact with the land.

5.4 Impact of Halogens on Atmospheric Chemistry on the Southern California Coast and in Los Angeles Basin

The presence of molecular halogens and iodine oxides has implications for atmospheric chemistry on the California coast. To provide more insight into the impact of halogens on atmospheric composition we expanded UCLA's 1D chemical transport model with known halogen reactions.

UCLA's 1D model has been described in detail [*Geyer and Stutz*, 2004] and only a short description will be given here. The model is based on a highly resolved log-linear grid from the ground up to 3 km altitude. Its chemistry is based on the Regional Atmospheric Chemistry Mechanism (RACM) mechanism, and it includes uptake on aerosol and the ground of various species, including the nocturnal species NO_3 and N_2O_5. NO and hydrocarbons are emitted near

the surface at variable rates. In addition, biogenic emissions are included in the model. The model has been primarily used in the investigation of nocturnal chemistry and its impact on daytime ozone chemistry [*Geyer and Stutz*, 2004]. To provide insight into halogen chemistry, we expanded the model with the reactions listed in Table 5.1. Only a few reactions of chlorine with hydrocarbons were included, since the model, and in particular the RACM would have to be considerably expanded to provide a better description of the Cl + HC reaction, a task that was beyond the scope of this project. Biogenic emissions of Br_2 and I_2 were also added to the model.

For our analysis, we set up model runs in which an airmass was located over the nocturnal ocean for the first 10 hours of the model run with initial concentrations of 30 ppb of ozone and 2 ppb of NO_2. During this time no surface emissions of NO, CO, or hydrocarbons were allowed in the model. We included biogenic I_2 emissions to take into account the observations of nocturnal IO and OIO at Malibu. At hour 10, the airmass moved over the coast where it was exposed to elevated emissions of Br_2 and I_2 for a total of 4 hours, after which biogenic emissions of both species were set to zero. Sunrise was set to occur at hour 12. Urban emissions of NO, CO, and VOCs were started at hour 14 and continued throughout the end of the model run. Emission rates were taken from the annual emission inventories of Los Angeles County developed by the California Air Resources Board. The model timeline is an idealized setup for an airmass moving from the ocean over Malibu into the LA Basin. The model exercise was not intended to realistically model the atmospheric chemistry in Malibu or Los Angeles, but rather to give insights into our understanding of the halogen levels observed in Malibu and their possible impact on ozone downwind. We will compare our observations to more elaborate model calculations [*Knipping and Dabdub.*, 2003, *Cohan et al.*, 2008] in Section 6.2.

Table 5.1 Halogen reactions included in UCLA's 1D chemical transport model (rate constants and uptake coefficients from Atkinson, 2007 and Sander et al., 2006.

Reactions	Rate Constants
Chlorine Reactions	
$Cl_2 + HO \rightarrow HOCl + Cl$	3.6e-12*EXP(-1200/T)
$Cl + O_3 \rightarrow ClO + O_2$	2.8e-11*EXP(-250/T)
$Cl + HO_2 \rightarrow HCl$	3.4e-11
$Cl + HO_2 \rightarrow ClO + HO$	9.3e-12
$ClO + HO \rightarrow Cl + HO_2$	1.9e-11
$ClO + HO \rightarrow HCl$	1.2e-12
$ClO + HO_2 \rightarrow HOCl$	3.5e-12
$ClO + HO_2 \rightarrow HCl + O_3$	3.5e-12
$ClO + NO \rightarrow Cl + NO_2$	6.2e-12*EXP(295/T)
$ClO + NO_2 + M \rightarrow ClONO_2 + M$	K_o = 1.6*e-31; K_{oo} = 7.0*e-11; f = 0.4
$ClO + ClO \rightarrow Cl_2 + O_2$	1.0e-12*EXP(-1590/T)
$ClO + ClO \rightarrow Cl + ClOO$	3.0e-11*EXP(-2450/T)
$ClO + ClO \rightarrow Cl_2 + OClO$	3.5e-13*EXP(-1370/T)
$ClO + IO \rightarrow ICl$	2.4e-12
$ClO + IO \rightarrow Cl + I + O_2$	3.0e-12
$ClO + IO \rightarrow I + OClO$	6.6e-12
$Cl + H_2O_2 \rightarrow HCl + HO_2$	1.1e-11*EXP(-980/T)
$HCl + HO \rightarrow Cl + H_2O$	2.6e-12*EXP(-350/T)
$Cl + NO_2 + M \rightarrow ClNO_2 + M$	K_o = 1.8*e-31; K_{oo} = 1.0*e-10; f = 1.3
$Cl + HOCl \rightarrow Cl_2 + HO$	2.5e-12*EXP(-130/T)
$Cl + ClONO_2 \rightarrow Cl_2 + NO_3$	6.5e-12*EXP(135/T)
$OClO + NO \rightarrow ClO + NO_2$	1.1e-13*EXP(350/T)
$ClO + NO_3 \rightarrow ClOO + NO_2$	3.4e-13
$ClONO_2 \rightarrow ClO + NO_2$	1.2e-3
$HOCl + HO \rightarrow ClO + H2O$	5.0e-13
$ClONO_2 + HO \rightarrow HOCl + NO_3$	1.2e-12*EXP(-330/T)
$ClNO_2 + HO \rightarrow HOCl + NO_2$	2.4e-12*EXP(-1250/T)
$ClNO_2 + Cl \rightarrow Cl_2 + NO_2$	5.1e-12
$Cl + NO_3 \rightarrow ClO + NO_2$	2.4e-11
$HCl + NO_3 \rightarrow Cl + HNO_3$	5.0e-17
$Cl + CH_4 \rightarrow HCl + CH_3$	6.6e-12*EXP(-1240/T)
$Cl + C_2H_6 \rightarrow HCl + C_2H_5$	8.3e-10*EXP(-100/T)
Cl + C3-alkenes → HCl + radicals	2.05e-10
Bromine Reactions	
$Br + O_3 \rightarrow BrO + O_2$	1.7e-11*EXP(-800/T)
$Br + HO_2 \rightarrow HBr$	7.7e-12*EXP(-450/T)
$Br_2 + HO \rightarrow HOBr + Br$	2.0e-11*EXP(240/T)
$HBr + HO \rightarrow Br + H_2O$	6.7e-12*EXP(155/T)
$Br + NO_3 \rightarrow BrO + NO_2$	1.6e-11
$Br + NO_2 + M \rightarrow BrNO_2 + M$	K_o = 4.2*e-31; K_{oo} = 2.7*e-11; f = 0.55
$BrNO_2 \rightarrow Br + NO_2$	4.0e-14
$BrO + BrO \rightarrow Br + Br$	2.7e-12
$BrO + BrO \rightarrow Br_2 + O_2$	2.9e-14*EXP(840/T)
$BrO + NO \rightarrow Br + NO_2$	8.7e-12*EXP(260/T)
$BrO + HO_2 \rightarrow HOBr$	2.25e-12*EXP(500/T)
$BrO + HO_2 \rightarrow HBr + O_3$	2.25e-12*EXP(500/T)

Table 5.1 Continued	
$HBr + NO_3 \rightarrow HNO_3 + Br$	1e-16
$BrONO_2 \rightarrow BrO + NO_2$	1.3e-15
$BrONO_2 + HO \rightarrow HOBr + NO_3$	4.0e-13
$BrO + NO_2 + M \rightarrow BrONO_2 + M$	K_o = 4.7*e-31; K_{oo} = 1.8*e-11; f = 0.4
Iodine Reactions	
$I + O_3 \rightarrow IO + O_2$	2.1e-11*EXP(-830/T)
$I + HO_2 \rightarrow HI + O_2$	1.5e-11*EXP(-1090/T)
$HI + HO \rightarrow H_2O + I$	1.6e-11*EXP(440/T)
$I + NO_2 + M \rightarrow INO_2 + M$	K_o = 3.0*e-31; K_{oo} = 6.6*e-11; f = 0.63
$I_2 + HO \rightarrow HOI + I$	2.1e-10
$I_2 + NO_3 \rightarrow IONO_2 + I$	1.5e-12
$IO + HO_2 \rightarrow HOI$	1.4e-11*EXP(540/T)
$IO + NO \rightarrow I + NO_2$	7.15e-12*EXP(300/T)
$IO + NO_2 + M \rightarrow IONO_2 + M$	K_o = 7.7*e-31; K_{oo} = 1.6*e-11; f = 0.4
$IO + IO \rightarrow I + OIO$	5.4e-11*EXP(180/T)
$IO + IO \rightarrow I_2O_2$	7.5e-12*EXP(500/T)
$IONO_2 \rightarrow IO + NO_2$	2.9e-3
$IO + O_3 \rightarrow I + 2\ O_2$	1e-15
$IO + O_3 \rightarrow OIO + O_2$	2e-16
$IO + IO \rightarrow I + I + O_2$	1.8e-12*EXP(500/T)
$I + NO \rightarrow INO$	3.2e-13
$I + NO_2 \rightarrow INO_2$	5.1e-12
$OIO + NO \rightarrow IO + NO_2$	1.1e-12*EXP(542/T)
$INO_2 \rightarrow I + NO_2$	2.4
$INO_2 + INO_2 \rightarrow I_2 + 2NO_2$	2.9e-11*EXP(-2600/T)
$INO + INO \rightarrow I_2 + 2NO$	8.4e-11*EXP (-2620/T)
$I + NO_3 \rightarrow IO + NO_2$	4.5e-10
$I_2O_2 \rightarrow IO + IO$	31
$I + INO \rightarrow I_2 + NO$	2.6e-10
$I + INO_2 \rightarrow I_2 + NO_2$	8.3e-11
$I + IONO_2 \rightarrow I_2 + NO_3$	8.3E-11
$HOI + HO \rightarrow IO + H_2O$	2.0e-13
$IONO_2 + HO \rightarrow HOI + NO_3$	4.0e-13
Mixed Halogen Reactions	
$BrO + ClO \rightarrow Br + OClO$	1.6e-12*EXP(430/T)
$BrO + ClO \rightarrow Br + ClOO$	2.9e-12*EXP(220/T)
$BrO + ClO \rightarrow BrCl$	5.8e-13*EXP(170/T)
$Br_2 + Cl \rightarrow BrCl + Br$	1.2e-10
$Cl_2 + Br \rightarrow BrCl + Cl$	1.1e-15
Heterogeneous reactions	
N_2O_5 + sea salt aerosol $\rightarrow ClNO_2$	HOI + sea salt aerosol → IBr
N_2O_5 + sea salt aerosol $\rightarrow BrNO_2$	$ClONO_2$ + sea salt aerosol $\rightarrow Cl_2$
OH + sea salt aerosol $\rightarrow Cl_2$	$BrONO_2$ + sea salt aerosol $\rightarrow Br_2$
HOCl + sea salt aerosol $\rightarrow Cl_2$	$BrONO_2$ + sea salt aerosol → BrCl
HOBr + sea salt aerosol $\rightarrow Br_2$	$IONO_2$ + sea salt aerosol → ICl
HOBr + sea salt aerosol → BrCl	*$IONO_2$ + sea salt aerosol → IBr*
HOI + sea salt aerosol → ICl	

We performed three model runs as listed in Table 5.2. The base run simulated the air mass without halogen chemistry, i.e. halogen emissions and heterogeneous formation were turned off. As shown in Figure 5.4.1, the model starts with 30 ppb of ozone and 2 ppb of NO_2 at night, similar to the values observed at Malibu. Ozone and NO_2 levels slowly decrease during the night due to nocturnal NO_3 chemistry and deposition. At hour 14, when urban emissions were turned on, i.e. the airmass moved inland, NO_2 mixing ratios increased from ~0.5 ppb to ~5 ppb. At this time the boundary layer is already well mixed up to 1000 m. While vertical profiles of many gases, in particular short-lived gases emitted at the surface, were simulated in the model, we only show the calculated mixing ratios at 10 m altitude. The NO_2 levels remain around 5 ppb for the rest of the day. Ozone is slowly formed throughout the day, reaching a maximum at hour 23 of 73.5 ppb. This case thus constitutes a semi-polluted day in Los Angeles, with a relatively large inversion height of 1000 m. Approximately 50 ppb of ozone are formed throughout the day on top of the 30 ppb initially assumed in the model.

Table 5.2 List of model runs performed to study the impact of halogen chemistry

Model Run	Cl chemistry	Br chemistry	I_2 chemistry
Base	No	No	No
Hal_Cl	Yes	No	No
Hal_All	Yes	Yes	Yes

Our second model run, Hal_Cl, included all reactions in Table 5.1, excluding emissions of I_2 and Br_2 from coastal algae. The chlorine and iodine results of this model run are shown in Figures 5.4.2 and 5.4.3, respectively. At night Cl_2 and Cl atom concentrations are negligible. However, $ClNO_2$ is efficiently formed through the aerosol uptake of N_2O_5. $ClNO_2$ mixing ratios are over 150 ppt in the morning. The photolysis of $ClNO_2$ in the morning is the source of the Cl atom increase at hour 12. Cl_2 levels during this run were below 3ppt throughout the entire model run, and thus lower than the observations. Cl atom concentrations were around 1 to 3×10^4 cm^{-3} with the higher levels in the morning. The main source of Cl atoms is the photolysis of $ClNO_2$ and Cl_2. Ozone levels increased by ~4.5% (or 2.4 ppb) around hour 16 compared to the base run (Figure 5.4.1). The maximum ozone at hour 24 was increased by ~3% (2.2 ppb). The increase is caused by the additional oxidation of alkenes (Cl oxidation of other hydrocarbons was not included in these runs), which, similar to OH, initiated a radical reaction chain. As a consequence of the additional radical chain initiation, OH radicals increased from the base case concentration of 8×10^6 cm^{-3} by ~3% (Figure 5.4.4).

In our third run, Hal_All, we included oceanic and coastal emissions of I_2 and Br_2. Since we used small Br_2 emissions, reactive bromine levels remained low in the model and had little influence on the atmospheric chemistry. It should be noted, however, that the observation of elevated Br_2 implies that bromine chemistry may be more important than we assumed here. In this run, iodine levels increase slowly throughout the night (Figure 5.4.3) and then increase faster during the time the airmass was located at the coast. The very high levels directly at the coast are in agreement with our observation of unevenly distributed sources of I_2, which lead to unevenly distributed IO. Although not included in the figures, the model also shows very strong gradients

in I_2 and IO due to the very short photolytic lifetime of I_2 of ~10 sec, which contribute to the high coastal values.

Iodine levels were high for a short amount of time, when the airmass was directly impacted by the emissions before sunrise. During the next hour IO levels were in the range of 4 ppt similar to our observations. However, OIO levels were much smaller than observed. From these results, and also considering the fact that we cannot currently explain the presence of well-mixed OIO in the marine boundary layer, we conclude that unknown iodine and chlorine chemistry must be active in the marine boundary layer.

Ozone mixing ratios for the coastal region in the Hal_All run decreased compared to the base run due to the high iodine levels which lead to an effective O_3 destruction by the IO + IO and IO + HO_2 reaction cycles (see Figure 5.4.1). The morning ozone destruction is most likely overestimated in our model due to the challenge of modeling large inhomogeneous emissions of I_2.

Iodine and chlorine chemistry are closely linked through a number of homogeneous and heterogeneous reactions (see Table 5.1). The presence of reactive iodine increases Cl_2 mixing ratios to 10 – 20 ppt in the coastal region (Figure 5.4.2). The influence later during the day is more moderate. The largest change is, however, found in the Cl atom concentrations, which are three times larger upon the inclusion of iodine chemistry (Figure 5.4.2). This increase occurs in the presence of urban pollution and IO levels lower than those observed in Malibu. While we cannot be certain that 1 ppt of IO is indeed present in the LA basin, due to possible unidentified iodine reactions, the observation of direct coastal emissions and elevated reactive iodine levels in airmasses upwind of the basin implies that this is indeed possible. The reactions responsible for the increase in Cl atom concentration are heterogeneous reactions of HOI and $IONO_2$ on the sea-salt aerosol, which result in release of ICl. The increase in Cl atom concentrations during the day leads to an increase in ozone formation. Ozone mixing ratios increase by 8% (4.5 ppb) around hour 16 and the maximum ozone is higher by 4% (3.5 ppb) at this time. The OH radical concentration increased to 9×10^6 cm^{-3} in the Hal_Cl case, and is nearly 10% higher than in the base case (Figure 5.4.4). The daytime Cl/OH ratio was found to be ~0.007. At this ratio 60% of the oxidation of ethane proceeded through Cl oxidation in the model (Table 5.1). It should be noted that this value changes if other hydrocarbons are included in the model. The modeled Cl/OH ratio is close to the ratio of equivalent RO_2 production of 0.012 for a natural gas hydrocarbon source profile we described in Table 2.2. For the roadway hydrocarbon source profile, Cl chemistry contributes a significant 10% to the RO_2 formation.

The change of OH levels due to the presence of halogens not only impacts ozone formation but also the budget of NO_x and VOCs, as well as the formation of particles. The latter has thus far not been studied and more elaborate modeling efforts are needed to quantify this change. Both halogen cases also lead to a change in the NO/NO_2 ratio (Figure 5.4.4) in the urban atmosphere of up to -10%, which again impacts the budget of NO_x and the formation of particle nitrate.

Our model runs show that chlorine and iodine at the levels observed at Malibu can indeed have a significant impact on atmospheric chemistry. The increased oxidation capacity of the atmosphere due to elevated levels of chlorine atoms leads to more ozone and to an accelerated removal of hydrocarbons. Both chlorine and iodine also impact total radical levels and NO_x. An interesting result of our study is that the combined chlorine and iodine chemistry lead to much

higher Cl atom levels and increased ozone formation. One can thus conclude that the incorporation of chlorine into any model should always also include the chemistry of the other halogens. However, our model exercise identified several poorly known aspects of the chemistry of halogens. We cannot explain the formation of nocturnal Cl_2 or the presence of OIO at high NO_x levels. Also the biogenic emissions of Br_2 and I_2 are poorly characterized and not quantified. Our results should therefore be seen as more qualitative than quantitative. More research is needed to close the various gaps that remain in our understanding of atmospheric halogen chemistry.

6 Conclusions

Our study came to the following conclusion with respect to the original scientific questions (see Section 1).

6.1 Reactive Halogen Chemistry at the California Coast

The primary goal of this project was to provide experimental evidence for the presence of reactive halogens, reactive halogen precursors, and ongoing halogen chemistry, i.e. the presence of halogen reaction products. The results of our field experiment in Malibu, which was organized by UCLA and conducted by UCLA, WSU, Battelle, and NSF-sponsored collaborators from the UCI and the UNH, clearly showed that:

- Molecular chlorine levels of up to 12 ppt were observed on the southern California coast [*Finley*, 2007] during the day and the night.
- Bromine oxide mixing ratios were mostly below 1ppt. The observation of up to 10 ppt of Br_2, most likely emitted by coastal kelp, is quite surprising. There is no published record of biological Br_2 emission and this observation deserves further attention.
- Molecular iodine levels were below 1 ppt throughout the experiment. However, the fast photolysis of I_2 and the nocturnal off-shore winds would lead to low I_2 even in the presence of large emissions. The observation of several ppt of IO and even more OIO are proof that iodine chemistry is occurring on the southern Californian coast.
- Measurements of chloroacetone at Zuma Beach and in the LA basin provide further evidence of active chlorine chemistry. The observation of high chloroacetone at Zuma beach in air masses impacted by anthropogenic emissions (fresh or aged urban air) validates our approach of using chloroacetone as an indicator of active chlorine chemistry.
- Chloroacetone was observed in the canister samples taken in the Los Angeles Basin and during the outflow event in the second half of the experiment. During this Santa Ana event, elevated Cl_2 levels were also seen. This seems to indicate that chlorine chemistry is occurring in the LA basin.
- The single particle composition analysis shows the presence of processed sea salt aerosol at Malibu. We can thus conclude that sea salt aerosol is most likely one of the sources of reactive chlorine.

In summary, our 2006 experiment clearly shows the presence of reactive halogen species and their precursors. The chemistry of these compounds is clearly active at the coast and in the LA basin.

6.2 Impact on Ozone Formation in the Los Angeles Air Basin

To study the impact of halogen chemistry at and downwind of Malibu, we expanded UCLA's 1D chemical transport model with known halogen chemistry. While the model yielded halogen levels close to those observed, a number of obvious deficiencies, such as the inability to form Cl_2 at night and to maintain elevated OIO levels for high NO_x environments, make the model runs more qualitative than quantitative. In addition, the model did not include multiphase (i.e., aqueous aerosol) chemistry, limiting its ability to accurately simulate the heterogeneous release and recycling of the various halogen species. Nevertheless, the model identified a number of general features of the impact of halogen chemistry in polluted coastal areas. These results allow for a better understanding of the halogen chemistry in polluted areas and we can draw conclusions on the extent to which this chemistry needs to be considered and which key reactive species it influences.

A more quantitative answer to the impact of halogen chemistry can be gained by a comparison with the two published studies [*Knipping and Dabdub.*, 2003; *Cohan et al*., 2008] on the impact of chlorine chemistry on Southern California ozone. *Knipping and Dabdub* [2003] found up to 12 ppt Cl_2 in the "Cl chem" case of their study, which assumes the reaction of OH radicals on sea salt aerosol as the source of Cl_2, i.e. $OH_{(gas)} + Cl^-_{(aerosol)} \rightarrow ½\ Cl_{2(gas)} + OH^-_{(aerosol)}$. Although it is not clear where the 12 ppt Cl_2 was found, model runs with other chlorine chemistry seem to indicate that the maximum Cl_2 levels were found in Malibu for their base case. We can therefore conclude that the model run including OH mediated formation of Cl_2 agrees fairly well with the values observed by the UCI group at Malibu. For this case, the model used by *Knipping and Dabdub* [2003] predicted an increase of ozone mixing ratios in the basin of up to 10 ppb. The largest increase was found in the morning along the coastal areas and further inland later in the day. The inclusion of a proposed surrogate nocturnal NO_3 + sea salt reaction led to Cl_2 values at the coast of Malibu of over 300 ppt, which were not observed during CalHal. In a follow-up study, the same group investigated the impact of chlorine chemistry on ozone levels and the weekend effect. Again, the presence of chlorine led to an increase of ozone in the basin by 6 ppb at the locations of surface air monitoring stations, such as Burbank, Pico Rivera and others. The impact on the weekend effect was small in the base chlorine case. Much larger changes in ozone and the weekend effect were found for cases with amplified chlorine formation. However, artificially increased Cl_2 formation, again, led to much higher Cl_2 levels in Malibu than we observed.

The following conclusions can be derived from our results and published modeling studies:

- The comparison between the modeling studies and our observations imply that chlorine and iodine chemistry can indeed lead to an increase of peak ozone levels in the range of 3-8% in coastal urban areas in California. The presence of halogens also increases OH concentrations by up to 10% and changes the NO/NO_2 ratio.
- Our observations do support the presence of an unknown nocturnal source of Cl_2. However, this source seems to be smaller than that adopted by *Knipping and Dabdub* [2003] and *Cohan et al*. [2008] in their enhanced chlorine cases.
- The observation of N_2O_5 and the resulting formation of $ClNO_2$, as predicted by our model, show that this reaction should be considered as an important source of reactive chlorine.

- Iodine chemistry is occurring at Malibu and in the LA Basin. Because chlorine and iodine chemistry are linked, the inclusion of iodine chemistry increases chlorine in our model and leads to enhanced formation of ozone away from the coastal zone. It should be noted that the models used by *Knipping and Dabdub* [2003] and *Cohan et al*. [2008] did not include iodine chemistry, and that the impact of halogens on ozone could thus be larger than simulated in their respective studies.
- We were unable to reproduce elevated OIO levels at high NO_x in our model. We can thus conclude that currently unknown iodine chemistry is occurring.

The comparisons of the observations with our model, as well as published modeling studies, show that the levels of halogens in Malibu are high enough to impact ozone levels upwind. However, the lack in our understanding of the chemistry forming Cl_2 at night and the missing iodine reactions make it difficult to give a clear quantitative assessment of the impact of halogen chemistry on ozone levels in the LA basin.

6.3 Sources of Halogen Species

We can identify a number of sources of halogen species that serve as precursors to reactive halogen atoms and/or halogen oxides. All our observations point to oceanic and/or coastal sources of halogen species. In the case of Br_2 and IO, we concluded that the sources were near Zuma Beach, i.e. in the coastal area. No clear statement can be made about the sources of chlorine. A surprising observation was that of OIO being vertically well-mixed, which indicates that sources further away from Malibu can also contribute to the observed iodine levels. Whether these sources are coastal or oceanic is unclear. We can distinguish two types of halogen sources: biological and chemical.

- Biological sources: We identified *Macrocystis pyrifera*, commonly known as Giant or Iodine Kelp, which is the predominant macroalgae species at the Southern California coast, as the dominant source of iodine species. This result is based on a bag experiment, which clearly identified I_2 as being emitted by the kelp, and the observation of IO being inhomogeneously distributed, which indicates localized coastal sources. The surprising observation of ambient Br_2 and of Br_2 in the bag experiment showed that this species is also emitted by the kelp.

  Kelp is present along the entire California coast, including the various nearby islands. The emission of iodine and bromine is thus most likely a common occurrence and our Malibu observations can probably be assumed to be similar to other coastal locations. Although we have identified kelp as an important source of iodine and most likely bromine, we cannot estimate the total amount of halogens that are emitted from this source along the California coast. It seems prudent to quantify these emissions more accurately since they will impact the atmospheric chemistry in coastal California.
- Chemical sources: Our observations of Cl_2 and processed sea salt aerosol show that chlorine is released chemically from the aerosol on the coast. While we cannot determine the mechanism for Cl_2 release, it is clear from the observations that this mechanism seems to be active during the day and the night. The observations also seem to indicate that the release of Cl_2 is enhanced in aged polluted airmasses. More studies of the mechanism of Cl_2 formation in the laboratory and longer atmospheric observations should be performed to identify the responsible mechanisms of Cl_2 formation.

Our observations of high levels of N_2O_5 together with recent reports of $ClNO_2$ formation [*Osthoff et al.*, 2008] show that this mechanism is a significant source of the reactive chlorine precursor $ClNO_2$. In our model studies, up to 200 ppt of $ClNO_2$ were formed and release a comparable amount of chlorine atoms in the first few hours of the day.

In summary, our study clearly showed the presence of reactive halogen chemistry at the Southern California Coast. Both chlorine and iodine chemistry are clearly active. Whether bromine chemistry is important is unclear since the observation of Br_2 emissions from kelp is too limited to allow any quantitative statement.

7 References

Abbott I.A. and G.J. Hollenberg (1976), Marine Algae of California, *Stanford University Press, California*.

Alicke, B., et al. (1999), Iodine oxide in the marine boundary layer, *Nature*, *397*, 572-573.

Aliwell, S. R., M. Van Roozendael, P. V. Johnston, A. Richter, T. Wagner, D. W. Arlander, J. P. Burrows, D. J. Fish, R. L. Jones, K. K. Tornkvist, J. C. Lambert, K. Pfeilsticker, and I. Pundt (2002), Analysis for BrO in zenith-sky spectra: An intercomparison exercise for analysis improvement, *J Geophys Res*, 107 (D14), doi: 10.1029/2001JD000329.

Allan, B. J., et al. (2000), Observations of iodine monoxide in the remote marine boundary layer, *J Geophys Res*, 105, 14363-14369.

Anderson, R.S, L. Huang, R. Iannone and J Rudolph, (2007) Laboratory measurements of the $^{12}C/^{13}C$ kinetic isotope effects in the gas-phase reactions of unsaturated hydrocarbons with Cl atoms at 298±3 K. *J. Atmos. Chem*., 56, 275-291, 2007.

Appel, B. R., Tokiwa Y., Povard V. (1988), Southern California Air Quality Study - Fall Study, *Final Report, California Air Resources Board*, Berkeley, CA.

Ariya, P.A., A. Khalizov, A. Gidas, (2002) Reactions of gaseous mercury with atomic and molecular halogens: Kinetics, products studies, and atmospheric implications, *J. Phys. Chem.*, 106, 7310-7320.

Ariya, P.A., Dastoor A. P., Amyot M., Schroeder W.H., Barrie L., Anlauf K., Raofie F., Ryzhkov, A., Davignon D., Lalonde J., Steffen A. (2004), The Arctic: a sink for mercury, *Tellus*, 56B, 397-403.

Atkinson, R., and S.M. Aschmann, (1985) Kinetics of the gas phase reaction of Cl atoms with a series of organics at 296 K and atmospheric pressure, *Int. J. Chem. Kinetics*, 17, 33-41.

Atkinson, R., (1987), A structure activity relationship for the estimation of rate constants for the gas-phase reactions of OH radicals with organic compounds, *Int. J. Chem. Kinetics*, 19, 799-828.

Atkinson, R., et al. (2007), Evaluated kinetic and photochemical data for atmospheric chemistry, Volume VIII – gas phase reactions of inorganic halogens, *Atmos. Chem. Phys.*, *7*, 981-1191.

Barrie, L. A., et al. (1988), Ozone destruction and photochemical reactions at polar sunrise in the lower Arctic atmosphere, *Nature*, *334*, 138-141.

Behnke, W., et al. (1991), Formation of atomic Cl from sea spray via photolysis of nitryl chloride - Determination of the sticking coefficient of N_2O_5 on NaCl aerosol, *J Aerosol Sci*, *22*, S609-S612.

Behnke, W., et al. (1992), Formation of $ClNO_2$ and HONO in the presence of NO_2, O_3 and wet NaCl aerosol, *J Aerosol Sci*, *23*, 933-936.

Behnke, W., et al. (1997), Production and decay of $ClNO_2$ from the reaction of gaseous N_2O_5 with NaCl solution: Bulk and aerosol experiments, *J. Geophys. Res.*, *102*, 3795 - 3804.

Bloss, W. J., et al. (2005), Impact of halogen monoxide chemistry upon boundary layer OH and HO_2 concentrations at a coastal site, *Geophys. Res. Lett.*, *32*, doi:10.1029/2004GL022084.

Brauers T., Hausmann M., Brandenburger U., and H-P Dorn (1995), Improvement of differential optical absorption spectroscopy with a multichannel scanning technique, *Appl. Opt.*, 34 (21), 4472-4479.

Burkholder, J.B., M.K. Gilles, T. Gierczak, and A.R. Ravishankara (2002), The atmospheric degradation of 1-bromopropane ($CH_3CH_2CH_2Br$): The photochemistry of bromoacetone, *Geophys. Res. Lett.*, 29, 1822

Carpenter L. J., Sturges W.T., Penkett S.A., Liss P.S., Alicke B., Hebersreit K., Platt U. (1999), Observation of short-lived alkyl iodides and bromides at Mace Head, Ireland: links to biogenic sources and halogen oxide production, *J. Geophys. Res.* 104, 1679-1690.

Carpenter L. J., et al. (2000), Novel biogenic iodine-containing trihalomethanes and other short-lived halocarbons in the coastal East Atlantic, *Glob. Biogeochem. Cyc.*, *14*, 1191-1204.

Carpenter L. J., et al. (2001), Coastal zone production of IO precursors: A 2-dimensional study, *Atmos. Chem. Phys.*, *1*, 9-18.

Carpenter L. J., et al. (2003), Marine organohalogens in the atmosphere over the Atlantic and Southern Oceans, *J. Geophys. Res.*, *108*, doi:10.1029/2002JD002769.

Carr S., et al., (2003) A kinetic and mechanistic study of the gas phase reactions of OH radicals and Cl atoms with some halogenated acetones and their atmospheric implications., Phys. Chem. Cjem. Phys., 5, 3874-3833.

Calvert, J.G., R. Atkinson, J.A. Kerr, S. Mandronich, G.K. Moortgat, T.J. Wallington, G. Yarwood, (2000) The Mechanisms of Atmospheric Oxidation of the Alkenes, Oxford University Press, New York.

Calvert, J.G., R. Atkinson, K.H. Becker, R.A. Kamens, J.H. Seinfeld, T.J. Wallington, G. Yarwood, (2002) The Mechanisms of Atmospheric Oxidation of Aromatic Hydrocarbons, Oxford University Press, New York.

Calvert, J.G., R.G. Derwent, J. Orlando, G.S. Tyndall, T.J. Wallington, (2008), Mechanisms of Atmospheric Oxidation of the Alkanes, Oxford University Press, New York.

Cohan A., Chang W., Carreras-Sospedra M., and D. Dabdub (2008), Influence of sea-salt activated chlorine and surface-mediated renoxification on the weekend effect in the South Coast Air Basin of California, *Atmos. Environ.*, *42*(13), 3115-3129.

de Gouw, J., and C. Warneke (2007) Measurements of volatile organic compounds in the earth's atmosphere using proton-transfer-reaction mass spectrometry, *Mass Spectrometry Reviews*, 26, 223-257.

Fan, S.-M., and D. J. Jacob (1992), Surface ozone depletion in the Arctic spring sustained by bromine reactions on aerosols, *Nature*, *359*, 522-524.

Fiebig M., Orgen J.A. (2006), Retrieval and climatology of the aerosol asymmetry parameter in the NOAA aerosol monitoring network, *J. Geophys. Res.*, 111, D21204, doi:10.1029/2005JD006545.

Finlayson-Pitts, B. J., et al. (1983), Reaction of NO_2 with NaCl and atmospheric implications of NOCl formation, *Nature*, *306*, 676-677.

Finlayson-Pitts, B. J., et al. (1990), Ozone destruction and bromine photochemistry at ground level in the Arctic spring, *Nature*, *343*, 622-625.

Finlayson-Pitts, B. J. (1993), Chlorine Atoms as a potential tropospheric oxidant in the marine boundary layer, *Res. Chem Intermed.*, *19*, 235 - 249.

Finlayson-Pitts, B. J., and J. N. Pitts (2000), *Chemistry of the upper and lower atmosphere: theory, experiments and applications*, Academic Press, San Diego, CA; London.

Finlayson-Pitts, B. J. (2003), The tropospheric chemistry of sea salt: A molecular-level view of the chemistry of NaCl and NaBr, *Chem. Rev.*, *103*, 4801-4822.

Finley, B.D., (2007) Detection of dihalogens in coastal urban air, *PhD thesis University of California Irvine, Irvine*.

Fleischmann, O.C., Orphal, J., Burrows, J.P. (2004): New ultraviolet absorption crosssections of BrO at atmospheric temperatures measured by time-windowing Fourier transform spectroscopy. *J. Photochem. Photobiol. A Chem.* 168,117–132.

Foster, K. L., et al. (2001), The role of Br_2 and BrCl in surface ozone destruction at polar sunrise, *Science*, *291*, 471-474.

Gershenzon, M., et al. (1999), The mechanism of reactive NO_3 uptake on dry NaX (X=Cl, Br), *J Atmos Chem*, *34*, 119 - 135.

Geyer, A., and J. Stutz (2004), Vertical profiles of NO_3, N_2O_5, O_3, and NO_x in the nocturnal boundary layer: 2. Model studies on the altitude dependence of composition and chemistry (vol 109, art no D16399, 2004), *J Geophys Res*, *109*, doi:10.1029/2003JD004211.

Ghosal, S., et al. (2005a), Electron spectroscopy of aqueous solution interfaces reveals surface enhancement of halides, *Science*, *307*, 563-566.

Ghosal, S., et al. (2005b), In situ study of water-induced segregation of bromide in bromide-doped sodium chloride by scanning polarization force microscopy, *J Phys Chem A*, *109*, 4744-4749.

Greenblatt, G.D., Orlando J.J., Burkholder J.B., and A.R. Ravishankara (1990), Absorption measurements of Oxygen Between 330 and 1140 nm, *J. Geophys. Res.*, 95 (D11), 18577-18582.

Halpern, B.S. and Cottenie K. (2007), Little evidence for climate effects on local-scale structure and dynamics of California kelp forest communities, *Global Change Biology*, 13, 236-251, doi: 10.1111/j.1365-2486.2006.01243.x

Hebestreit, K., et al. (1999), First DOAS measurements of tropospheric bromine oxide in mid latitudes, *Science*, *283*, 55-57.

Hendrick, F., et al. (2006) Intercomparison exercise between different radiative transfer models used for the interpretation of ground-based zenith-sky and multi-axis DOAS observations. *Atmos. Chem. Phys.* 6, 93–108.

Henyey, L. C., and Greenstein J. L. (1941), Diffuse radiation in the galaxy, *Astrophysical Journal*, 93 (1), 70-83.

Hönninger, G. (1999), Referenzspektren reaktiver Halogenverbindungen für DOAS-Messungen, Diploma Thesis, *University of Heidelberg, Heidelberg*.

Hughes, L. S., et al. (2000), Evolution of atmospheric particles along trajectories crossing the Los Angeles basin, *Atmos. Env.*, *34*, 3058 - 3068.

Jobson, B.T., et al. (1994), Measurements of C_2-C_6 hydrocarbons during the Polar Sunrise 92 Experiment: Evidence for Cl-atom and Br-atom Chemistry, *J. Geophys. Res.*, 99, 2355-25368.

Jobson, B.T., et al (1998), Spatial and temporal variability of nonmethane hydrocarbon mixing ratios and their relation to photochemical lifetime, *J. Geophys. Res.*, 103, 13,557-13,567.

Jobson, B.T. et al (1999), Trace gas mixing ratio variability vs. lifetime in the troposphere and stratosphere – Observations, *J. Geophys. Res.*, 104, 16,091-16,113.

Jobson, B.T., et al (2004), Hydrocarbon source signatures in Houston Texas – Influence of the petrochemical industry, *J. Geophys. Res.*, 109, doi:10.1029/2004JD004887.

Keene, W. C., et al. (1990), The geochemical cycling of reactive chlorine through the marine troposphere, *Glob. Biogeochem. Cyc.*, *4*, 407-430.

Keene, W. C., J. Stutz, A. P. Pszenny, J. R. Maben, E. V. Fischer, A. M. Smith, R. von Glasow, S. Pechtl, B. C. Sive, and R. K. Varner (2007), Inorganic chlorine and bromine in coastal New England air during summer, *J Geophys Res*, *112*(D10), doi: 10.1029/2006JD007689.

Khalil, M. A. K., et al. (1981), Atmospheric methylchloride (CH_3Cl), *Chemosphere*, *10*, 1019-1023.

Knipping, E. M., and D. Dabdub (2002), Modeling Cl_2 formation from aqueous NaCl particles: Evidence for interfacial reactions and importance of Cl_2 decomposition in alkaline solution, *J Geophys Res*, *107*, doi:10.1029/2001JD000867.

Knipping, E. M., and D. Dabdub (2003), Impact of chlorine emissions from sea-salt aerosol on coastal urban ozone, *Environ Sci Technol*, *37*, 275-284.

Laskin, A., et al. (2003) Time-resolved aerosol collector for CCSEM/EDX single-particle analysis. *Aerosol Sci. Tech.*, 37, 246-260.

LeBras, G., and U. Platt (1995), A possible mechanism for combined chlorine and bromine catalysed destruction of tropospheric ozone in the Arctic, *Geophys. Res. Lett.*, *22*, 599-602.

Leisten T.M. (2002), Coastal watershed development, erosion, marine habitat loss and kelp forest decline in Santa Monica Bay, California, California State University Monterey Bay Seafloor Mapping Lab, May 2002, http://seafloor.csumb.edu/publications/SFML_Capstones/Leisten_capstone02.pdf

Leser, H., et al. (2003), MAX-DOAS measurements of BrO and NO_2 in the marine boundary layer, *Geophys. Res. Lett.*, *30*, 1,537.

McFiggans G., et al. (2004), Direct evidence for coastal iodine particles from Laminaria macroalgae – linkage to emissions of molecular iodine, ACP, No. 4, 701-713.

Meller R., Moorgat G.K. (2000), Temperature dependence of absorption cross sections of formaldehyde between 223 and 323 K in the wavelength range 225-375 nm, *J. Geosphys. Res.*, 105(D6), 7089-7101

Mozurkewich, M. (1995), Mechanisms for the release of halogens from sea-salt particles by free radical reactions, *J. Geophys. Res.*, *100*, 199-207.

Osthoff, H. D., et al. (2008), High levels of nitryl chloride in the polluted subtropical marine boundary layer, *Nature Geoscience*, *1*(5), 324-328.

Peters, C., S. Pechtl, J. Stutz, K. Hebestreit, G. Honninger, K. G. Heumann, A. Schwarz, J. Winterlik, and U. Platt (2005), Reactive and organic halogen species in three different European coastal environments, *Atmos. Chem. Phys.*, *5*, 3357-3375.

Pikelnaya O., Hurlock S.C., Trick S., and Stutz J. (2007), Intercomparison of Multi-Axis and Long-Path DOAS Measurements in the Marine Boundary Layer, *J. Geophys. Res.*, 112, D10S01, doi:10.1029/2006JD007727.

Platt, U., and J. Stutz (2008), *Differential Optical Absorption Spectroscopy: Principles and Applications*, , Springer, Heidelberg, New York, ISBN 978-3540211938.

Pszenny, A. A. P., et al. (1993), Evidence of inorganic chlorine gases other than hydrogen-chloride in marine surface air, *Geophys Res Lett*, *20*, 699-702.

Ragains, M.L., B.J. Finlayson-Pitts, (1997) Kinetics and mechanism of the reaction of Cl-atoms with 2-methyl-1-3-butadiene (isoprene) at 298 K, *J. Phys. Chem. A*., 101, 1509-1517.

Rasmussen, R. A., et al. (1982), Atmospheric methyl iodine (CH_3I), *J. Geophys. Res.*, *87*, 3086 - 3090.

Read, K. A., et al. (2008), Extensive halogen-mediated ozone destruction over the tropical Atlantic Ocean, *Nature*, *453*(7199), 1232-1235.

Rogozen, M. B., et al. (1988), *Sources and concentrations of chloroform emissions in the South Coast Air Basin*, Final Report, Air Resources Board, California.

Saiz-Lopez, A., and J. M. C. Plane (2004a), Novel iodine chemistry in the marine boundary layer, *Geophys Res Lett*, *31*, doi:10.1029/2003GL019215.

Saiz-Lopez, A., et al. (2004b), Bromine oxide in the mid-latitude marine boundary layer, *Geophys Res Lett*, *31*, doi:10.1029/2003GL018956

Saiz-Lopez A., et al. (2004c), Absolute absorption cross-section and photolysis rate of I_2. *Atmos. Chem. Phys*, 4, 2379-2403.

Saiz-Lopez, A., J. A. Shillito, H. Coe, and J. M. C. Plane (2006), Measurements and modelling of I_2, IO, OIO, BrO and NO_3 in the mid-latitude marine boundary layer, *Atmos. Chem. Phys.*, *6*, 1513-1528.

Saiz-Lopez, A., K. Chance, X. Liu, T.P. Kurosu, and S. P. Sander (2007a) First observations of iodine oxide from space, *Geophys. Res. Lett*., 34, L12812, doi:10.1029/2007GL030111

Saiz-Lopez, A., A. S. Mahajan, R. A. Salmon, S. J.-B. Bauguitte, A. E. Jones, H. K. Roscoe, and J. M. C. Plane (2007b), Boundary Layer Halogens in Coastal Antarctica, *Science*, *317*(5836), 348-351

Sander, R., and P. J. Crutzen (1996), Model study indicating halogen activation and ozone destruction in polluted air masses transported to the sea, *J. Geophys. Res.*, *101D*, 9121-9138.

Sander S.P., et al. (2006), Chemical Kinetics and Photochemical Data for Use in Atmospheric Studies Evaluation Number 15, *JPL Publication 06-2, NASA, JPL*, Pasadena, CA.

Shi J., Bernhard M.J. (1997), Kinetic studies of Cl-atom reactions with selected aromatic compounds using the photochemical reactor-FTIR, *International Journal of Chemical Kinetics*, Vol. 29, Issue 5, 349-358.

Sokolov O., et al., (1998), Kinetics and mechanism of the gas phase reaction of Cl atoms with benzene, *J. Phys. Chem. A*., 102, 10671-10681.

Spicer, C. W., et al. (1998), Unexpectedly high concentrations of molecular chlorine in coastal air, *Nature*, *394*, 353-356.

Spicer, C. W., et al. (2002), Molecular halogens before and during ozone depletion events in the Arctic at polar sunrise: concentrations and sources, *Atmos. Environ.*, *36*, 2721-2731.

Steffen A., et al. (2008), A synthesis of atmospheric mercury depletion event chemistry in the atmosphere and snow, Atmos. Chem. Phys., 8, 1445–1482.

Stutz J., Platt U. (1996), Numerical analysis and estimation of the statistical errors of differential optical absorption spectroscopy measurements with least-square methods, *Applied Optics*, Vol. 35, No 30, 6041-6053.

Stutz, J., and U. Platt (1997), Improving long-path differential optical absorption spectroscopy with a quartz-fiber mode mixer, *Appl. Opt.*, *36*, 1105-1115.

Stutz, J., et al. (1999), Chemistry of halogen oxides in the troposphere: Comparison of model calculations with recent field data, *J. Atmos. Chem.*, *34*, 65-85.

Stutz, J., et al. (2002), Atmospheric reactive chlorine and bromine at the Great Salt Lake, Utah, *Geophys Res Lett*, *29*, 1380.

Stutz, J., O. Pikelnaya, S. C. Hurlock, S. Trick, S. Pechtl and R. von Glasow (2007), Daytime OIO in the Gulf of Maine, *Geophys. Res. Lett.*, *34*, *L22816*, doi:10.1029/2007GL031332.

Su, T. (1988), Trajectory calculations of ion-polar molecule capture rate constants at low temperatures, *J. Chem. Phys*., 89, 5355,.

Tanaka, P. L., et al. (2000), Anthropogenic sources of chlorine and ozone formation in urban atmospheres, *Environ Sci Technol*, *34*, 4470-4473.

Tanaka, P. L., et al. (2003a), An environmental chamber investigation of chlorine-enhanced ozone formation in Houston, Texas, *J Geophys Res*, *108*, doi:10.1029/2002JD002432.

Tanaka, P. L., et al. (2003b), Direct evidence for chlorine-enhanced urban ozone formation in Houston, Texas, *Atmos. Environ.*, *37*, 1393-1400.

Tuckermann, M., et al. (1997), DOAS-observation of halogen radical-catalysed Arctic boundary layer ozone destruction during the ARCTOC-campaigns 1995 and 1996 in Ny-Ålesund, Spitsbergen, *Tellus*, *49B*, 533-555.

Tyndall G.S,, J.J. Orlando, T.J. Wallington, M. Dill, E.W. Fraser (1997), Kinetics and mechanisms of the reactions of chlorine atoms with ethane, propane, and n-butane, *Int. J. Chem. Kinetics*, 29, 43-55.

Tyndall G.S,, J.J. Orlando, E.C. Apel, D.D. Reimer, S.E. Paulson (2003), Rate coefficients and mechanisms of the reactions of Cl-atoms with a series of unsaturated hydrocarbons under atmospheric conditions, *Int. J. Chem. Kinetics*, 35, 334-353.

Vogt, R., et al. (1996), A mechanism for halogen release from sea-salt aerosol in the remote marine boundary layer, *Nature*, *383*, 327-330.

Voigt, S., J. Orphal, K. Bogumil, and J. P. Burrows (2001), The temperature dependence (203-293 K) of the absorption cross sections of O_3 in the 230-850 nm region measured by Fourier-transform spectroscopy, *J. Photochem and Photobiol. A*, 143, 1-9.

Voigt, S., J. Orphal, and J. P. Burrows (2002), The temperature and pressure dependence of the absorption cross-sections of NO_2 in the 250-800 nm region measured by Fourier-transform spectroscopy, *J Photochem Photobiol a*, 149, 1-7.

Volkamer R., Spietz R., Burrows J., Platt U. (2005), High-resolution absorption cross-section of glyoxal in the UV-visible and IR spectral range, *J. Photochem. Photobio. A* – Chemistry, 172, 35 – 46.

von Glasow, R., et al. (2004), Impact of reactive bromine chemistry in the troposphere, *Atmos. Chem. Phys.* 4, 2481-2497.

Vountas M., Rozanov V.V., Burrows J.P. (1998), Ring effect: impact of rotational raman scattering on radiative transfer in Earth's atmosphere, *J. Quant. Spectrosc. Radiat. Transfer*, Vol. 60, No. 6, 943-961.

Wallington, T.J., L.M. Skewers, W.O. Siegel. (1988), Kinetics of the gas phase reaction of chlorine atoms with a series of alkenes, alkynes, and aromatics at 295 k, *J. Photochem. Photobio. A. Chem.*, 45, 167-175.

Wang, L, J. Arey, R. Atkinson (2005), Reactions of chlorine atoms with a series of aromatic hydrocarbons, *Environ. Sci. Technol*, 39, 5302-5310.

Wayne, R. P., et al. (1995), Halogen oxides: radicals, sources and reservoirs in the laboratory and in the atmosphere, *Atm. Environ.*, *29*, 2675 - 2884.

Zetzsch, C., et al. (1988), Heterogeneous formation of chlorine atoms from NaCl in a photosmog system., *J. Aerosol Sci*, *19*, 1202 - 1206.

Zetsch, C., and W. Behnke (1992), Heterogeneous Photochemical sources of atomic Cl in the troposphere, *Ber. Bunsenges.*, *96*, 488-493.

Figures

Chapter 3

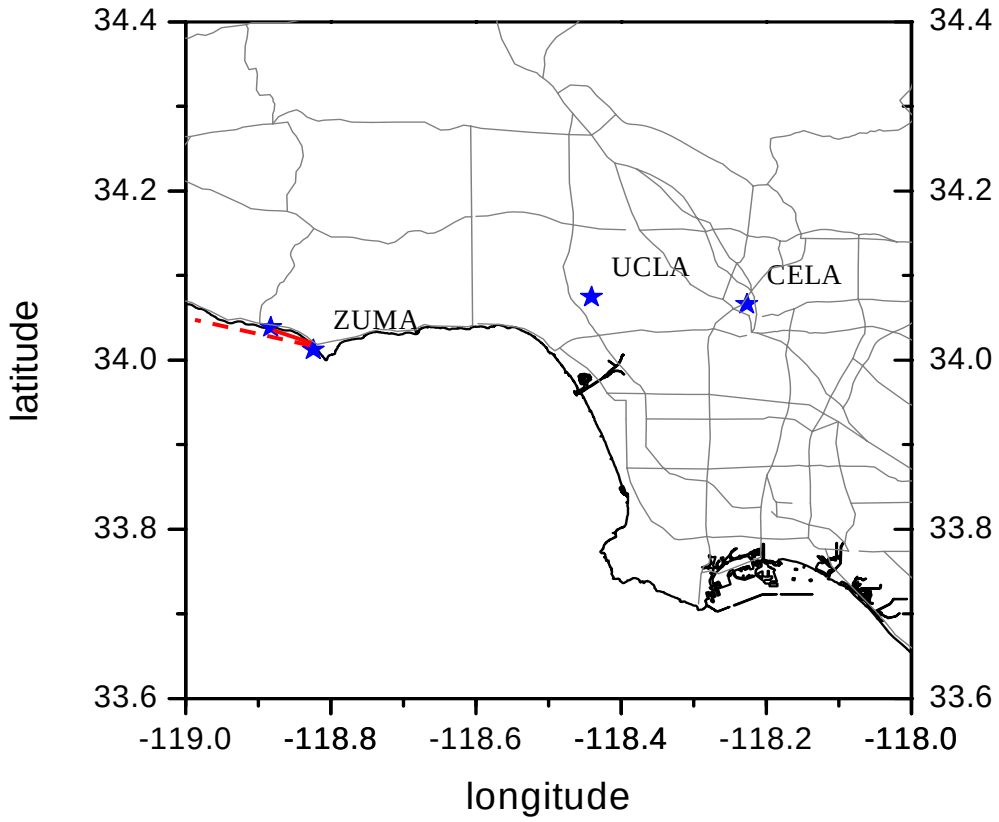

Figure 3.0.1. Map of field site locations for the Zuma Beach halogen experiment. The LP DOAS light path is indicated by the red line. Unmarked star at the west end of the LP DOAS light path indicates El Matador State Beach – location of the LP DOAS retro reflector array. The MAX-DOAS line of sight is shown by the red dashed line.

Figure 3.0.2. Photograph of mobile containers at the main site at Zuma Beach.

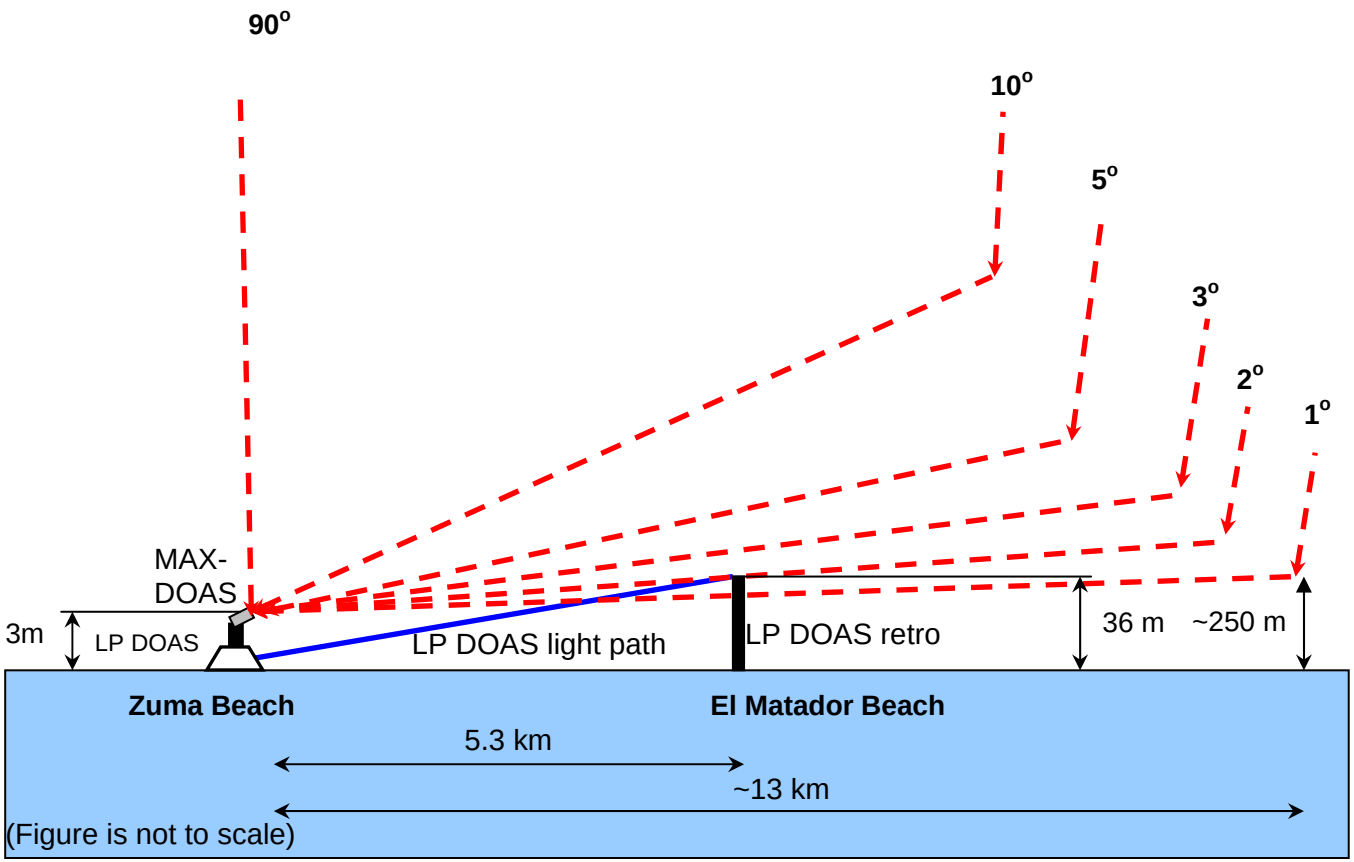

Figure 3.1.1. Schematics of the DOAS experimental set-up at Zuma Beach.

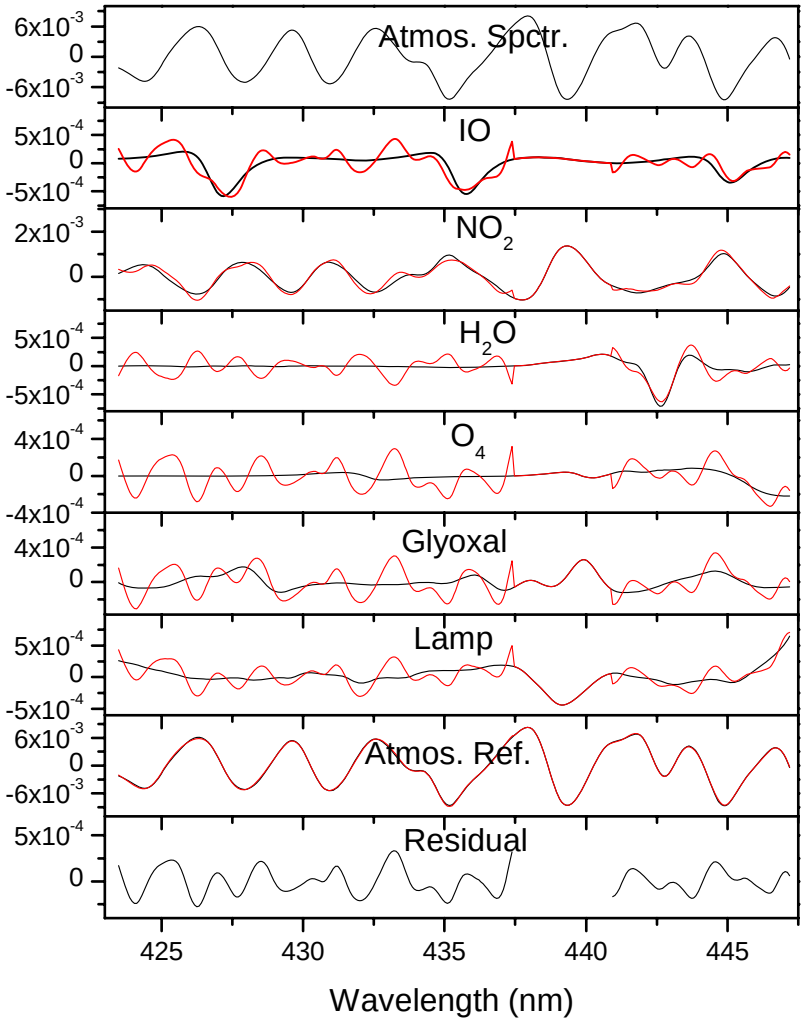

Figure 3.1.2. Example of the spectral analysis of daytime IO from the LP DOAS spectrum recorded on 10/12/2006 at 16:14 UT. The red lines represent the spectral references. The black lines represent fit results, i.e. the fitted reference + the residual. From top to bottom of the figure the following references are shown: the atmospheric absorption spectrum, the IO, NO_2, H_2O, O_4, and Glyoxal absorptions, lamp spectrum, daytime atmospheric reference spectrum, and residual. The region from 437 to 441 nm was excluded from the analysis due to spectral interferences, most likely caused by the instrument. The absorption structure of IO was clearly identified in this spectrum. The IO mixing ratio was determined to be 2.0 +/- 0.3 ppt.

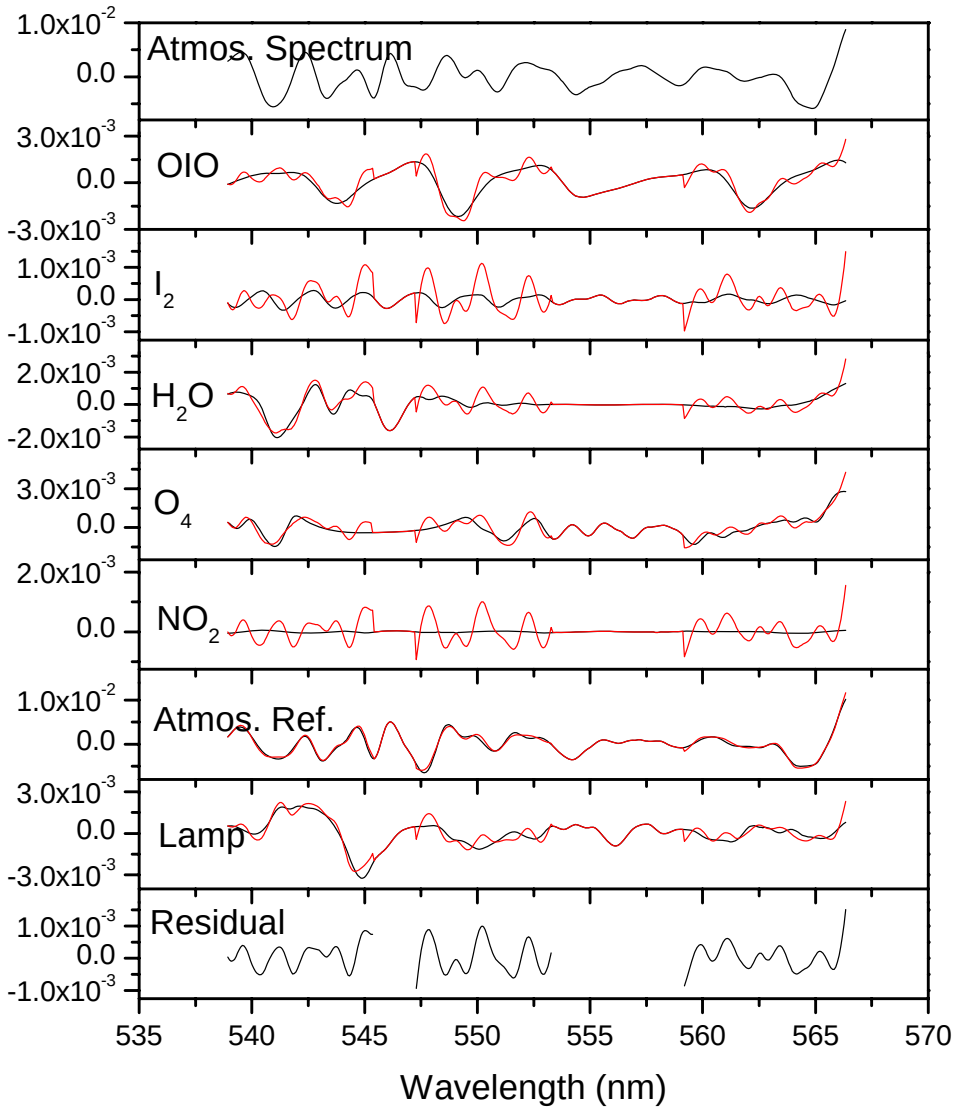

Figure 3.1.3. Example of the spectral analysis of daytime OIO from the LP DOAS spectrum recorded on 10/13/2006 at 13:06 UT. The black lines represent the spectral references. The red lines represent fit results, i.e. the fitted reference + the residual. From top to bottom of the figure the following references are shown: the atmospheric absorption spectrum, the OIO, I_2, H_2O, O_4, and NO_2 absorptions, atmospheric reference spectrum, lamp spectrum, and residual. The regions from 546 to 547.5 nm and 553 to 559 were excluded from the analysis due to spectral interferences, most likely caused by the instrument. The absorption structure of IO was clearly identified in this spectrum. The OIO mixing ratio was determined to be 23.5 ± 2.2 ppt.

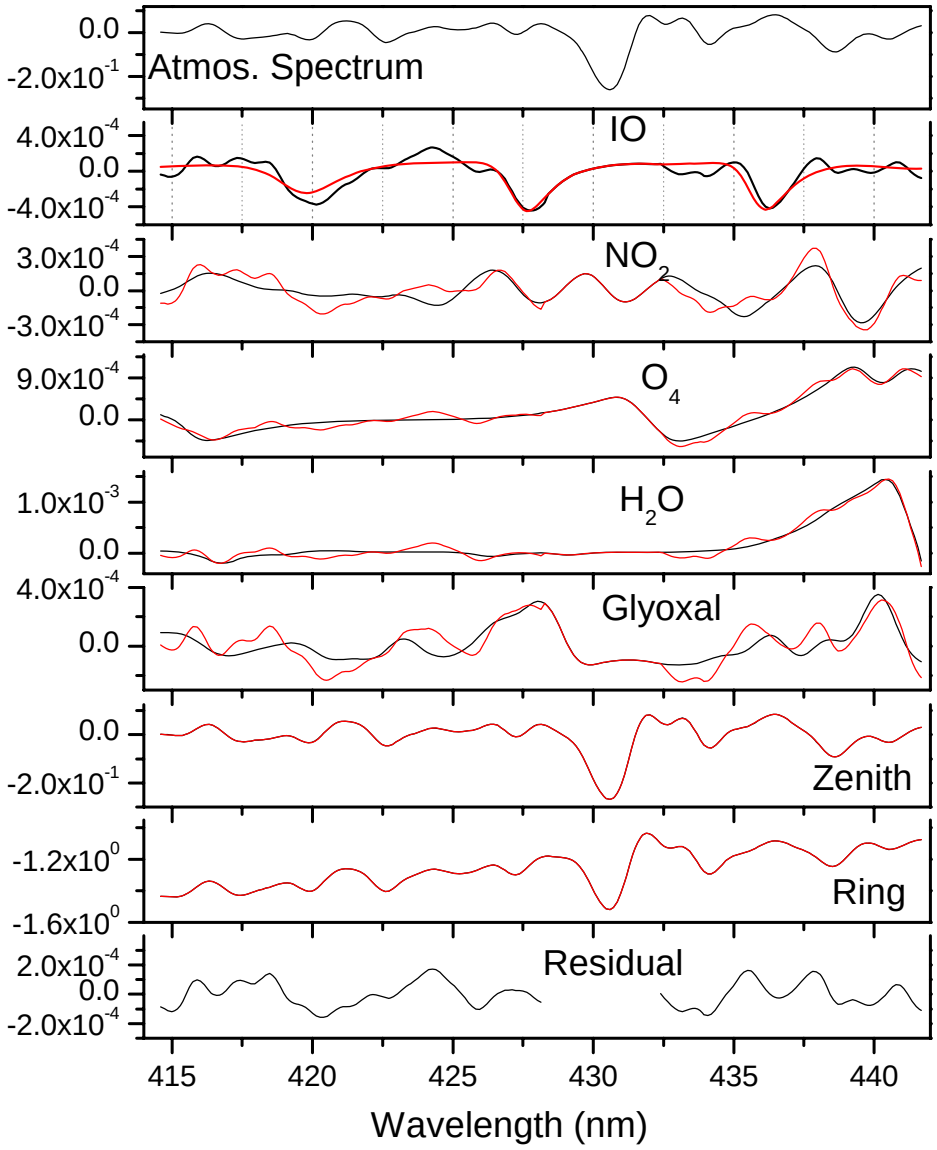

Figure 3.1.4. Example of the spectral analysis of daytime IO from the 1° elevation viewing angle MAX-DOAS spectrum recorded on 10/11/2006 at 19:26 UT. Red lines represent the spectral references. Black lines represent fit results, i.e. the fitted reference + the residual. The region from 428 to 432 nm was excluded from the analysis due to spectral interferences from either unknown absorbers or the instrument. The IO DSCD was found to be (4.09 +/- 0.22) x 10^{13} molec/cm^2.

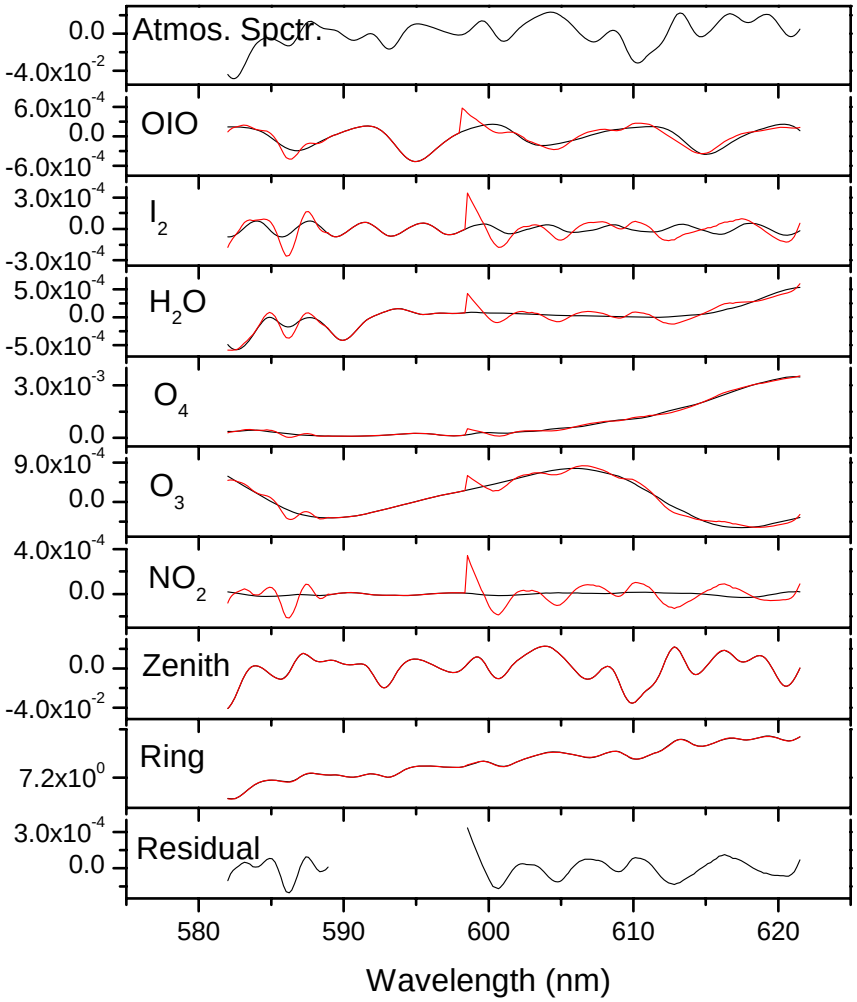

Figure 3.1.5. Example of the spectral analysis of daytime OIO from the 1° elevation viewing angle MAX-DOAS spectrum recorded on 10/18/2006 at 19:34 UT. Black lines represent the spectral references. Red lines represent fit results, i.e. the fitted reference + the residual. The region from 590 to 597 nm was excluded from the analysis due to spectra interferences from either unknown absorbers or the instrument. The OIO DSCD was found to be (1.2 ± 0.11) x 10^{14} molec/cm^{2}.

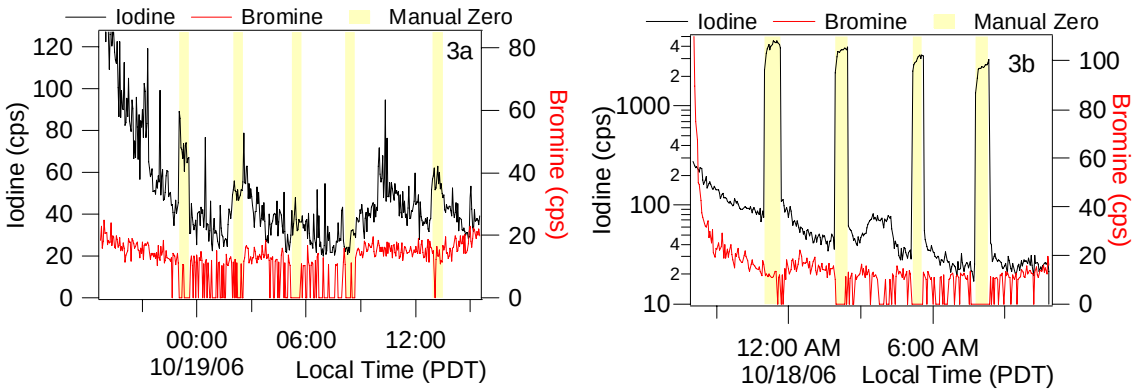

Figure 3.2.1. Impact of denuder placement and composition on I_2 and Br_2 response, shown in counts per second (cps). Data in the left panel were obtained using a denuder coated only with sodium carbonate that was positioned upstream of a 0.8 m ambient air inlet. Data in the right panel were obtained using a denuder coated with sodium carbonate and glycerol that was positioned downstream of a 2.8 m ambient inlet.

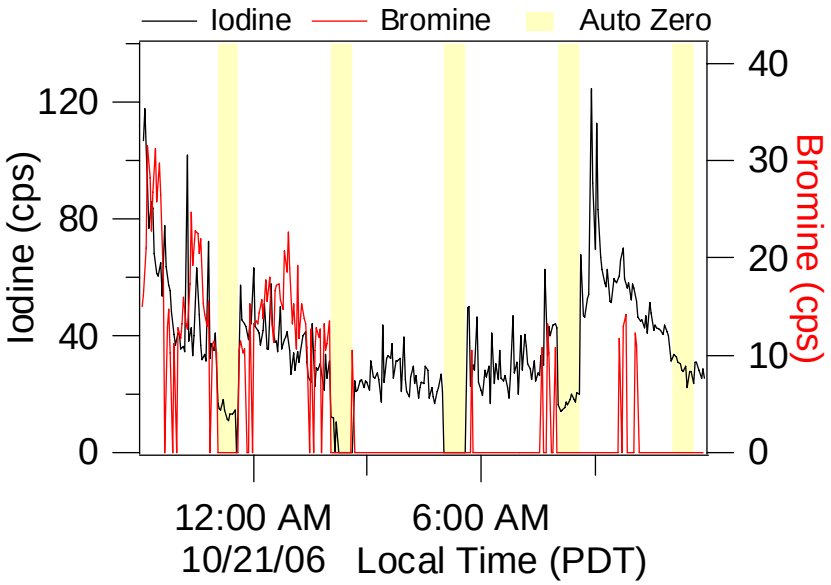

Figure 3.2.2. Iodine and bromine blanks obtained by flooding the ambient inlet with zero air.

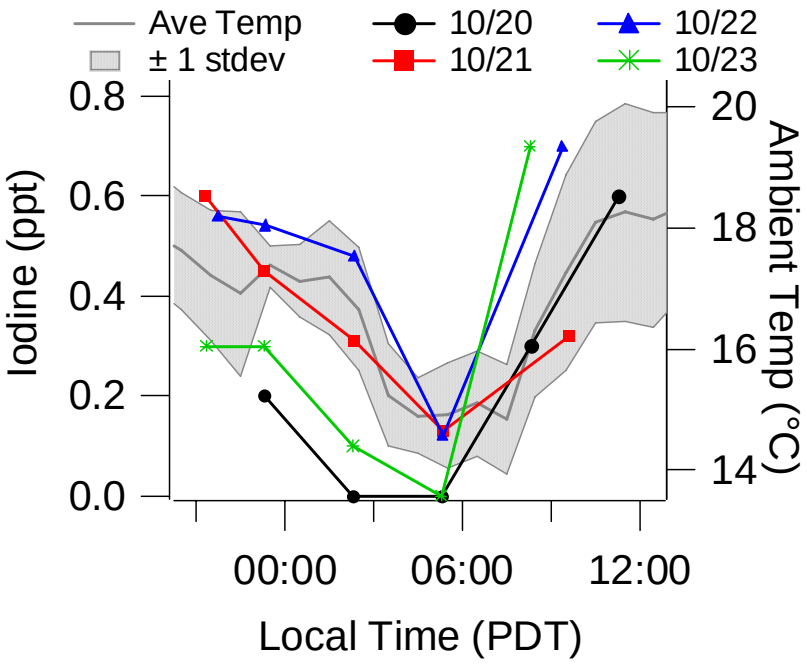

Figure 3.2.3. Automated zero air blanks for iodine plotted as a function of time of day with the average ambient temperature (Oct. 20-23).

Chapter 4

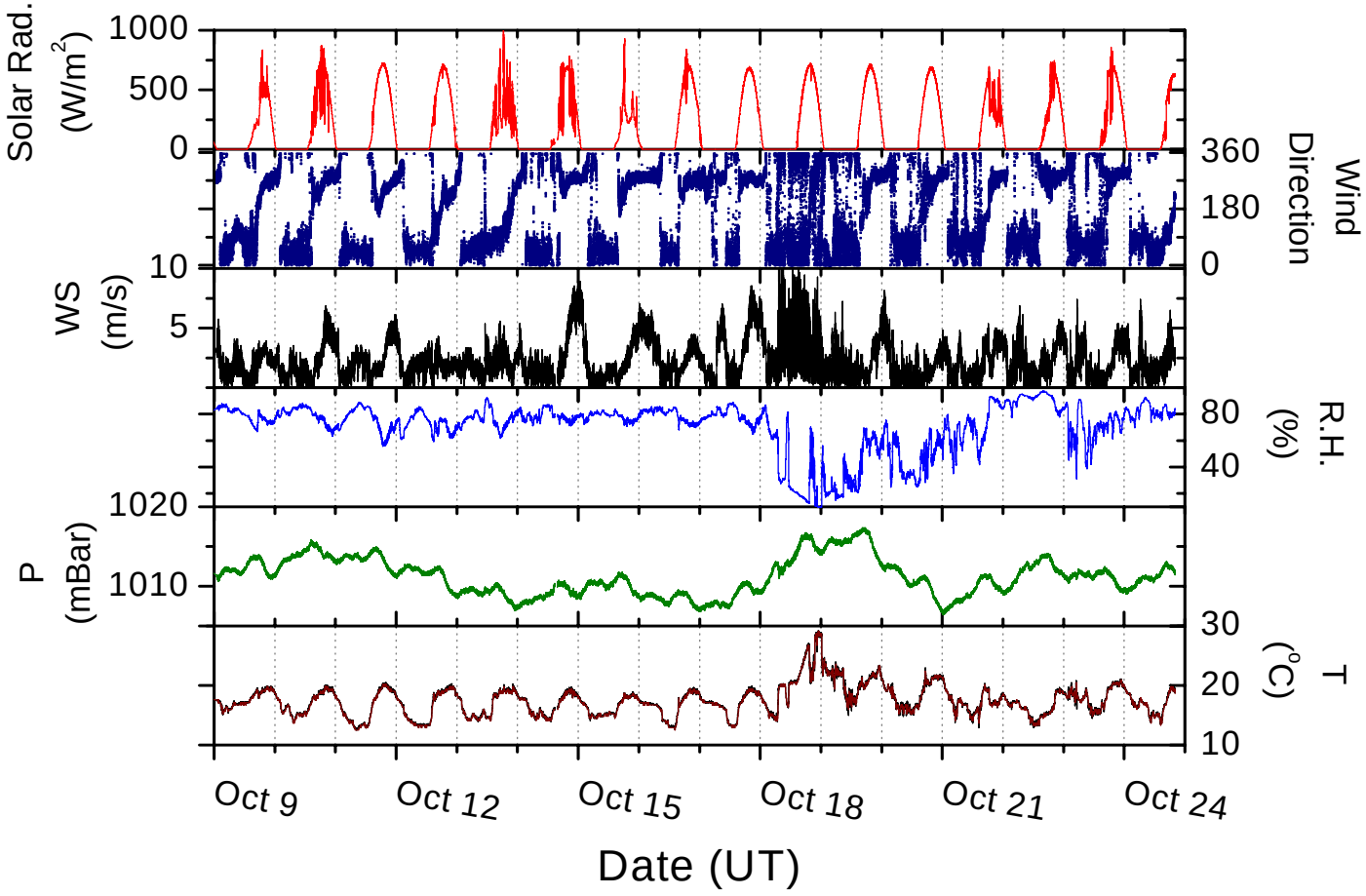

Figure 4.1.1. Meteorological data at Zuma Beach.

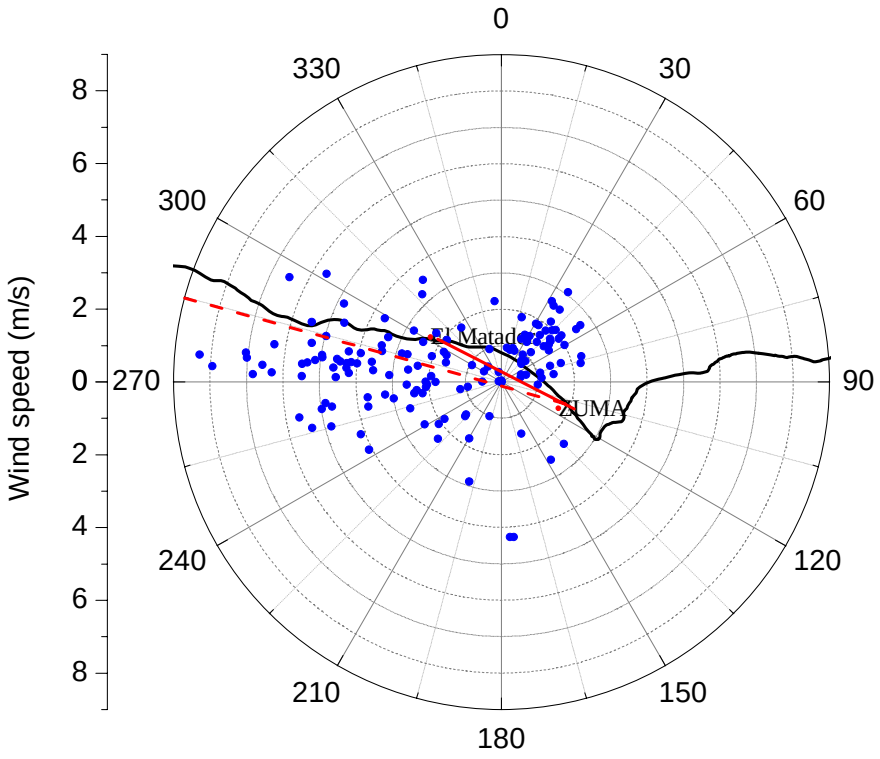

Figure 4.1.2. Daytime measurements of wind speed and wind direction for each LP-DOAS measurement during the CalHal experiment. Wind data were collected by the meteorological station located at the Zuma Beach measurement site. However, DOAS observations are representative of the measurements of concentrations averaged over the LP DOAS light path between the Zuma and El Matador beaches. We assume that wind speed and wind directions variations are negligible along the LP DOAS light path hence placing the center of the wind rose at the center of the LP DOAS light path. The locations of the LP-DOAS light path is indicated by the red solid line, while the viewing direction of the MAX-DOAS is shown as the red dashed line (see also figure 3.1).

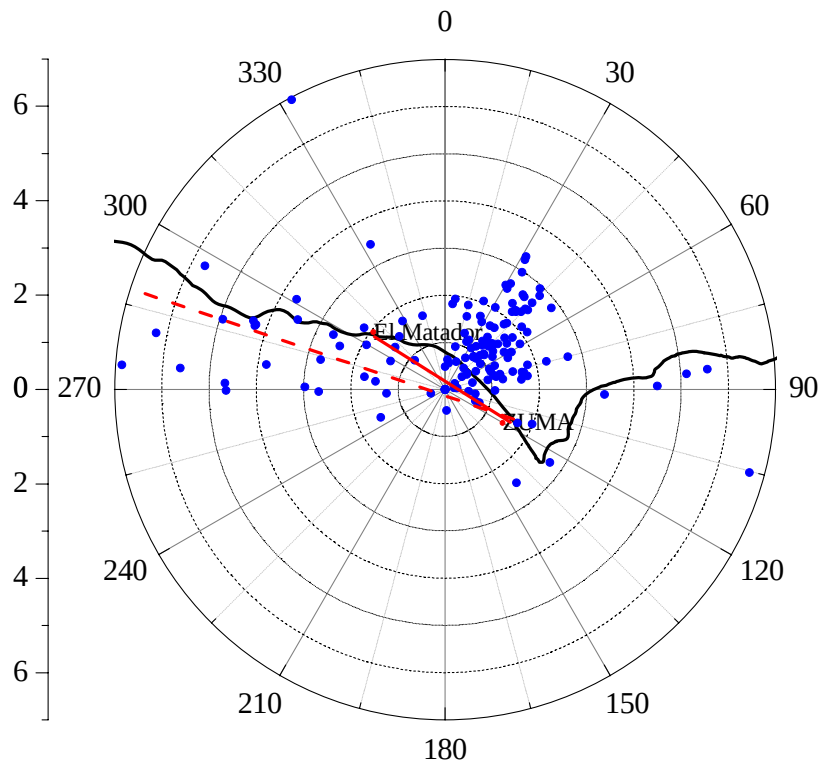

Figure 4.1.3. Nighttime measurements of wind speed and wind direction for each LP-DOAS measurement during the CalHal experiment. Wind data were collected by the meteorological station located at the Zuma Beach measurement site. However, DOAS observations are representative of the measurements of concentrations averaged over the LP DOAS light path between the Zuma and El Matador beaches. We assume that wind speed and wind directions variations are negligible along the LP DOAS light path hence placing the center of the wind rose at the center of the LP DOAS light path. The locations of the LP-DOAS light path is indicated by the red solid line, while the viewing direction of the MAX-DOAS is shown as the red dashed line (see also figure 3.1).

.

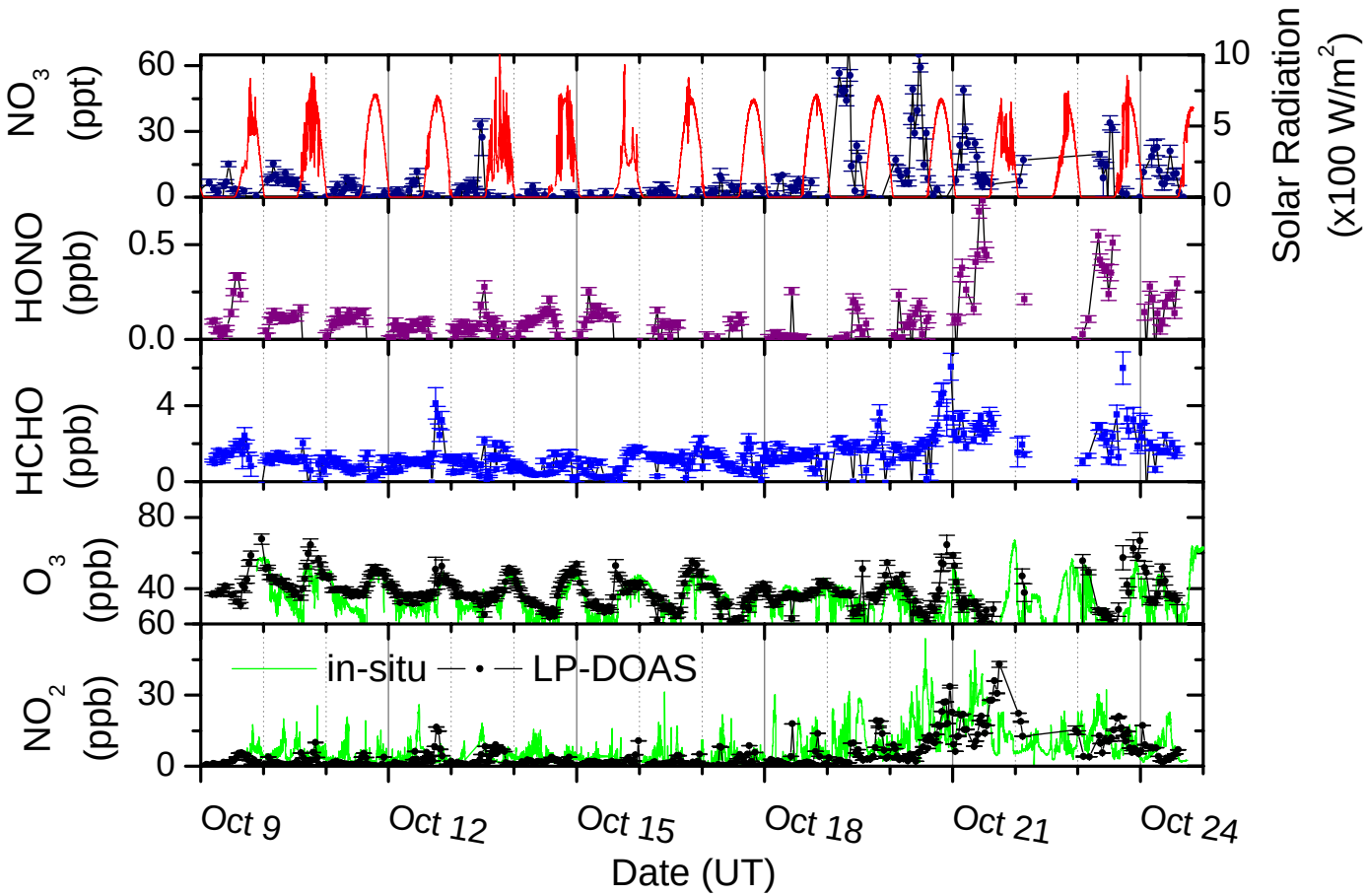

Figure 4.2.1. UCLA LP DOAS and UCI in-situ observations of pollutants at Zuma Beach. Solar radiation data is added to the top panel to orient between day and night.

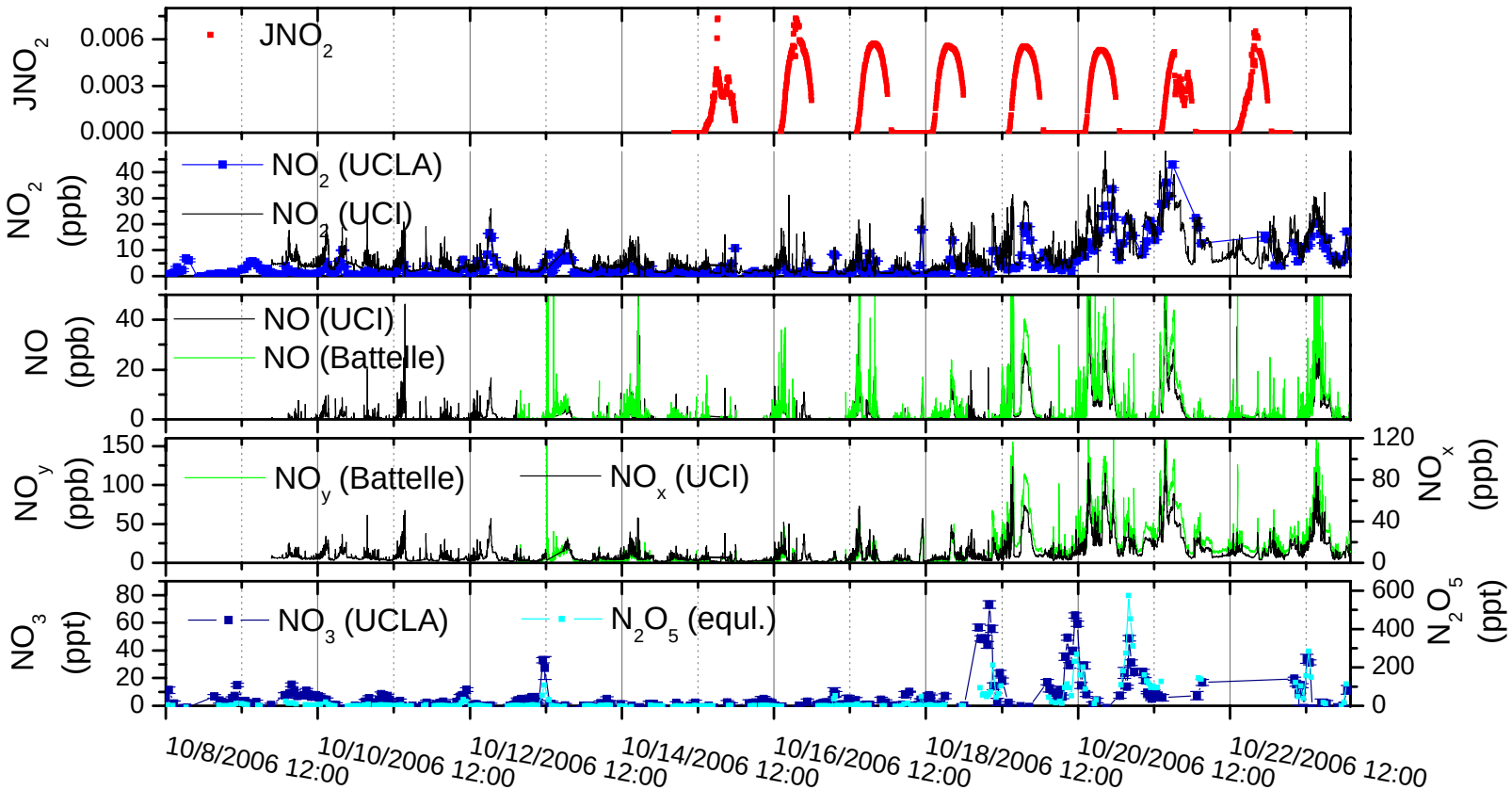

Figure 4.2.2 Observations of various nitrogen oxide species, NO_y, and the photolysis frequencies of NO_2.

.

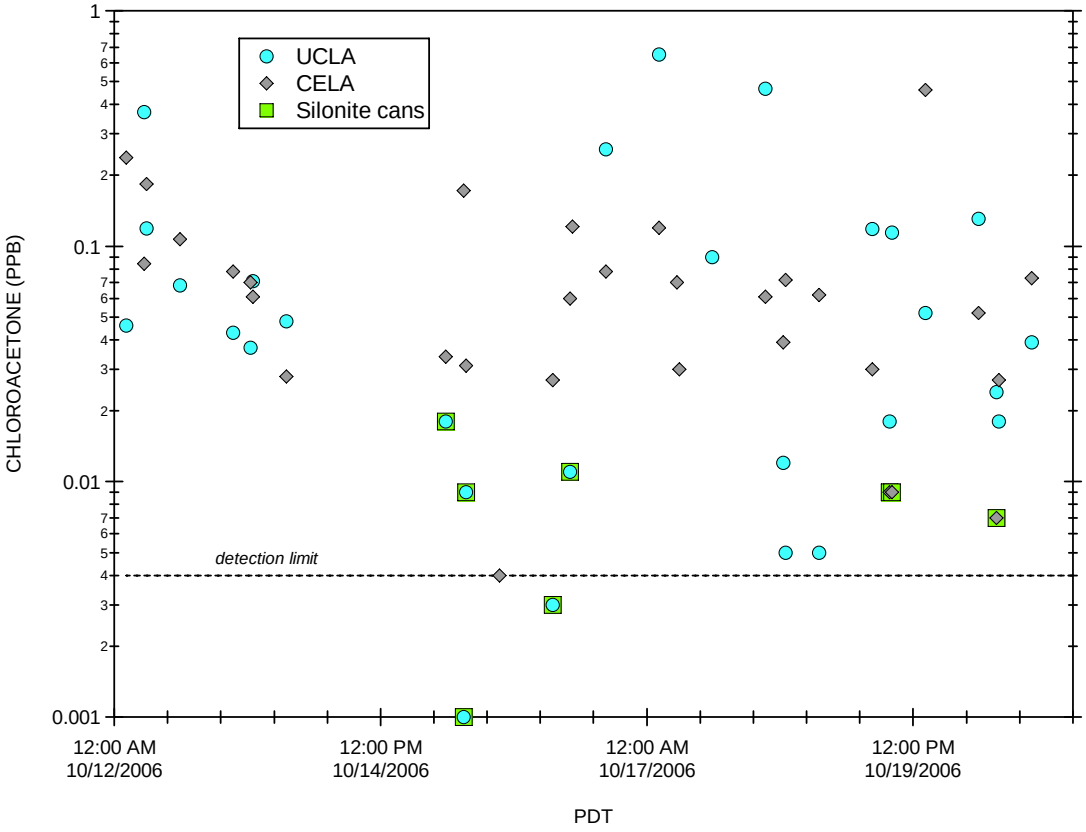

Figure 4.3.1. Chloroacetone mixing ratios initially measured in canister samples collected at the UCLA (circles) and CELA (diamonds) sites. The 4 ppt detection limit for chloroacetone is given as the dashed line. Symbols highlighted with squares are samples collected into Silonite treated canisters (Entech Inc.). Six out of a total of 12 Silonite canisters contained chloroacetone above the detection limit. (Two samples were collected only 30 minutes apart and overlap in the figure.)

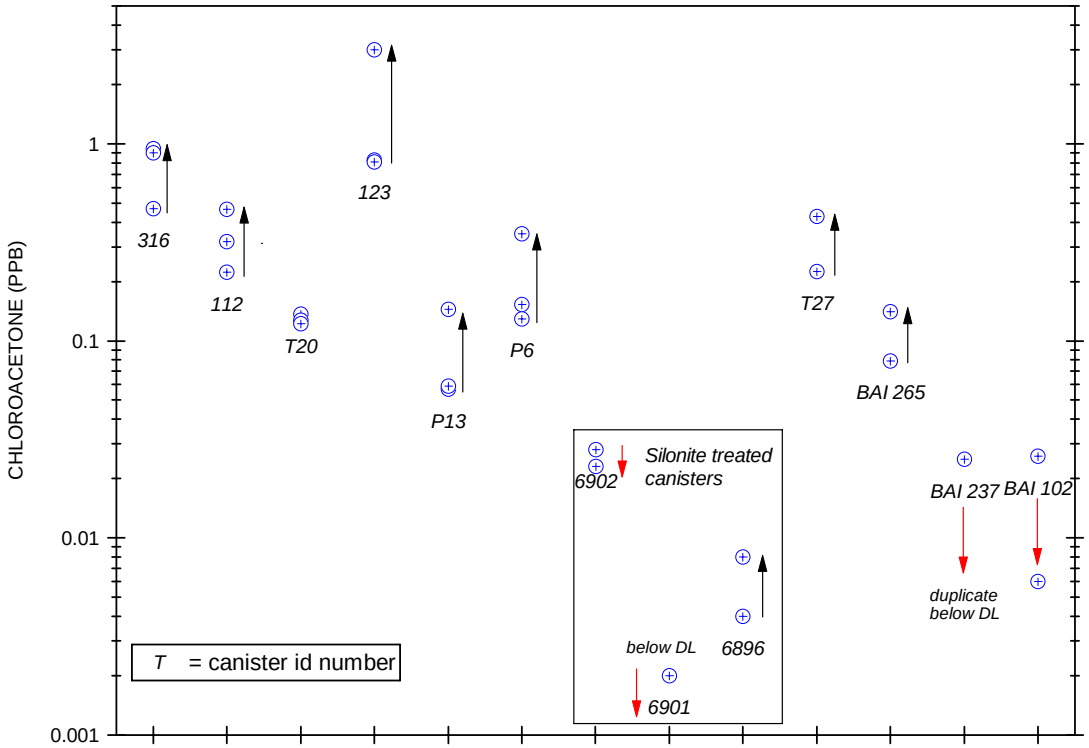

Figure 4.3.2. Replicate sample analysis results for chloroacetone. Thirteen canister samples were analyzed in duplicate or triplicate. Chloroacetone increased in most canisters with storage time (up arrows) but decreased in some canisters (down arrows).

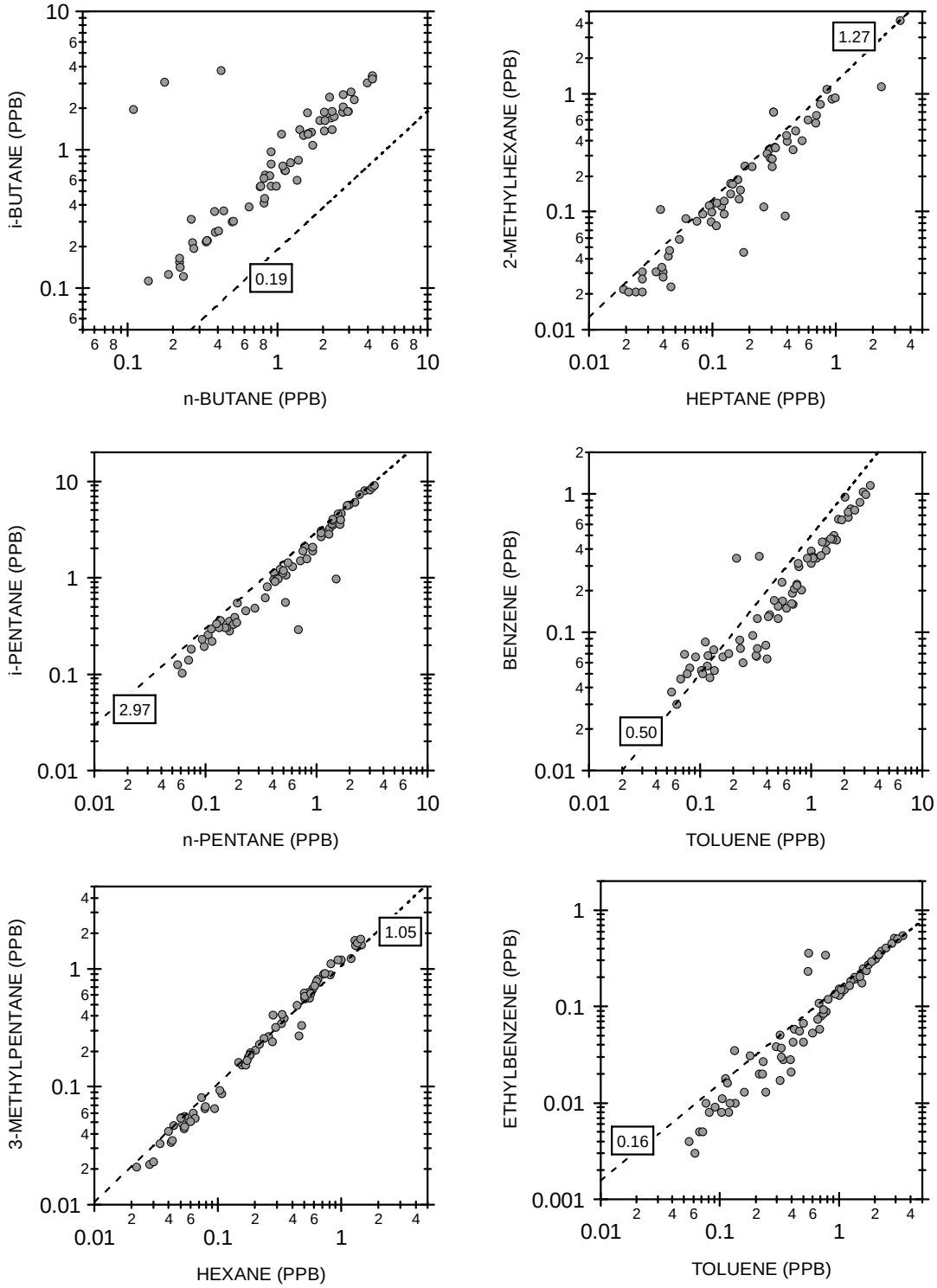

Figure 4.3.3. Correlations between hydrocarbon groups from Table 4.3 illustrating the generally good agreement of the canister data with the auto exhaust ratio shown as the dashed line. With the exception of benzene vs. toluene, the plotted pairs have very similar OH reaction rate coefficients but significantly different Cl atom rate coefficients.

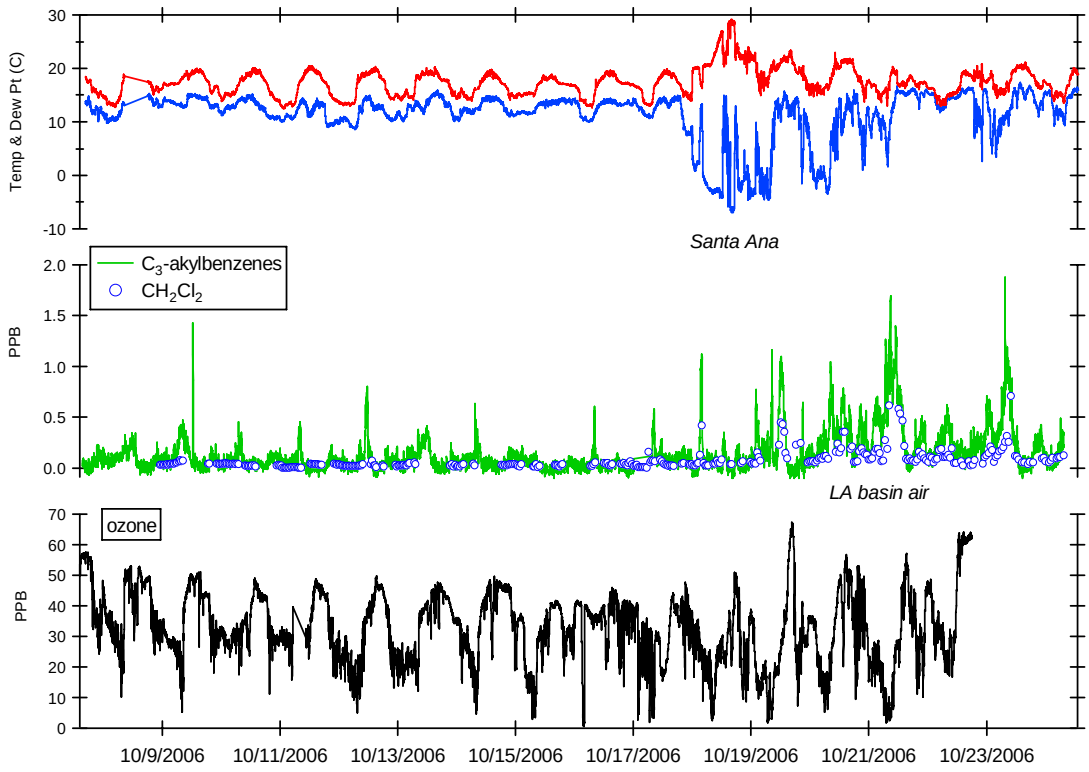

Figure 4.3.4. Hydrocarbon mixing ratios measured at Zuma Beach. Middle plot shows sum of C_3-alkylbenzene isomers as measured by the PTR-MS and CH_2Cl_2 mixing ratios as measured by GC-MS. Upper panel shows temperature (red) and dew point (blue) and bottom panel O_3 mixing ratios.

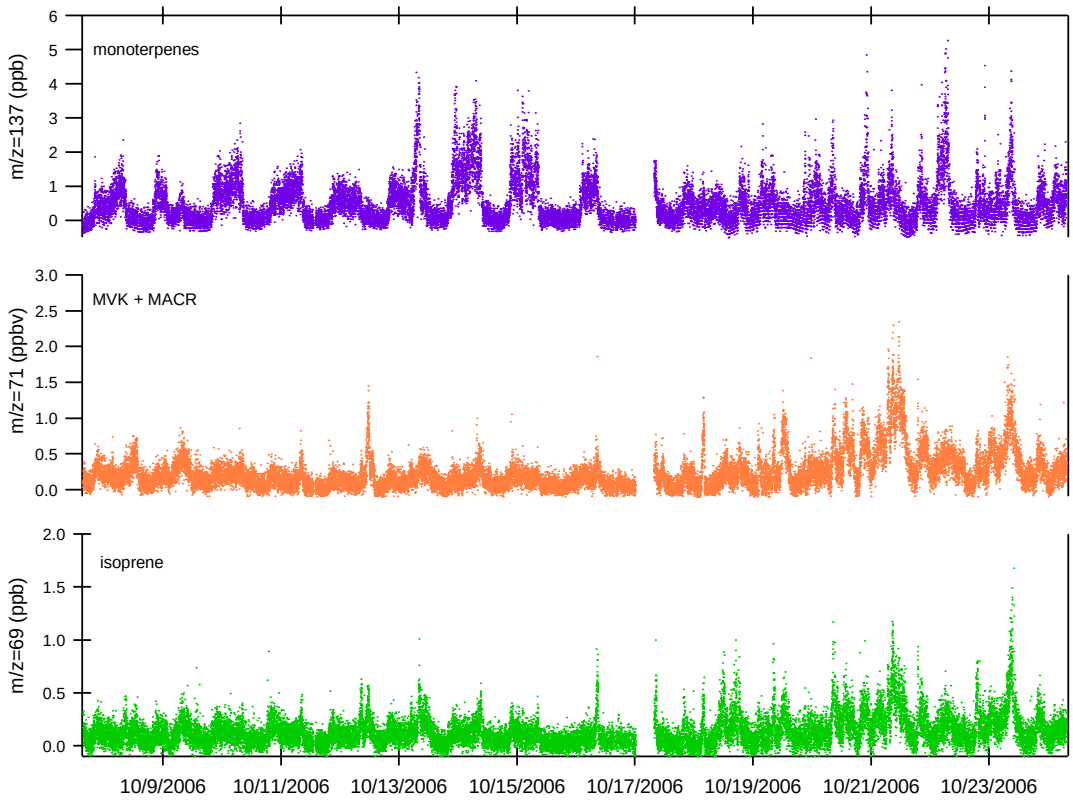

Figure 4.3.5. Zuma Beach time series isoprene, the sum of MACR and MVK, and monoterpene isomers as measured by the PTR-MS instrument.

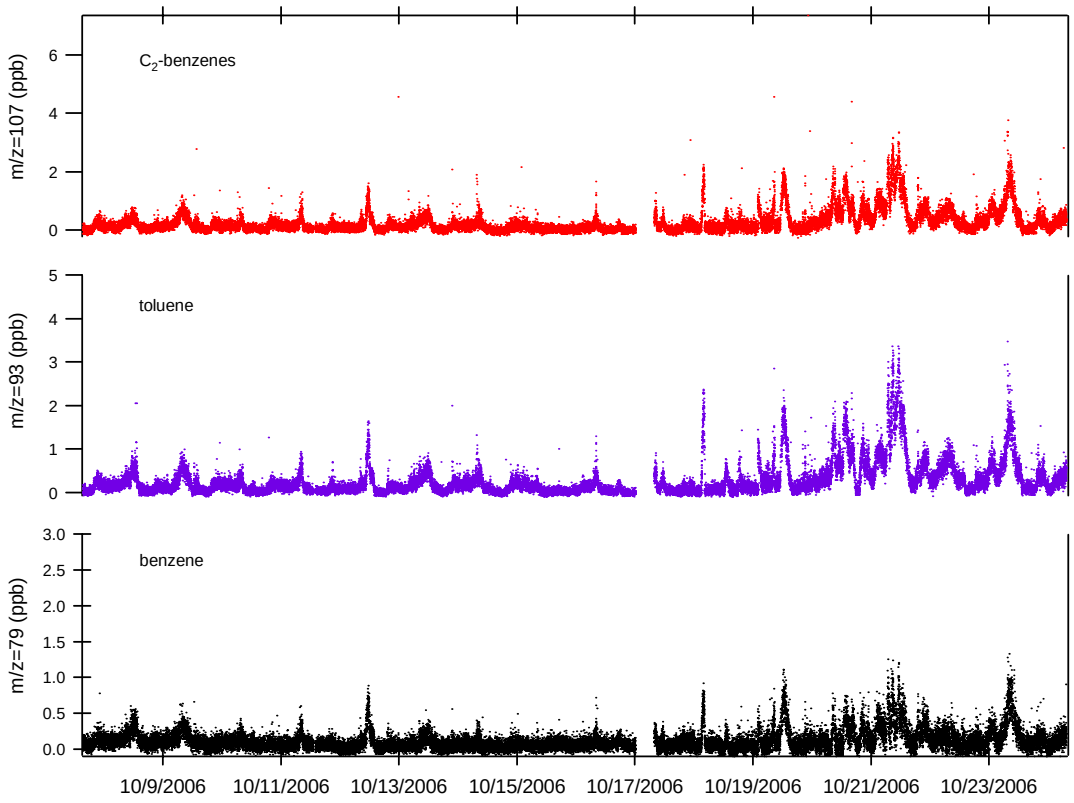

Figure 4.3.6. Zuma Beach time series of benzene, toluene, and the sum of C_2-alkylbenzene isomers as measured by the PTR-MS instrument.

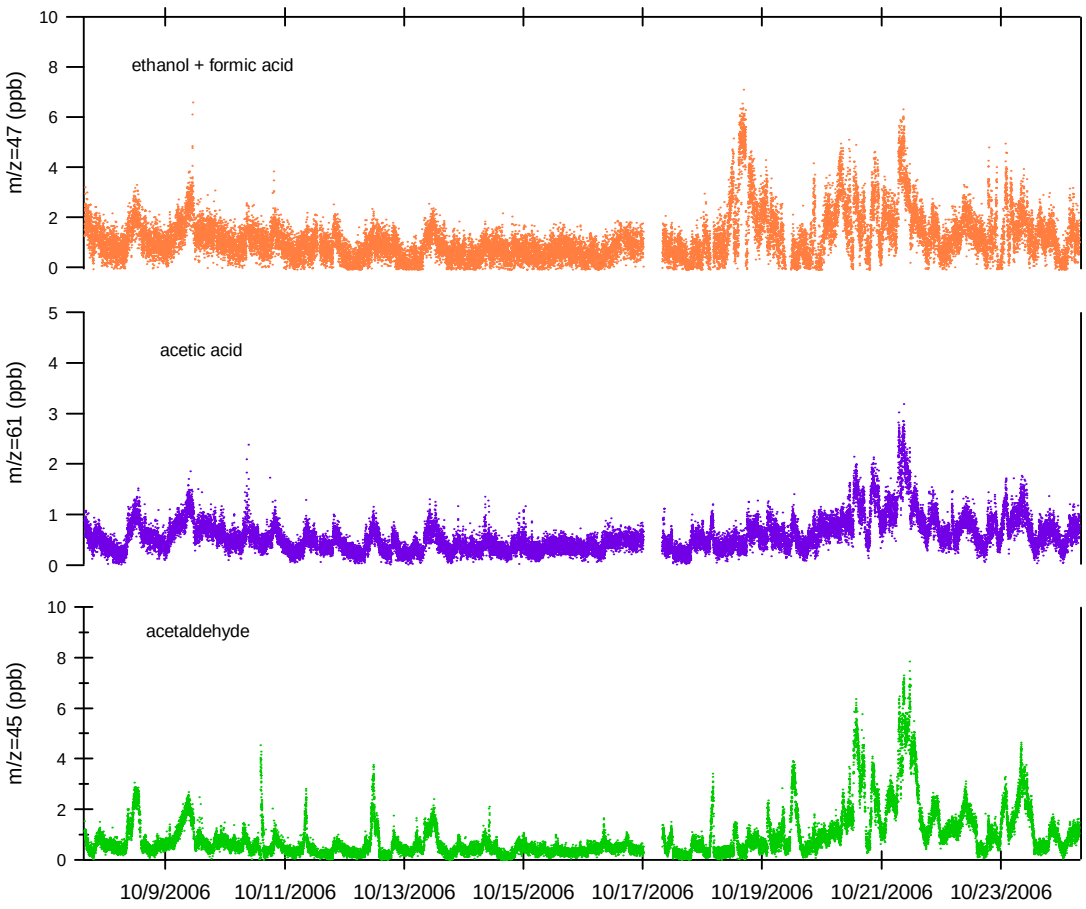

Figure 4.3.7. Zuma Beach time series of acetaldehyde, m/z=61 assumed to be acetic acid, and m/z=47 attributed to ethanol and formic acid.

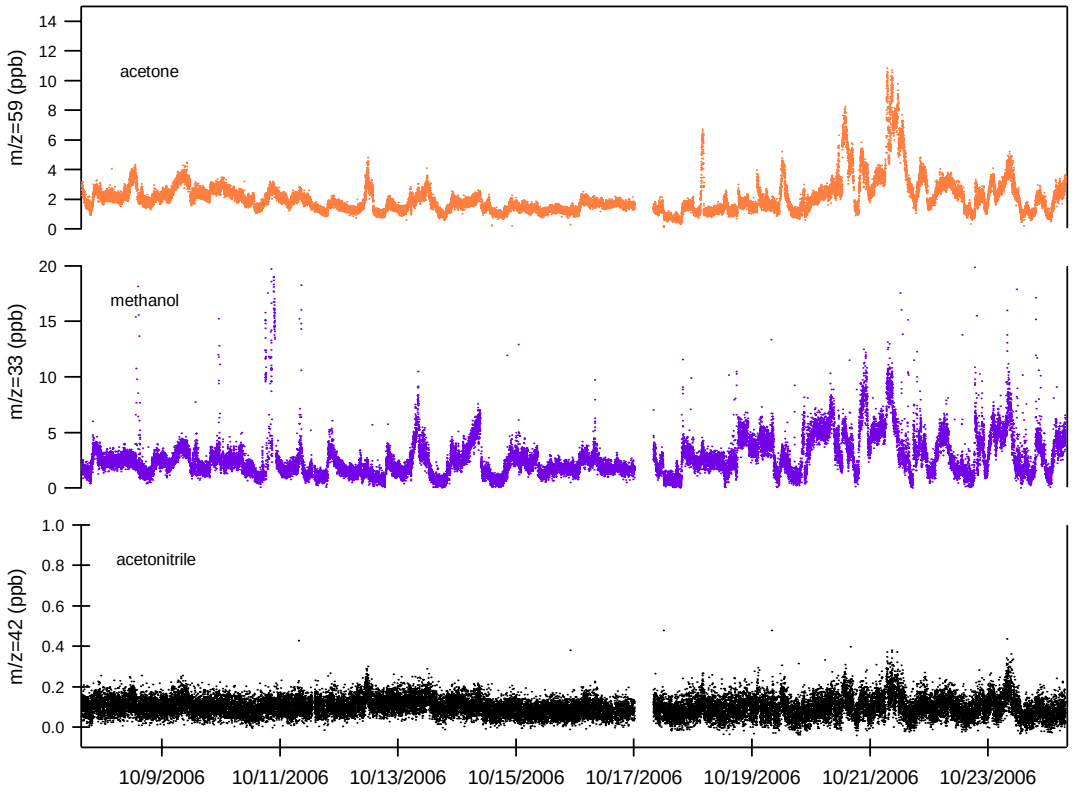

Figure 4.3.8. Zuma Beach time series of acetonitrile, methanol, and acetone as measured by the PTR-MS instrument.

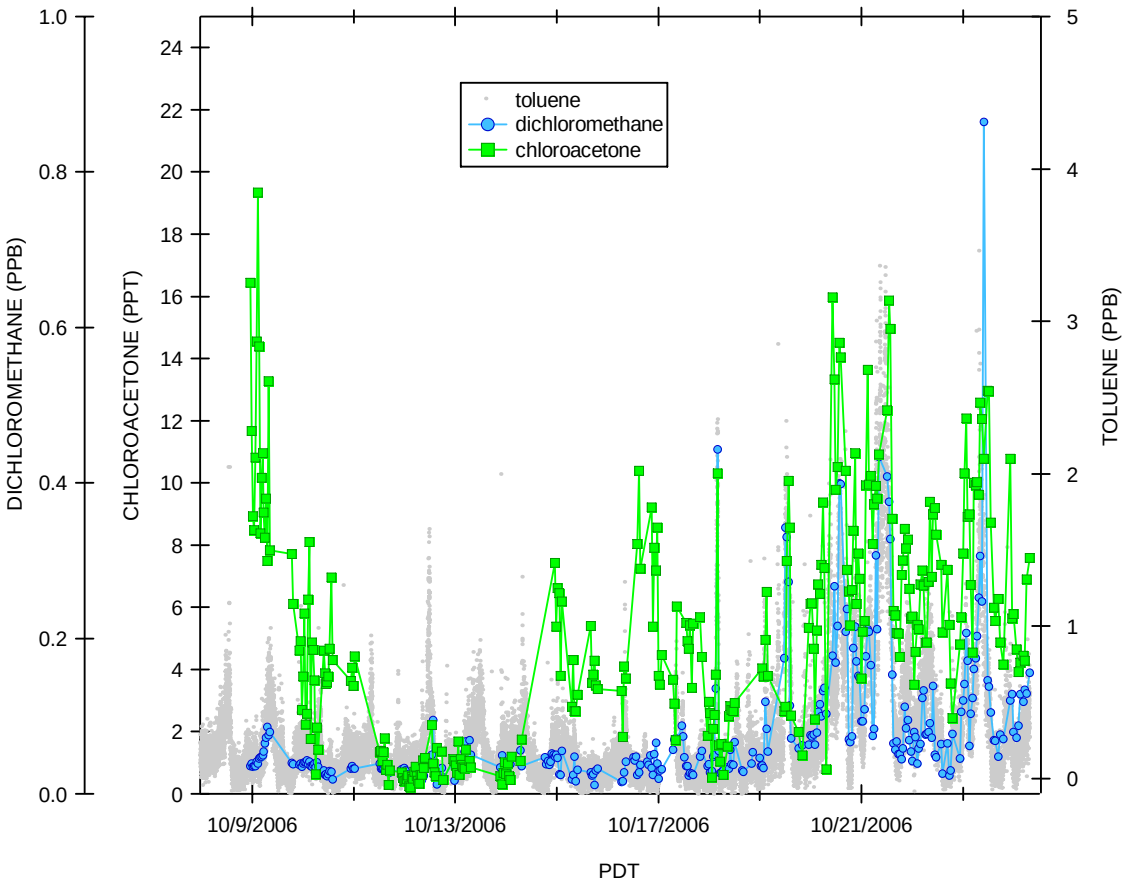

Figure 4.3.9. Zuma Beach time series of chloroacetone and CH_2Cl_2 mixing ratios measured by in-situ GC-MS and toluene mixing ratios measured by PTR-MS. Chloroacetone was significantly above the 4 ppt detection limit during three periods: clean air period from Oct 9 to Oct 10, clean air period from October 16 to October 18, and during a polluted period of LA basin outflow from October 19 to October 24.

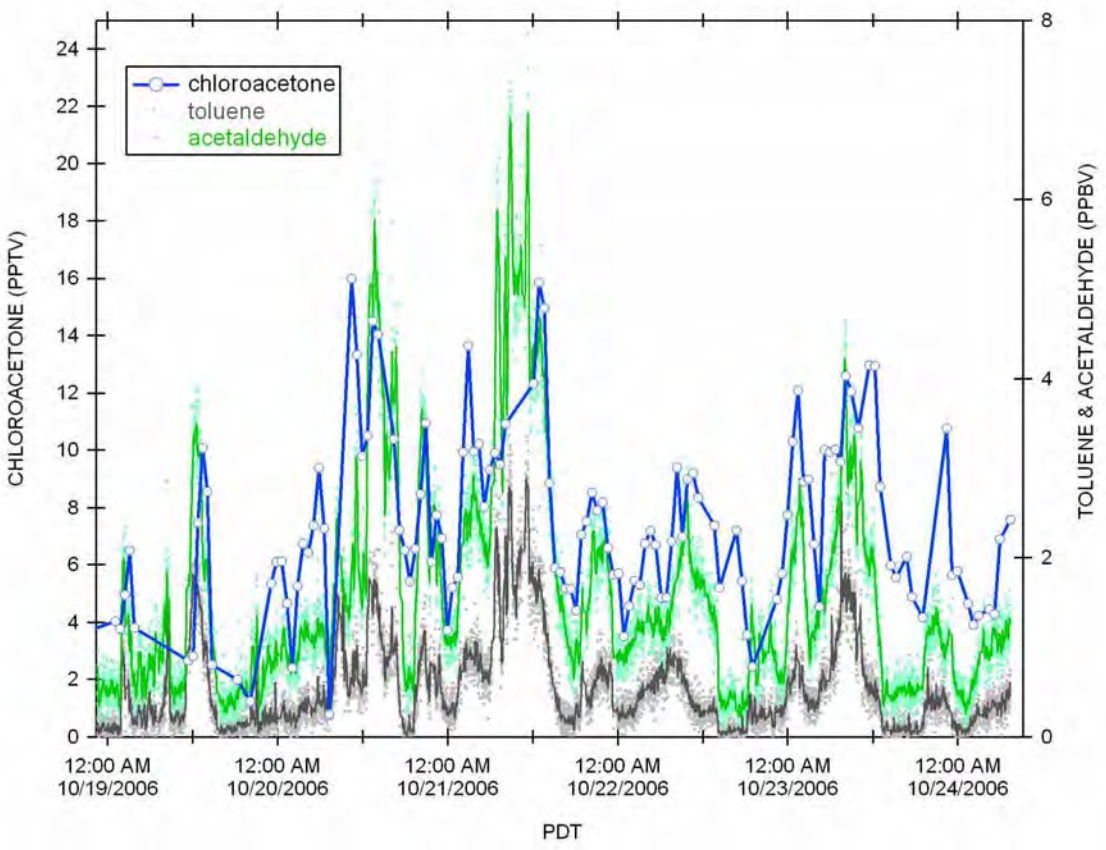

Figure 4.3.10. Time series of the October 19 to October 24 LA basin outflow period showing chloroacetone, toluene, and acetaldehyde mixing ratios. Lines through toluene and acetaldehyde data points are 11-point box smooth averages of the data.

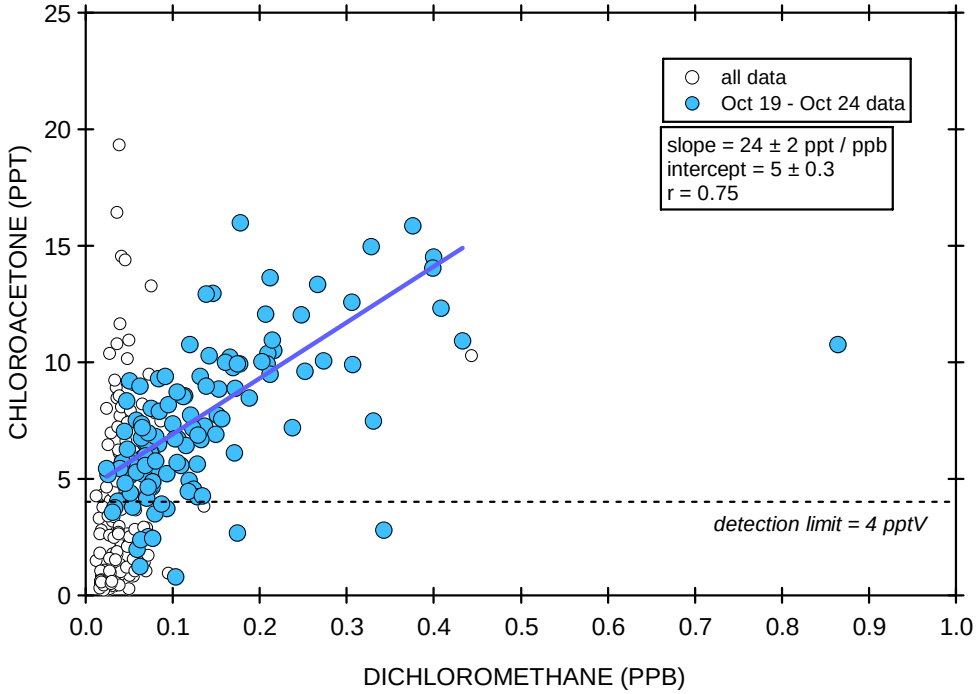

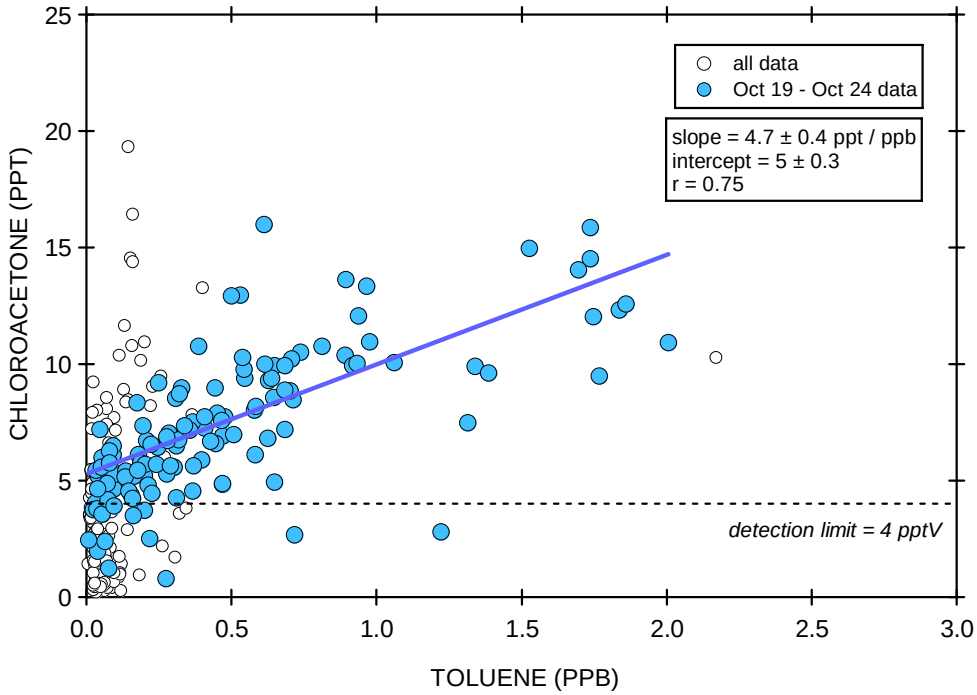

Figure 4.3.11. Zuma Beach data correlations between chloroacetone and a long lived urban air tracer CH_2Cl_2 (upper panel), and a short lived tracer toluene (lower panel). Linear regressions are shown through the LA basin air period from October 19 to October 24 for data above the 4 ppt chloroacetone detection limit.

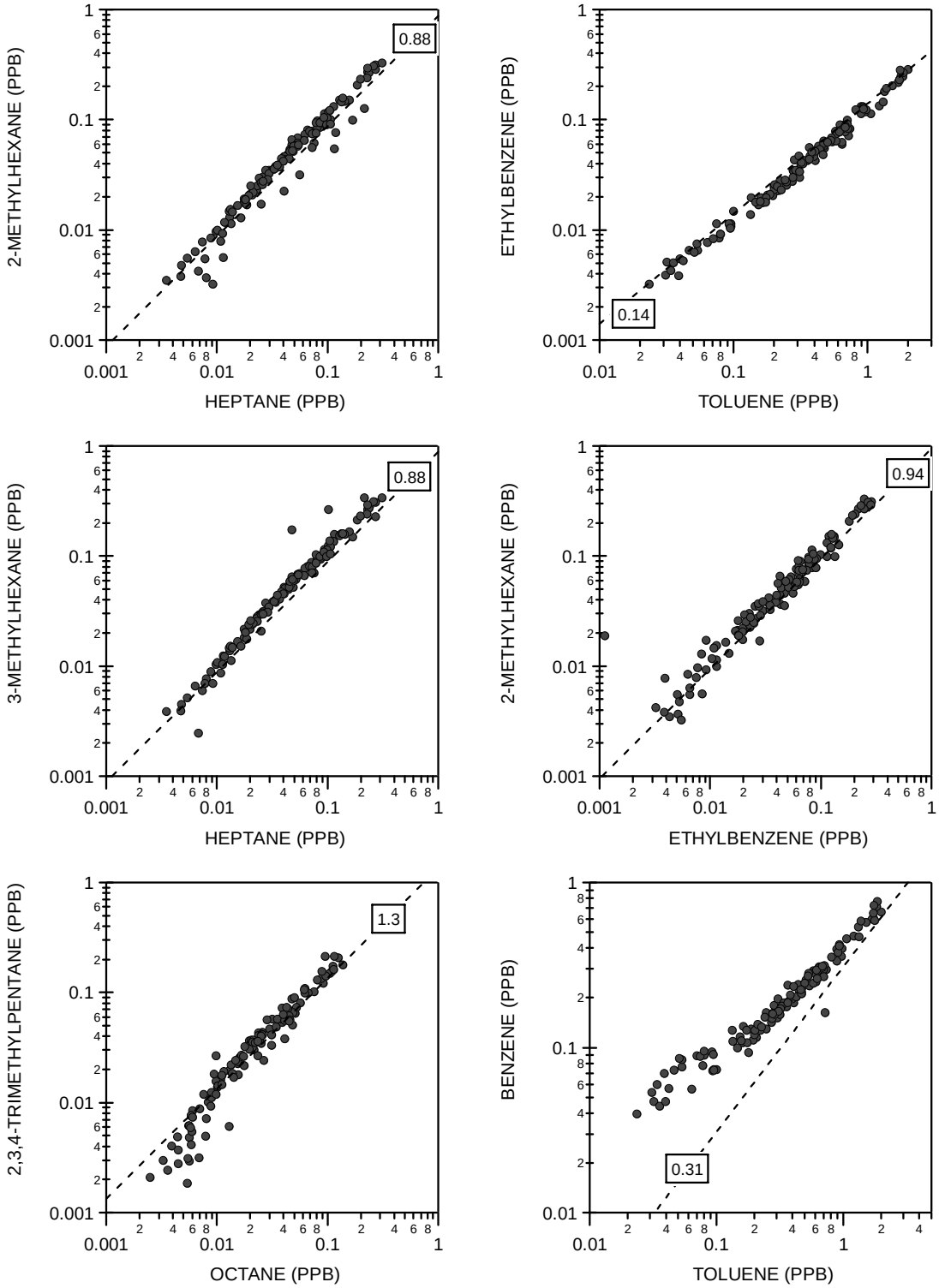

Figure 4.3.12. Correlations between Zuma Beach hydrocarbons with similar OH rate coefficients but significantly different Cl-atom rate coefficients. The data trends are in good agreement with the urban source ratio observed from the CELA canister samples shown as the dashed line.

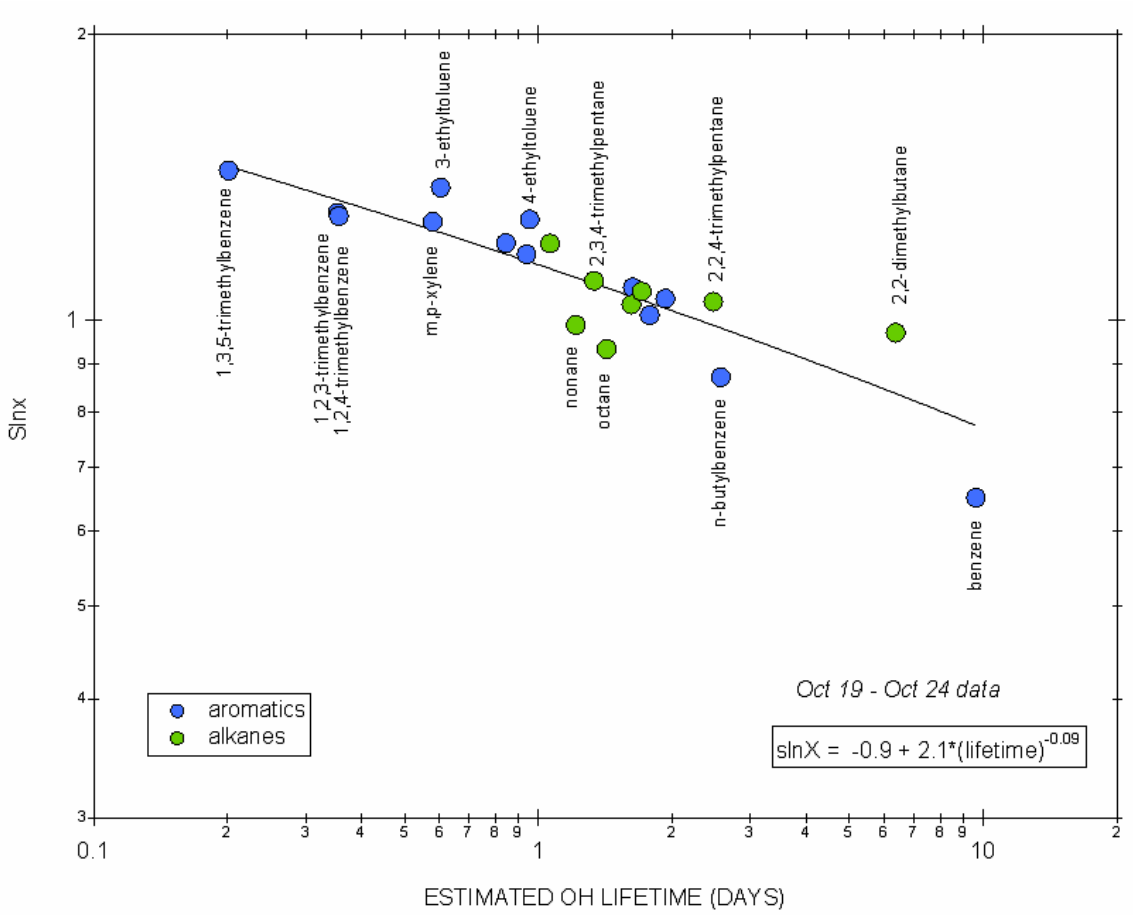

Figure 4.3.13. Measure of variability vs. estimated OH lifetime for hydrocarbons measured by GC-MS at Zuma Beach during the LA basin air outflow period. Plot illustrates only a weak lifetime dependence, indicating that much of the mixing ratio temporal variability was caused by varying degrees of urban plume dilution rather than chemical processing.

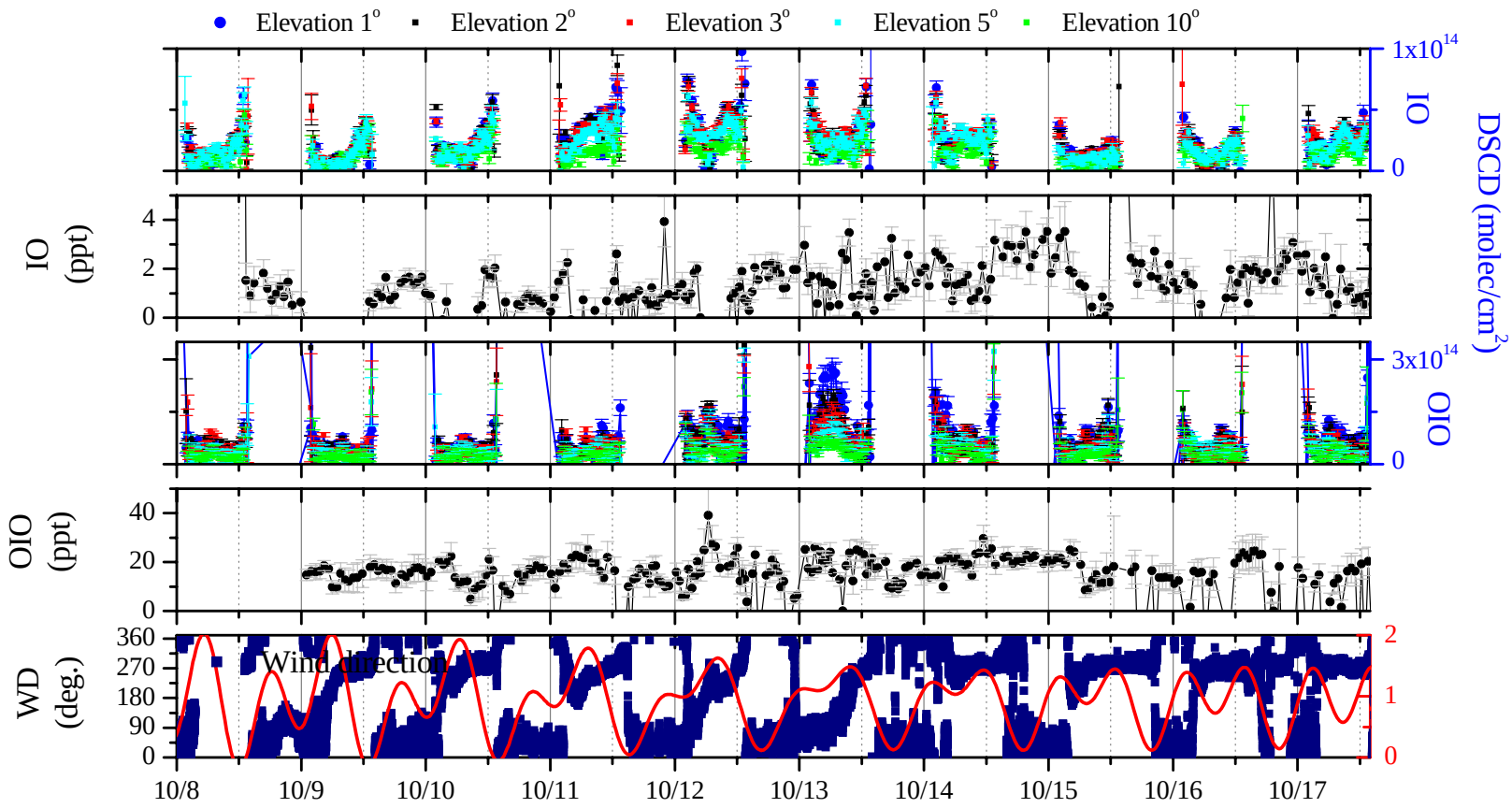

Figure 4.5.1 Overview of observations at Zuma Beach. Top two panels show IO mixing ratios and DSCDs measured by the MAX-DOAS instrument at 1, 2, 3, 5, and 10 degrees elevation viewing angles, and mixing ratios measured by the LP-DOAS respectively. Panels three and four show the same for OIO. Since MAX-DOAS data are only available during the day, it provides orientation for the day and nighttime. The lower panel shows wind direction measured by the UCLA meteorological station at Zuma Beach as well as tidal height.

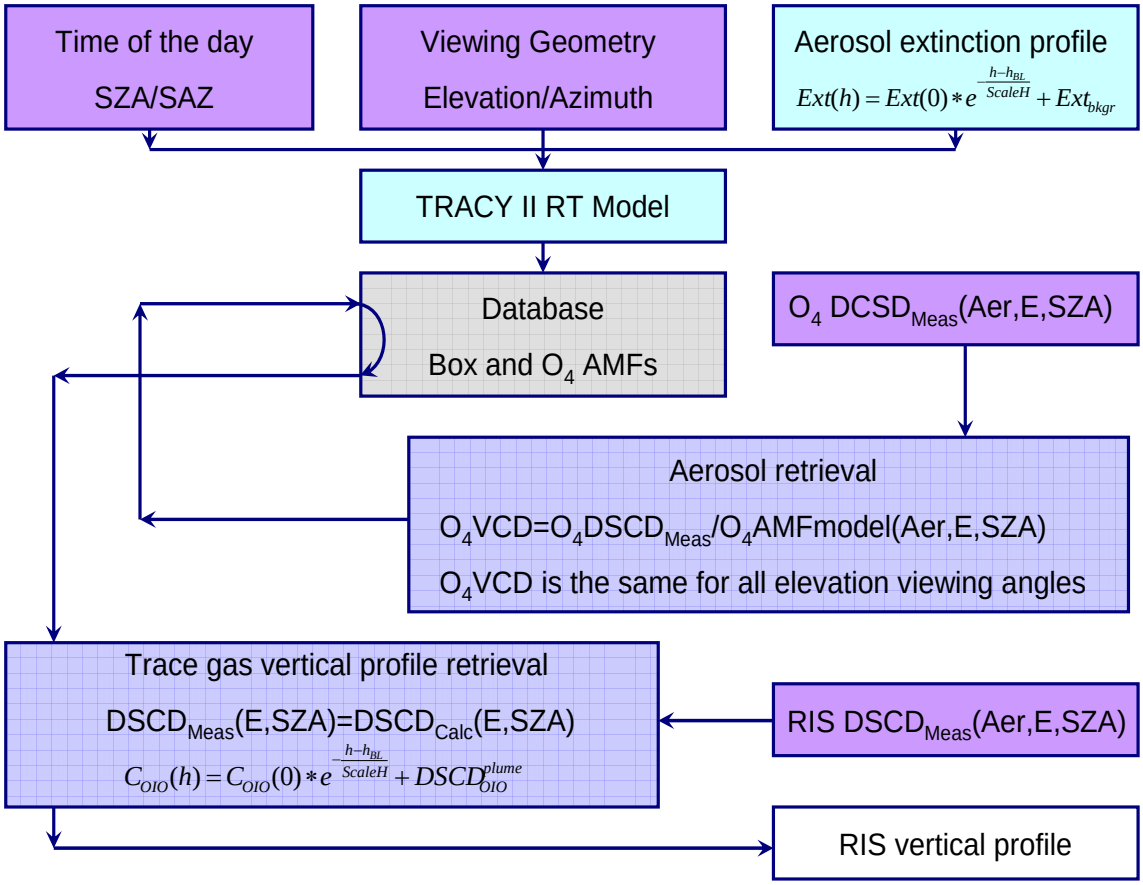

Figure 4.5.2. OIO vertical profile retrieval algorithm.

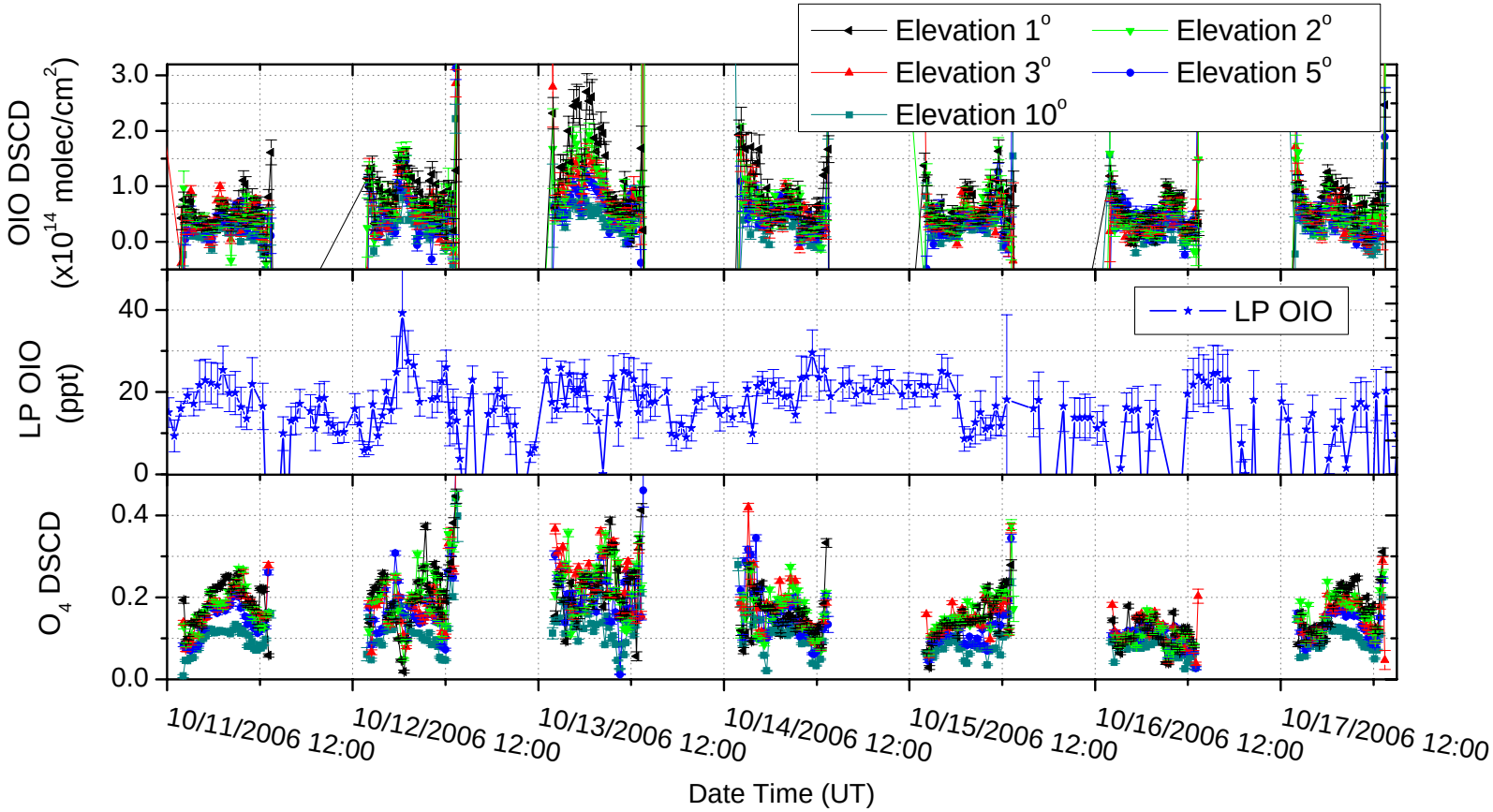

Figure 4.5.3. Zuma OIO DOAS measurement overview. Top panel shows MAX-DOAS OIO DSCDs measured at 1°, 2°, 3°, 5° and 10° elevation viewing angles; middle panel shows LP DOAS OIO mixing ratios; and bottom panel shows MAX-DOAS O_4 DSCDs from the 530 nm center wavelength spectra for all five elevation viewing angles.

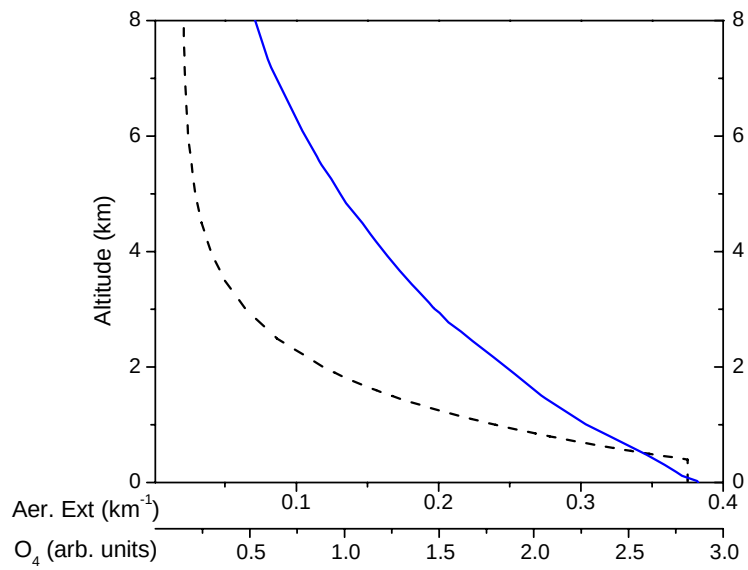

Figure 4.5.4. Example of an aerosol profile (dashed black line) generated during the aerosol retrieval process and the O_4 vertical profile (solid blue line) used for RT calculations. Parameters for this aerosol profile are H_{BL}= 400 m; Ext_{BL} = 0.355 km^{-1}; *ScaleH* = 1; Ext_{Bckgr} = 0.02 km^{-1}. O_4 profile was constructed using atmospheric T and P vertical profiles. For Zuma Beach, profiles collected by airplanes on approach to LAX were used [provided by ACARS database http://www.acarsd.org/].

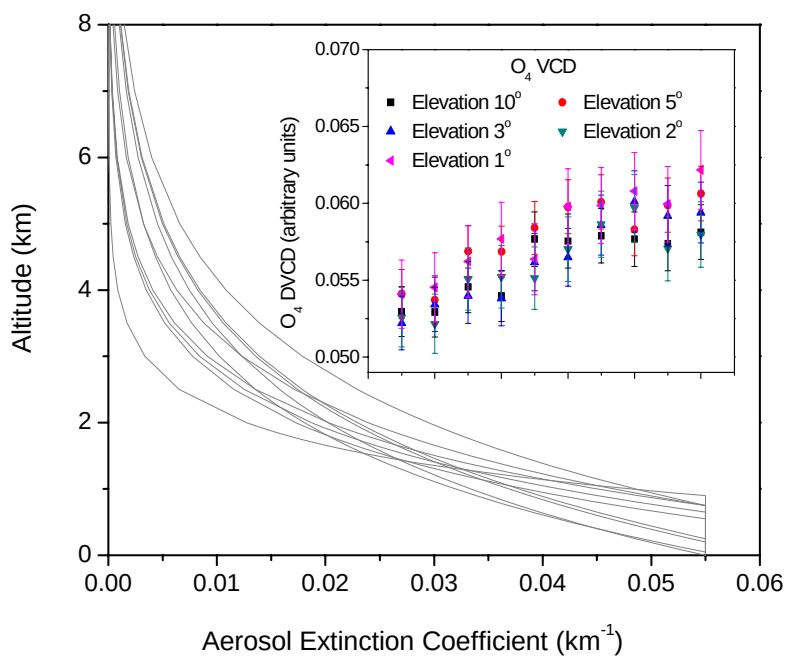

Figure 4.5.5. Example of the aerosol profile retrieval. Gray lines show aerosol profiles that satisfy requirement for O_4 VCDs for all elevations to be equal within errors. This is illustrated in the inset figure that shows O_4 VCDs for all presented aerosol profiles. For each of the profile, VCDs at all elevation viewing angles agree within the error bars.

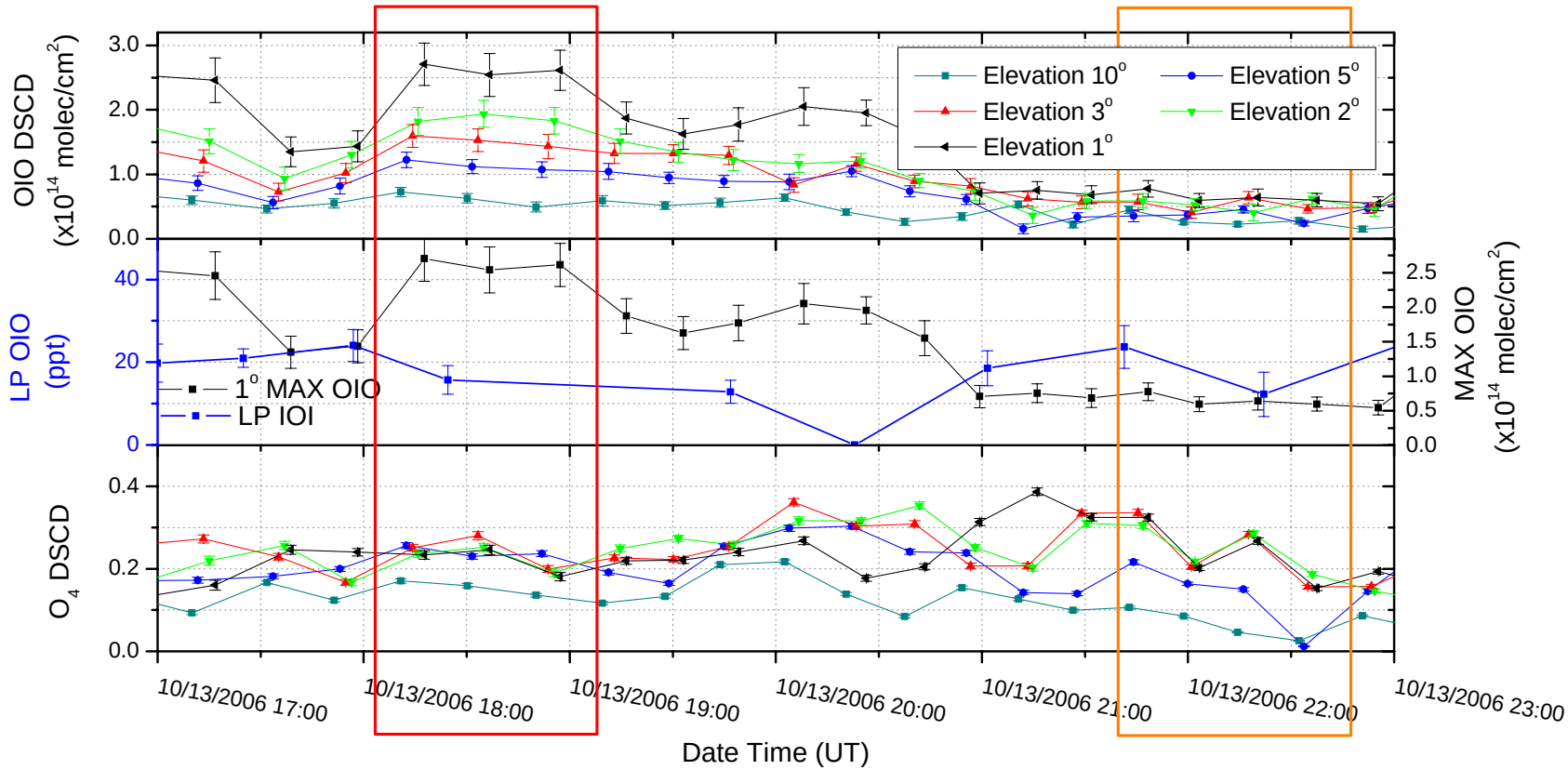

Figure 4.5.6. Overview of OIO MAX- and LP DOAS measurements on October 13, 2006. See text for description of outline boxes.

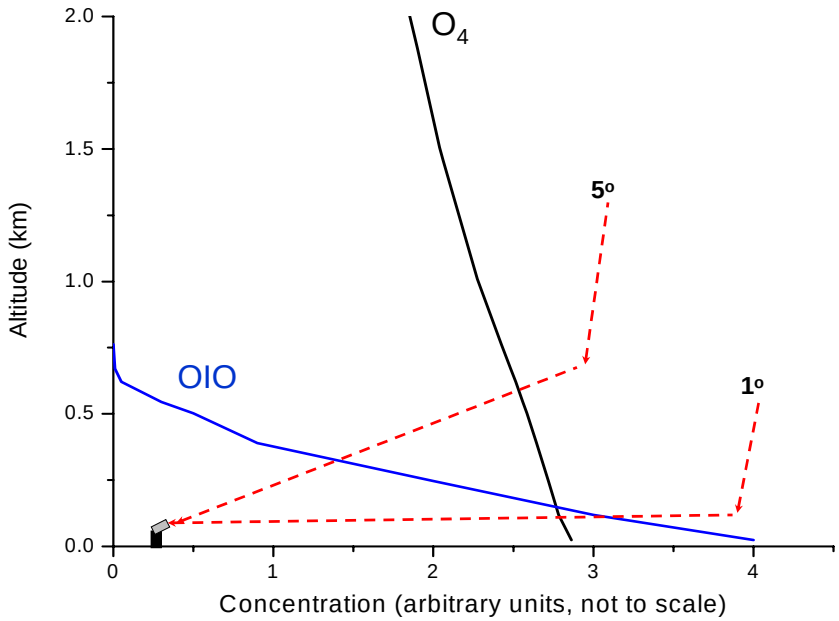

Figure 4.5.7. Schematic representation of MAX-DOAS light paths for 1° and 5° elevation viewing angles (dashed lines). The O_4 atmospheric profile (black line) slowly changes with altitude and the hypothetical OIO profile (blue line) is very close to the surface.

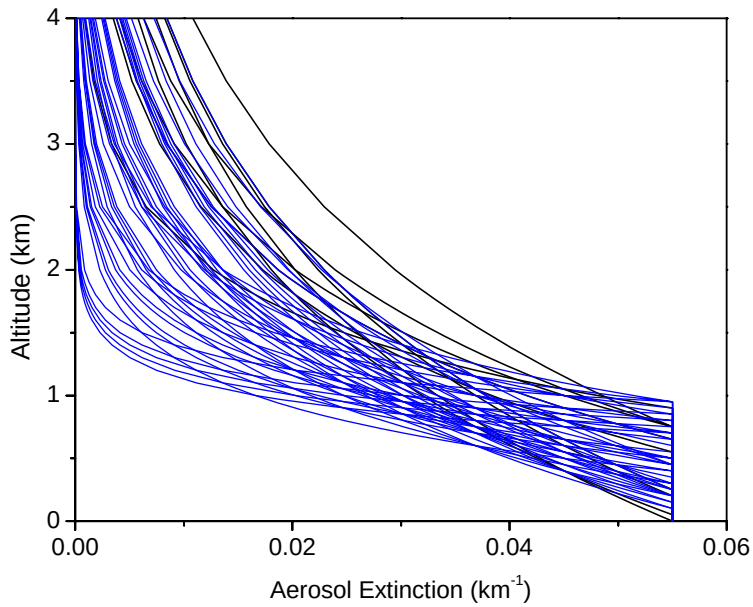

Figure 4.5.8. Aerosol retrievals for October 13, 2006 between 18:10 and 18:30 UT in Malibu, CA.

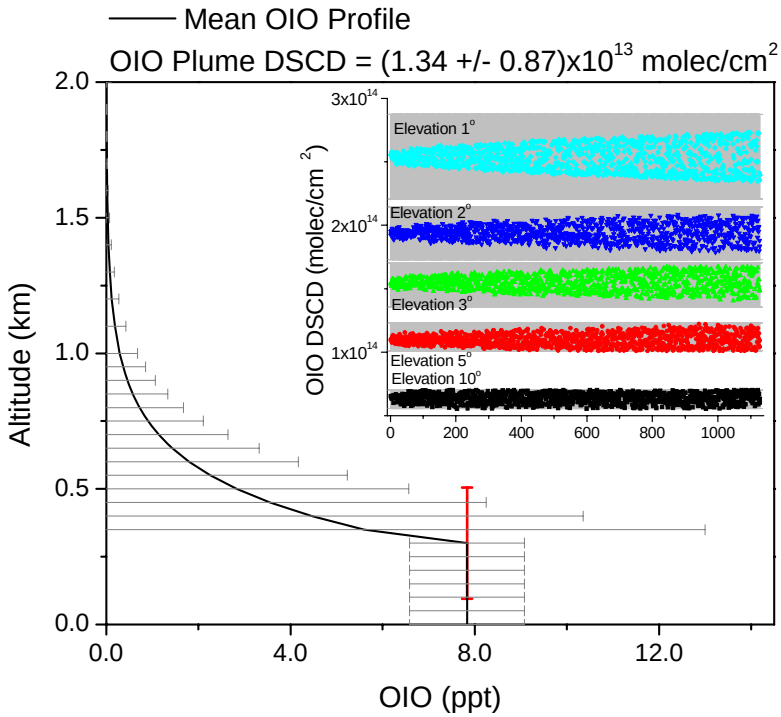

Figure 4.5.9. OIO vertical profile retrieved for October 13, 2006 at 18:30 UT. In addition to the homogeneous profile showed here, there is also 1.34 (± 0.87) × 10^{13} molec/cm^2 OIO present in the marine boundary layer in the inhomogeneous plumes.

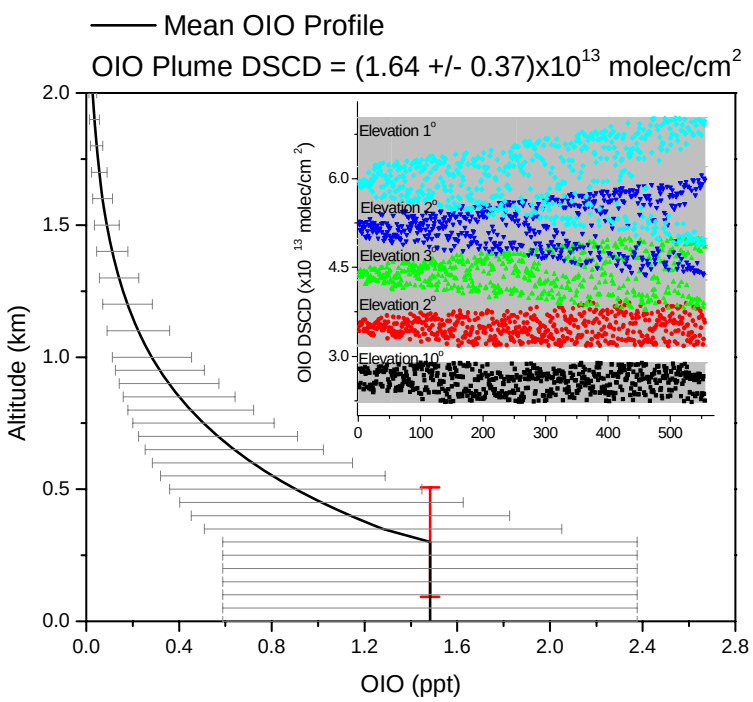

Figure 4.5.10. OIO vertical profile retrieval for October 13, 2006 at 22:03 UT. In addition to the homogeneous profile showed here, there is also 1.64 (± 0.37) × 10^{13} molec/cm^2 OIO present in the marine boundary layer in the inhomogeneous plumes.

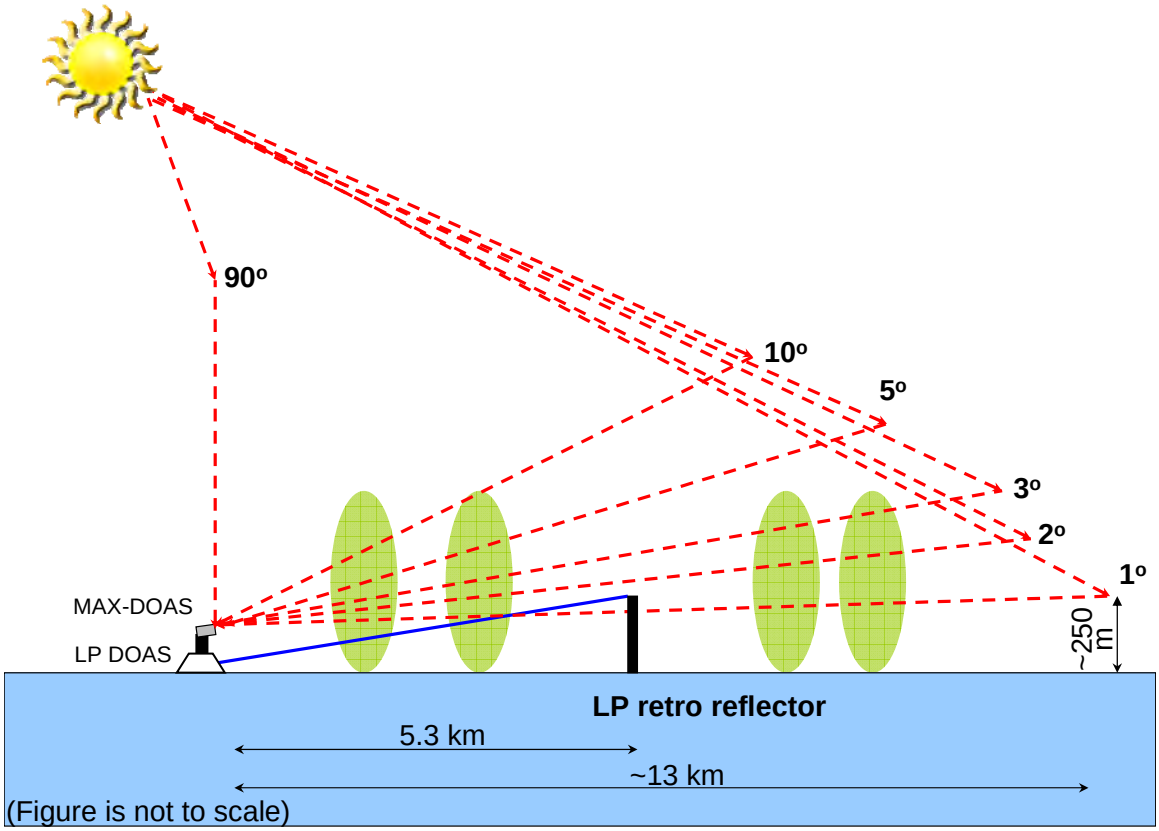

Figure 4.5.11. Schematics of the OIO spatial distribution model. Blue line represents LP DOAS light path between the Zuma and El Matador Beach, red dashed lines represent MAX-DOAS lines of sight at different elevation viewing angles. Green ovals represent inhomogeneous IO plumes.

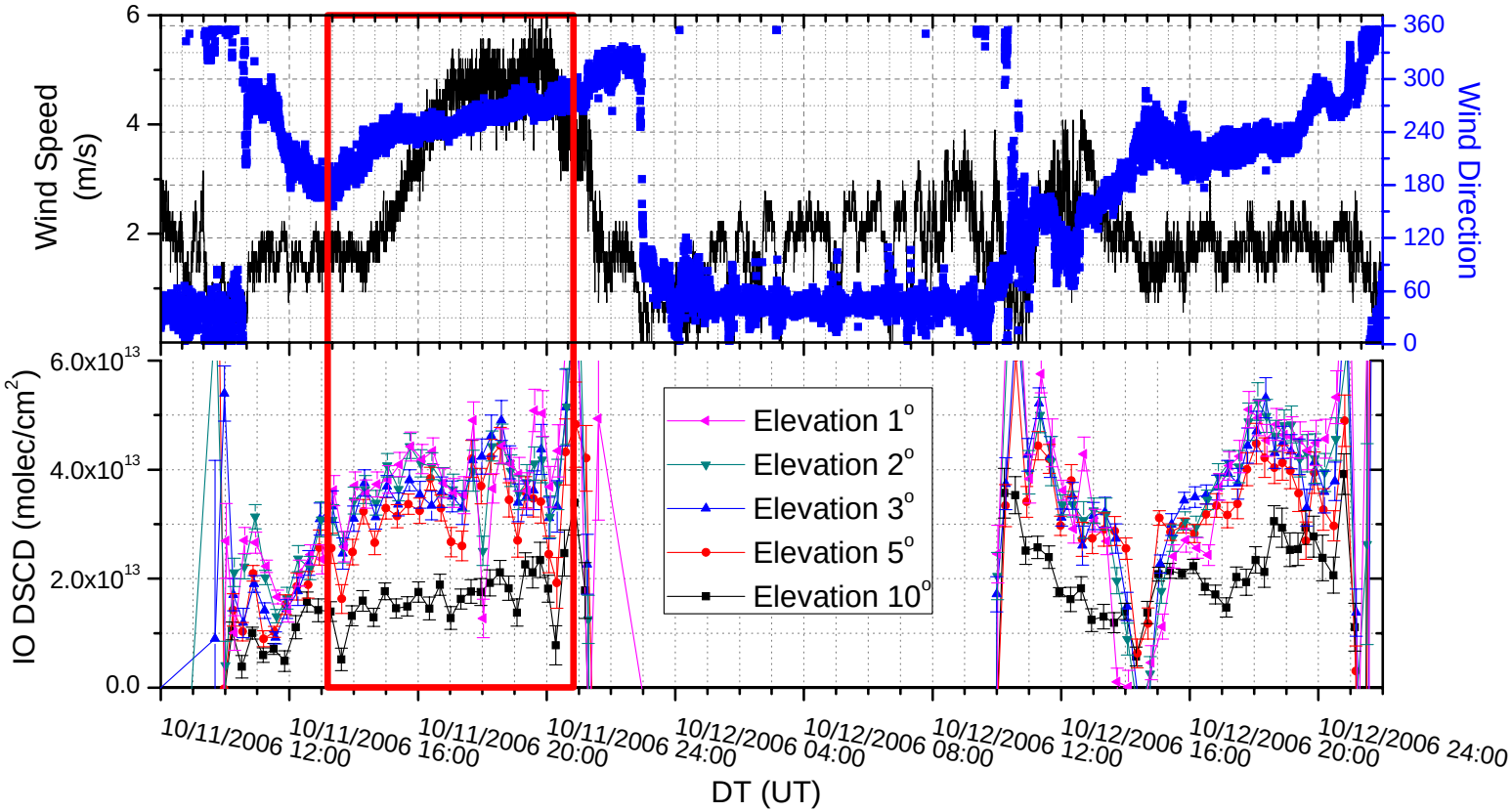

Figure 4.5.12. MAX-DOAS IO DSCDs and wind speed and direction at Zuma Beach on October 11 and 12, 2006. See text for description of outline box.

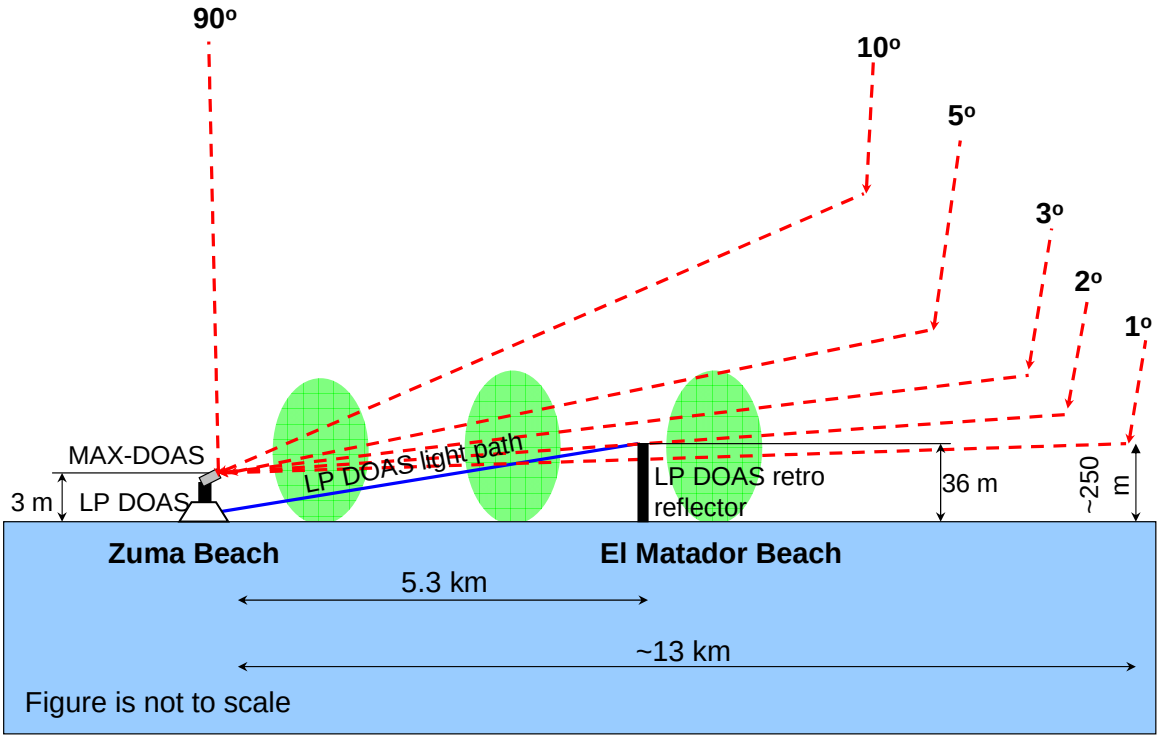

Figure 4.5.13. Schematics of IO spatial distribution at Zuma Beach. Blue line represents LP DOAS light path between the Zuma and El Matador Beach, red dashed lines represent MAX-DOAS lines of sight at different elevation viewing angles. Green ovals represent inhomogeneous IO plumes.

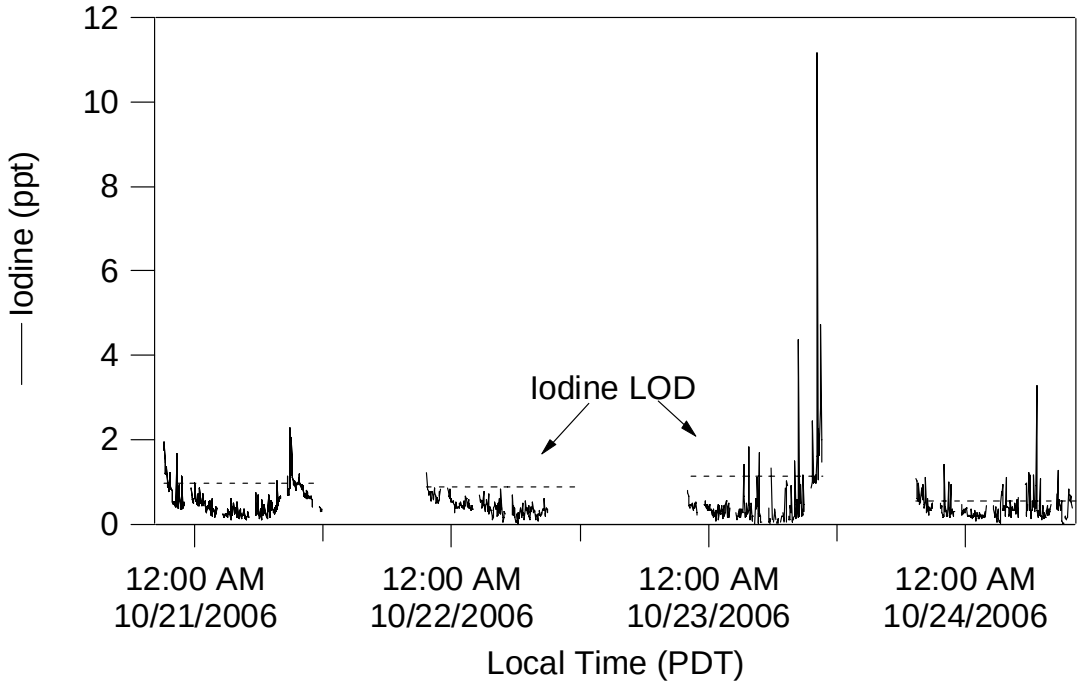

Figure 4.6.1. Battelle ambient I_2 dataset. The solid trace shows the I_2 measurements and the dashed line shows the LOD for each day

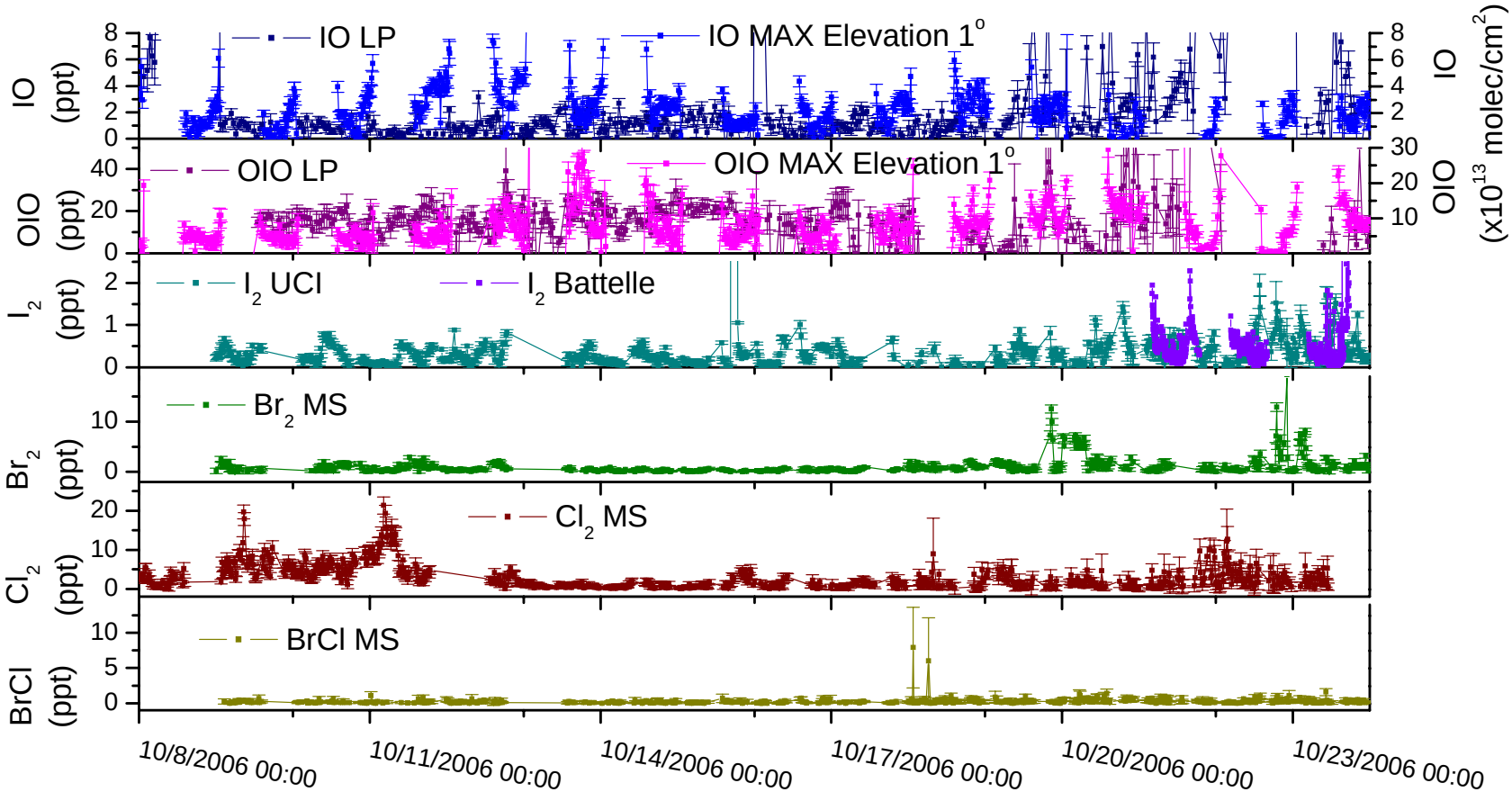

Figure 4.6.2 Overview over all halogen species detected at Zuma Beach. The plot contains the observations from UCLA's DOAS instruments, Battelle's API-MS/MS, and UCI's MS.

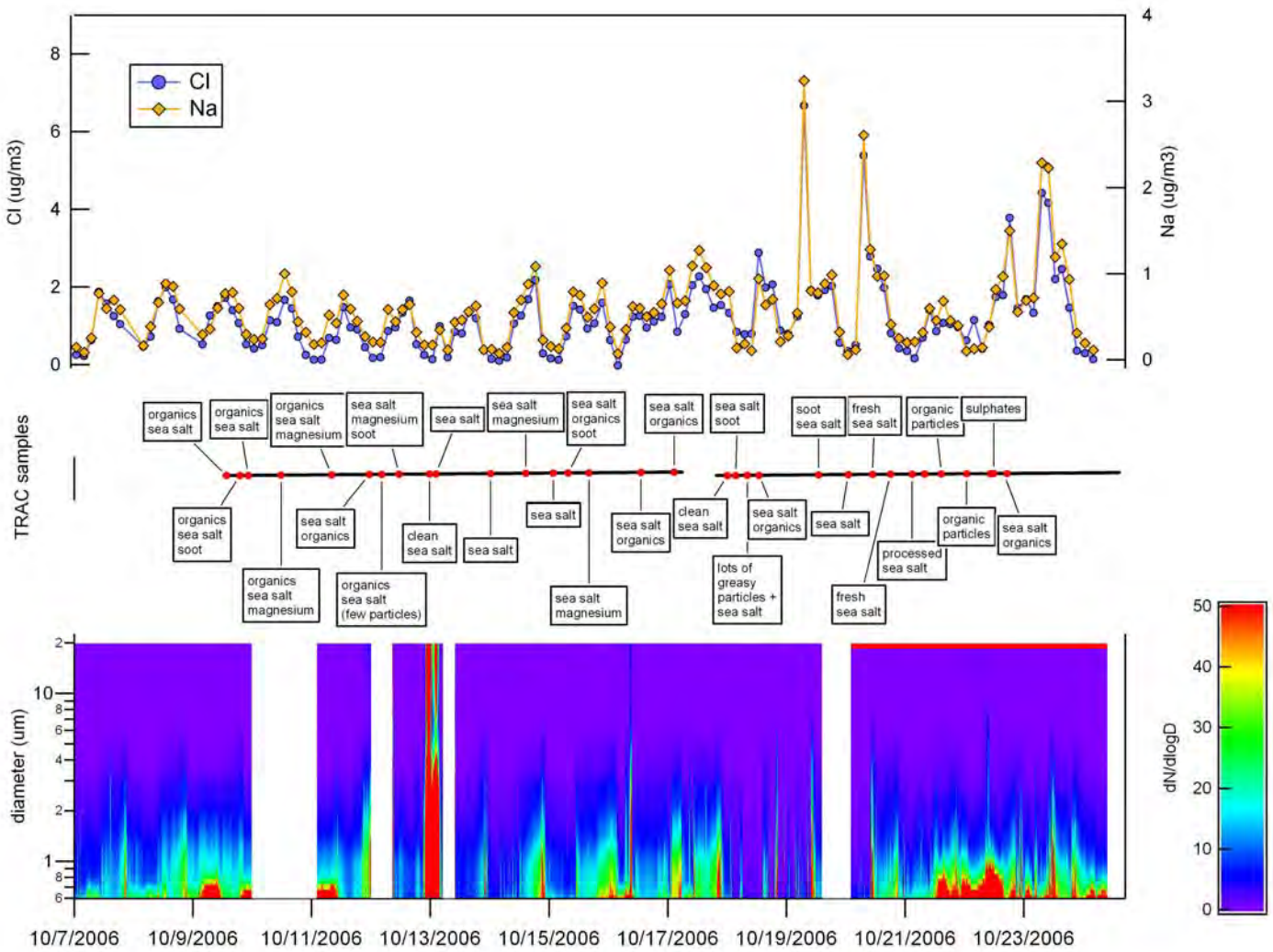

Figure 4.7.1 Aerosol size distribution, TRAC sample particle morphology observations, and Na and Cl aerosol concentrations.

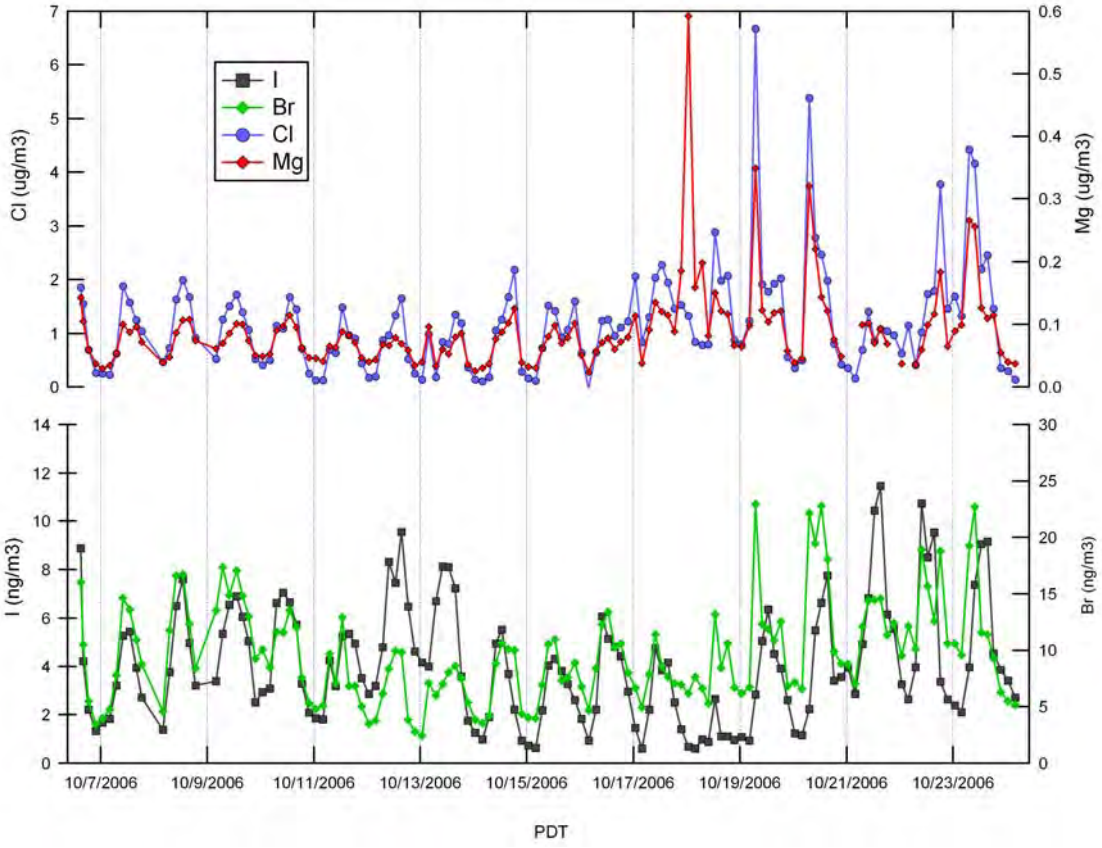

Figure 4.7.2 Particulate composition of major and minor elements associated with sea-salt particles (A. Pszenny, UNH)

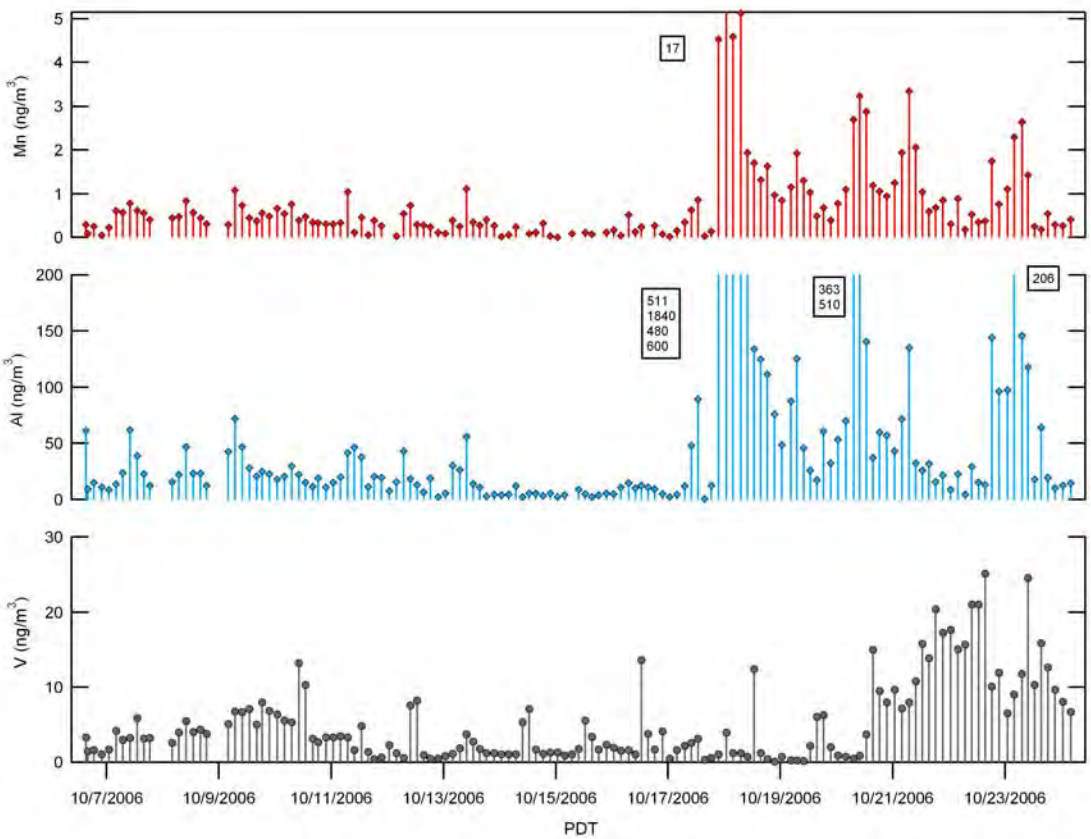

Figure 4.7.3 Particulate trace metal concentrations. Values of offscale data are listed as boxed values (A. Pszenny, UNH)

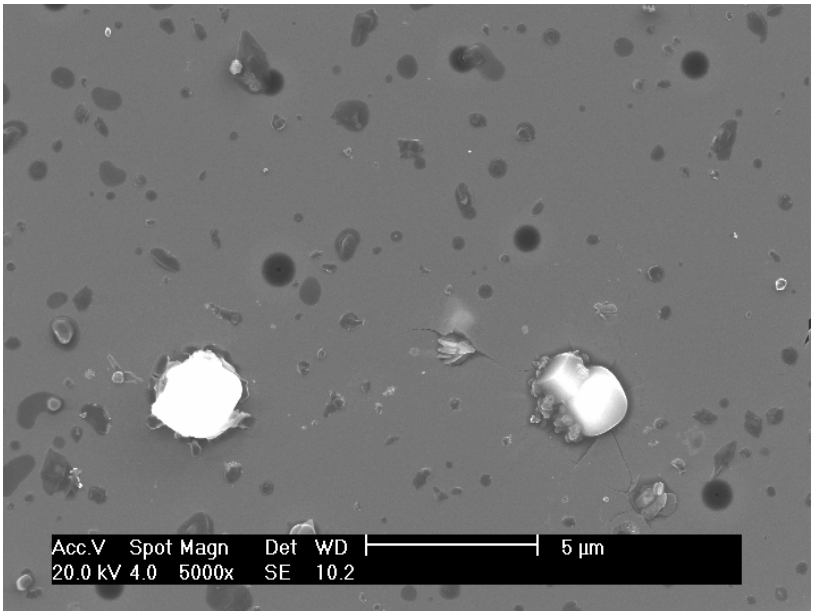

Figure 4.7.4 SEM image of particles collected by TRAC from October 9 22:21 (Disk 1, hole 33) showing fresh sea-salt particles (large white objects) and organic particles (darker objects).

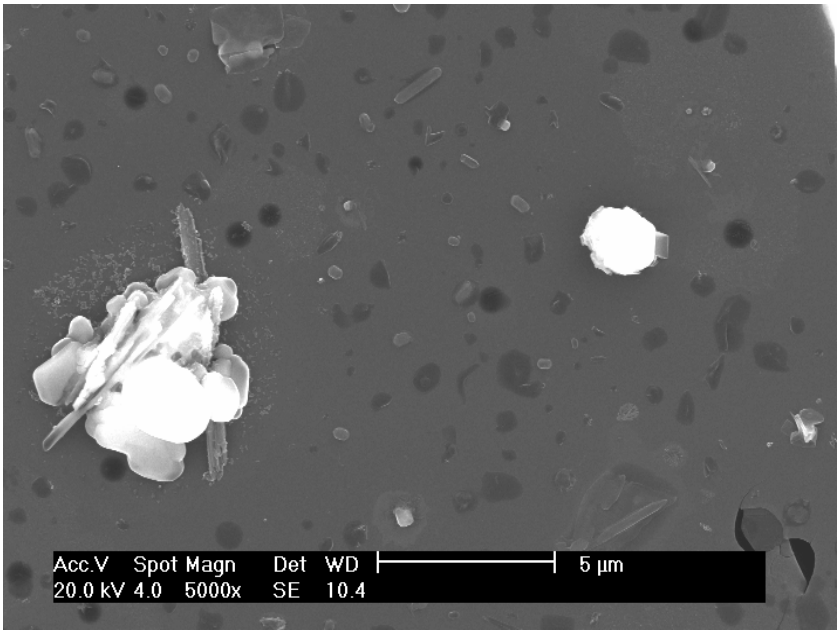

Figure 4.7.5 SEM image of particles collected by TRAC from October 10 11:42 (Disk 1, hole 72) showing chemically processed sea-salt particles (sodium sulfate).

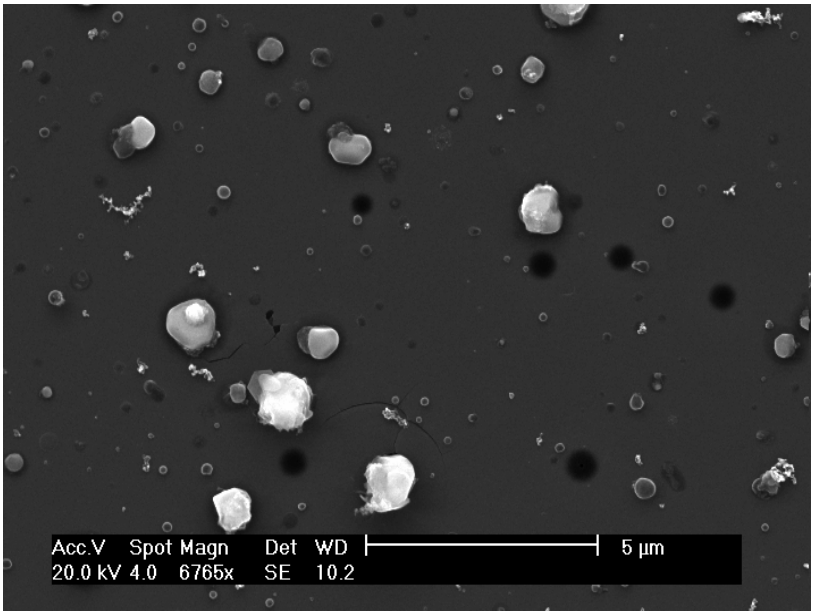

Figure 4.7.6 SEM image of particles collected by TRAC from October 19 13:03 (Disk 2, hole 131) showing fresh and chemically processed sea-salt particles and soot particles.

Chapter 5

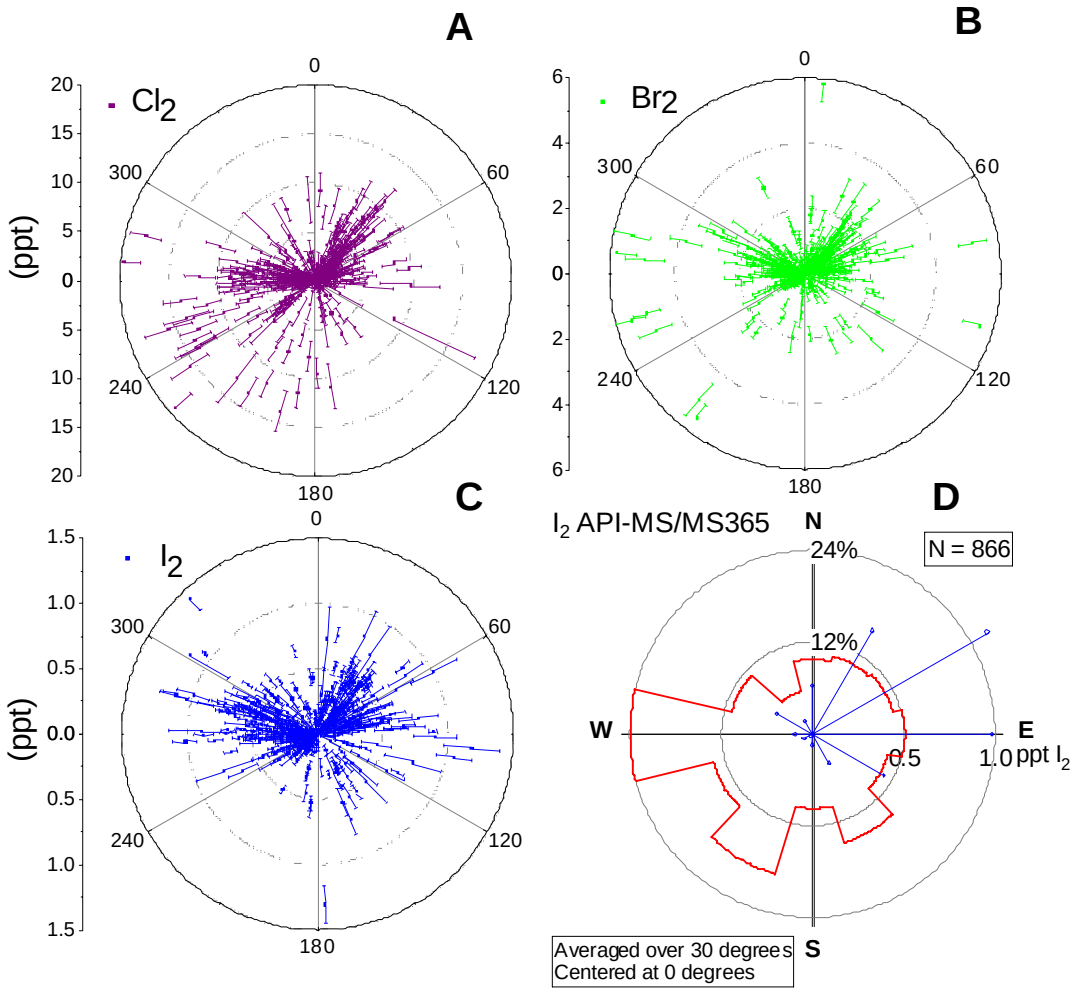

Figure 5.1.1 Dependence of molecular halogens (Cl_2, Br_2, and I_2), as measured by the UCI MS instrument, on wind direction (A-C). Panel D shows a wind rose plot of ambient I_2 measured by the API-MS/MS, where the I_2 mixing ratios (red trace) were averaged over 30 degree wind direction bins and plotted as a function of wind direction on a polar axis. The blue lines represent the frequency of observations in each wind direction bin by percent.

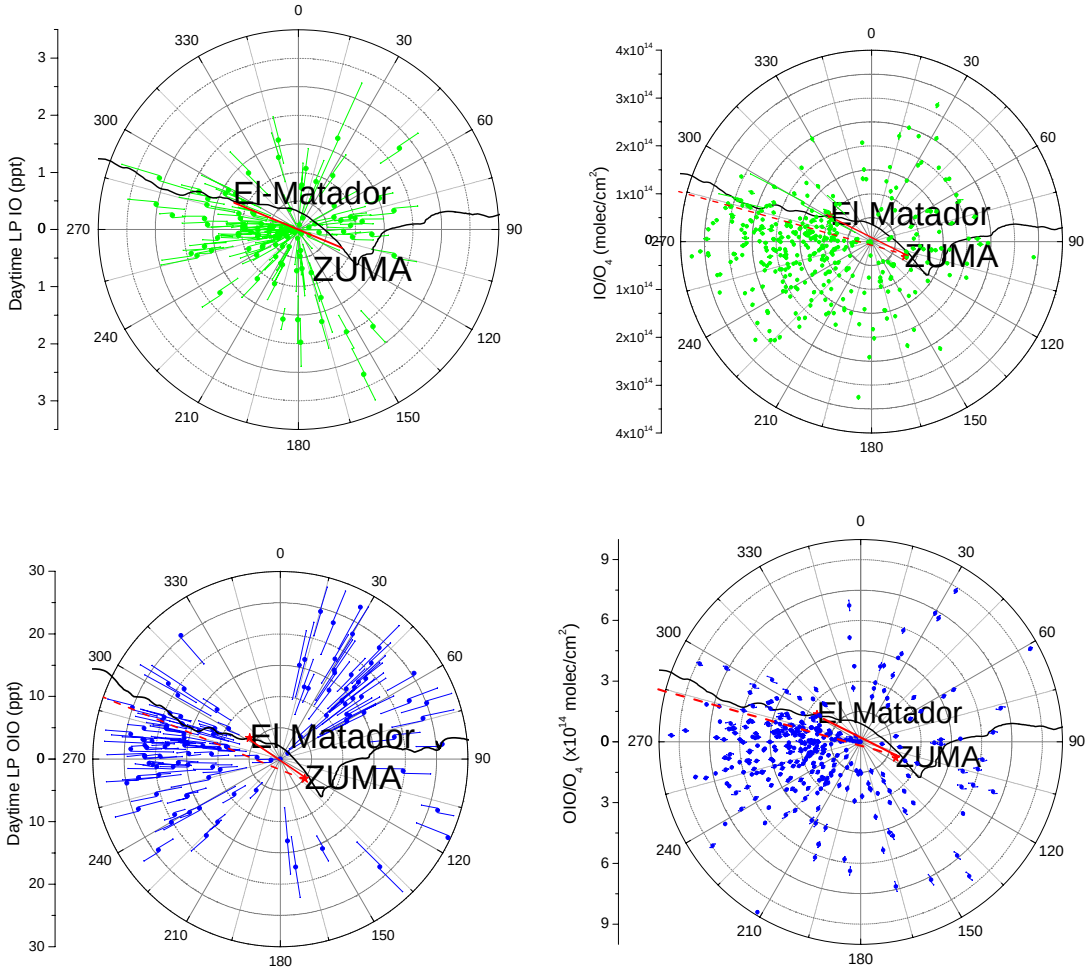

Figure 5.1.2. Daytime IO and OIO mixing ratios (ppt) (left panels) and IO/O_4 and OIO/O_4 ratios (right panels) as a function of wind direction in Malibu.

Figure 5.1.3. Map of the Southern California coastline and neighboring islands. Zuma Beach measurements location is marked by the yellow star. Directly west of Zuma Beach are Channel Islands, and Santa Catalina Island is to the south-east. Distance to both islands from Zuma Beach is approximately 65 kilometers (40 miles).

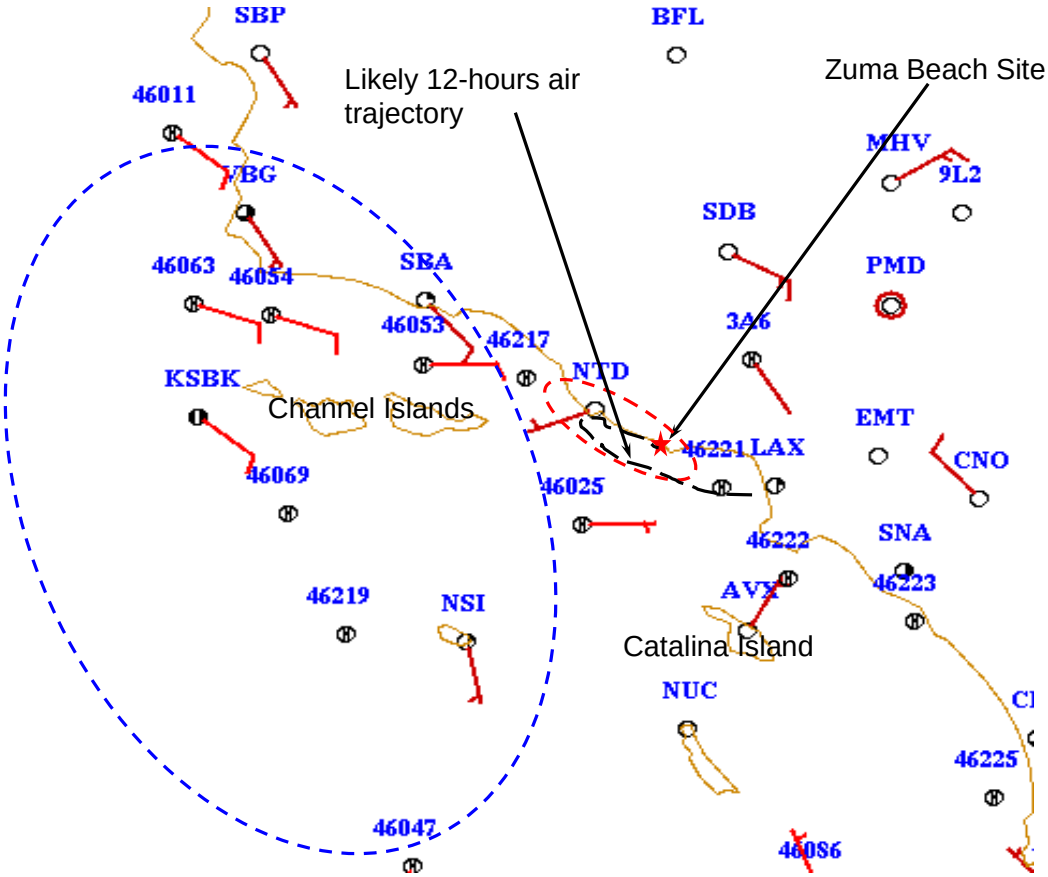

Figure 5.1.4. Wind data reported by weather stations around Southern California coast at 18:00 UT on October 11, 2006. Zuma Beach measurement site is marked by the red star. Blue dashed line represents off-coast cyclonic system that led to the easterly winds observed for the south-east part of LA Basin, off-shore islands and Santa Barbara County. Red dashed line represents areas unaffected by the off-shore cyclone.

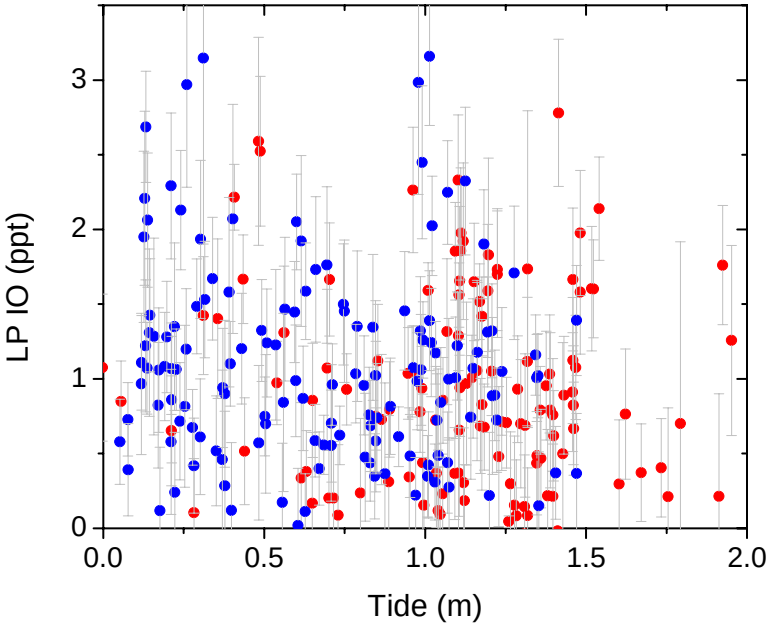

Figure 5.1.5. Observed relationship between the IO measured by the LP DOAS and tidal height in Malibu. Red points represent daytime and blue points nighttime IO measurements.

Figure 5.2.1. Photograph of macroalgae *Macrocystis pyrifera*, Coralline, and Surf grass found on the Zuma Beach in October of 2006.

Figure 5.2.2. Photograph of the kelp emission experiment. As shown, the Teflon bag was being inflated with zero air (*i.e.*, the vent tube was capped).

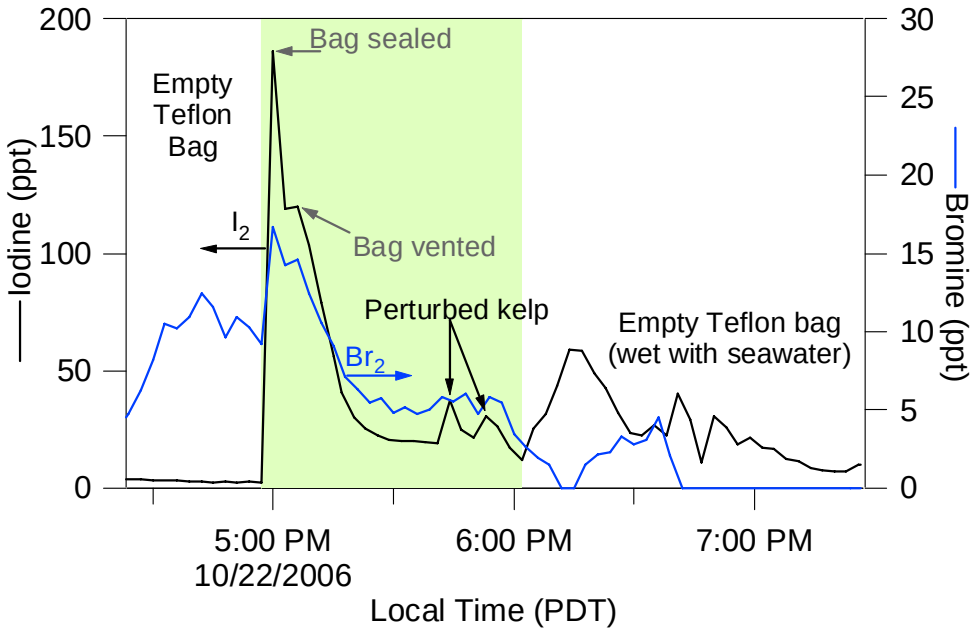

Figure 5.2.3. I_2 emission from kelp while enclosed in a Teflon bag. Also shown are Br_2 measurements during the experiment.

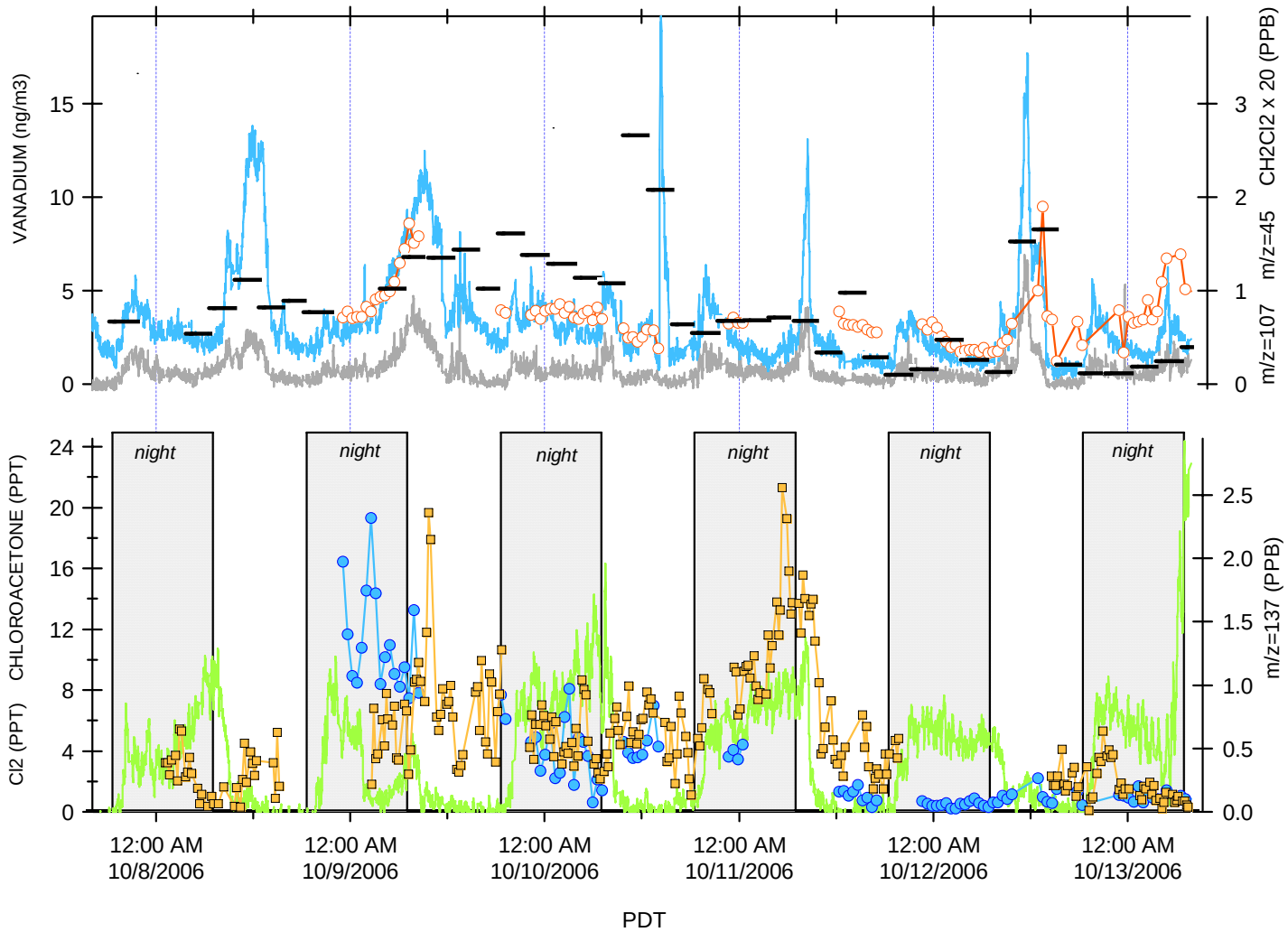

Figure 5.3.1 Time series of selected tracers during a period of elevated Cl_2. Upper panel: particulate vanadium levels are given by horizontal bars, bar length shows sampling duration; CH_2Cl_2 mixing ratios (open circles) are multiplied by 20 to better display data; grey and blue traces are PTR-MS measurements of C_2-alkylbenzene isomers (m/z = 107) and acetaldehyde (m/z = 45) respectively. Lower panel: Cl_2 (orange squares); chloroacetone (blue circles); and total monoterpenes (m/z = 137, green trace). Bottom panel shows nighttime periods defined by sunrise and sunset times.

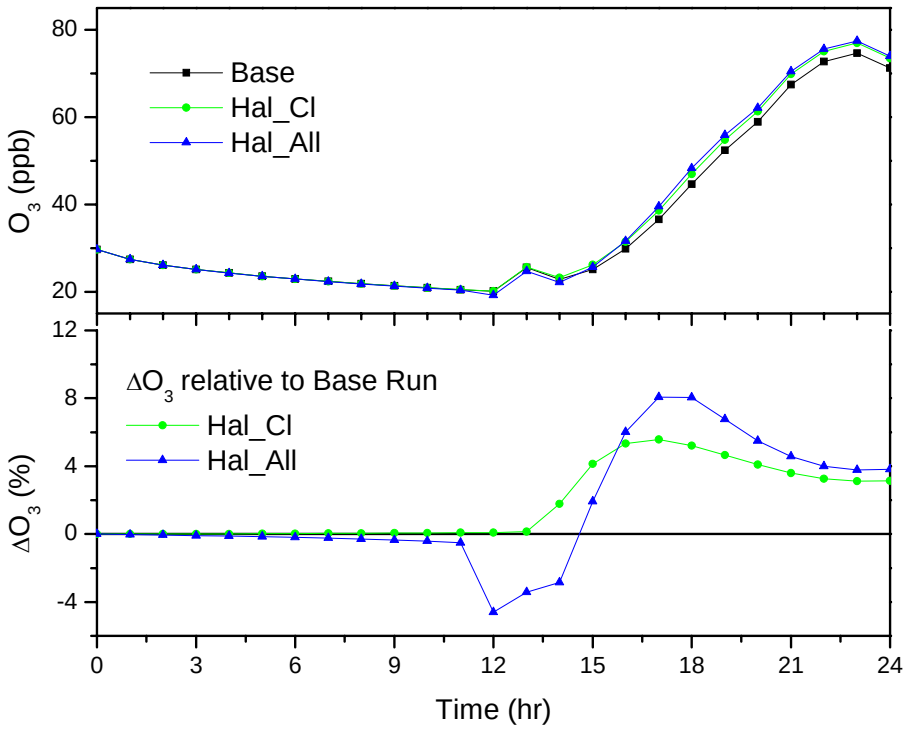

Figure 5.4.1 Modeled ozone mixing ratios for the three scenarios described in Table 5.2. The bottom panel shows the change in ozone in the presence of active halogen chemistry compared to the base run without halogens.

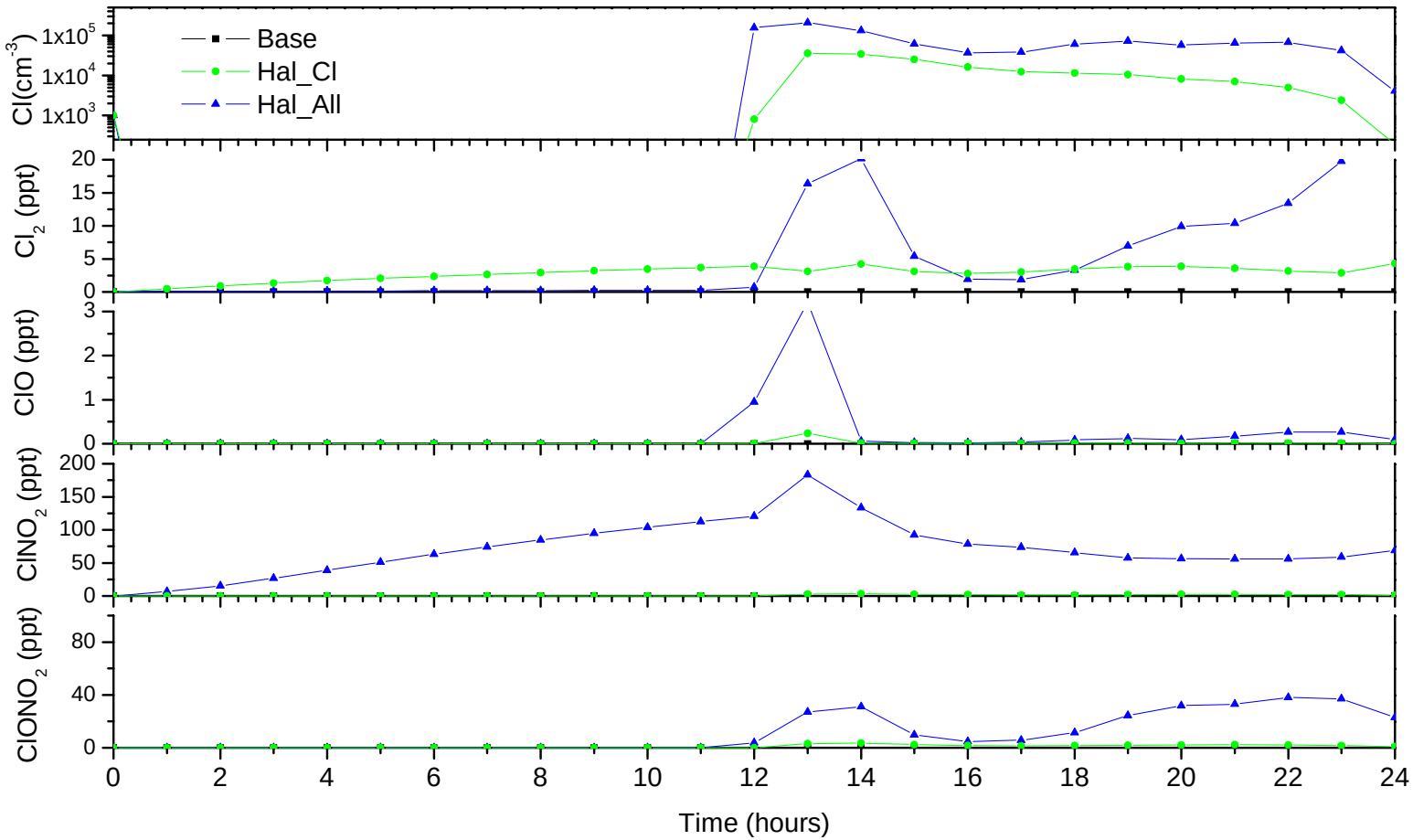

Figure 5.4.2 Modeled concentrations of the most important chlorine species for the scenarios described in Table 5.2.

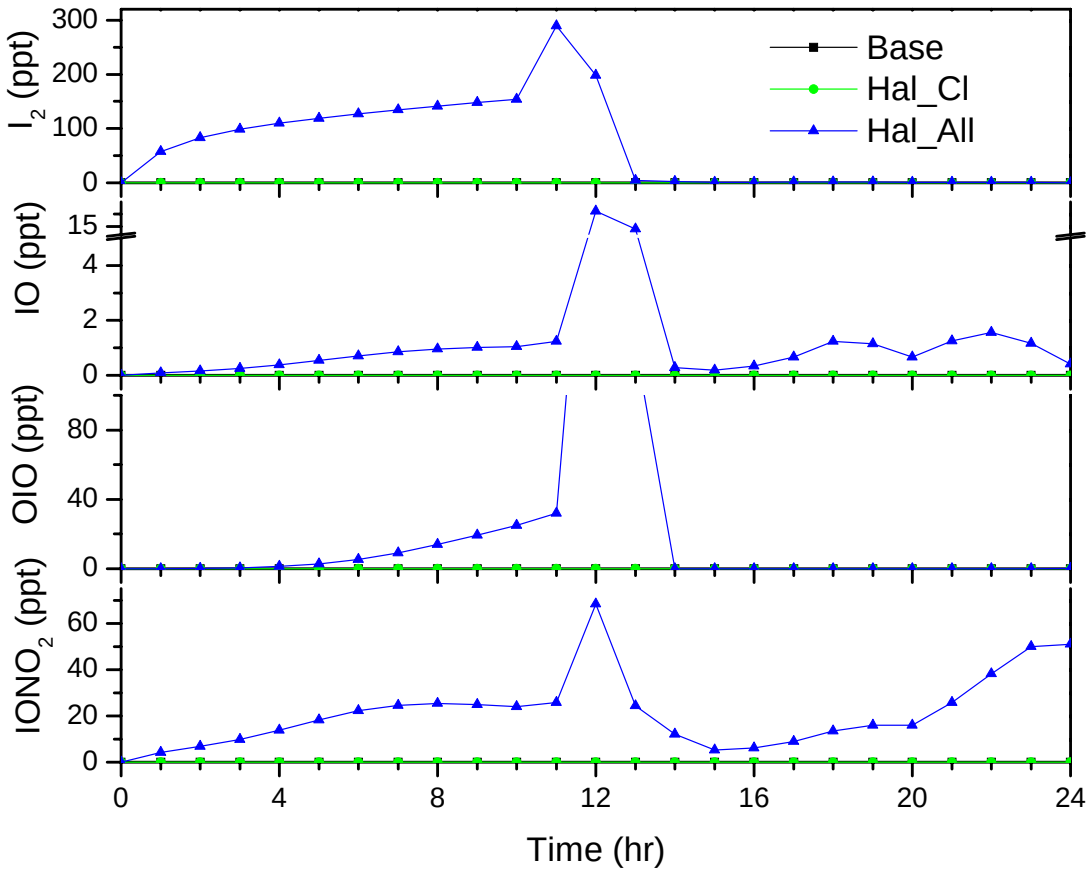

Figure 5.4.3 Modeled concentrations of the most important iodine species for the scenarios described in Table 5.2.

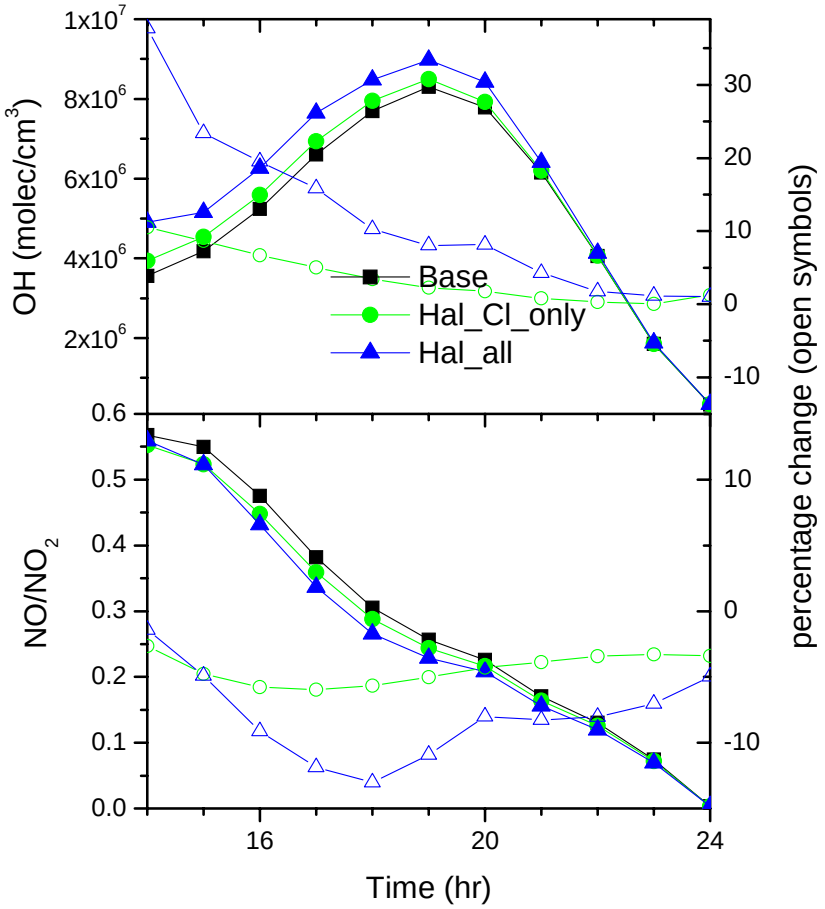

Figure 5.4.4 Modeled OH concentration and NO/NO_2 ratios for the modeled cases (closed symbols) and the percentage change for the two halogen cases compared to the base case without halogens (open symbols).